

NASA Contractor Report 178185

AN EXPERIMENTAL INVESTIGATION OF THE
INTERIOR NOISE CONTROL EFFECTS OF
PROPELLER SYNCHROPHASING

(NASA-CR-178185) AN EXPERIMENTAL
INVESTIGATION OF THE INTERIOR NOISE CONTROL
EFFECTS OF PROPELLER SYNCHROPHASING
(Virginia Polytechnic Inst. and State Univ.)
103 p

N87-11577

Unclas
43864

CSCL 20A G3/71

J. D. Jones and C. R. Fuller

VIRGINIA POLYTECHNIC INSTITUTE
AND STATE UNIVERSITY
Blacksburg, Virginia

Grant NAG1-390
October 1986



National Aeronautics and
Space Administration

Langley Research Center
Hampton, Virginia 23665

TABLE OF CONTENTS

	<u>Page</u>
1. INTRODUCTION.....	1
2. EXERIMENTAL SETUP AND PROCEDURE.....	3
3. MODAL DECOMPOSITION OF SHELL VIBRATION.....	7
4. RESULTS AND DISCUSSIONS.....	10
4.1 Driving Frequency of 680Hz.....	10
4.2 Driving Frequency of 708Hz.....	21
4.3 Effect of Interior Acoustic Damping Material.....	24
5. CONCLUDING REMARKS.....	32
6. REFERENCES.....	35
NOMENCLATURE.....	36
APPENDIX - Modal Decomposition Algorithm.....	37
FIGURES.....	45

1. INTRODUCTION

Due to the potential of significant fuel savings, recent interest has arisen over the use of advanced turboprop (ATP) engines in commercial aircraft. However, preliminary investigations have shown that the interior levels of these aircraft's cabin exceed acceptable levels.

Several transmission paths for propeller noise [1] have been identified. The dominant path for propeller noise is the direct airborne path from the propeller blades through the cabin wall. Traditional passive techniques for noise control would require heavy damping material (or additional mass) around the propeller plane for the necessary noise reduction. This additional weight for noise reduction would offset the potential fuel savings of ATP engines, therefore, it is beneficial to investigate alternative methods for interior noise reduction. As discussed by Metzger [1], one of the most promising alternatives to passive techniques is synchrophasing. This technique involves synchronizing the relative rotational phase of the turboprop engines to achieve maximum interior noise reduction.

Promising results from previous experimental investigations [2,3] have been acquired during inflight testing in an actual aircraft fuselage. However, this procedure will not allow the investigator to isolate individual parameters and correspondingly study their effect on synchrophasing. Although some progress has been made, the physical mechanisms behind the synchrophasing concept are not fully understood. In addition, the in-flight testing can be expensive and time consum-

2. EXPERIMENTAL SETUP AND PROCEDURE

A photograph of the experimental setup is presented in Fig. 1. The aircraft fuselage is modeled as a finite unstiffened aluminum cylinder 0.508 m in diameter by 1.245 m long. The cylinder was formed from a 1.63 mm thick aluminum sheet and has an epoxy-bonded butt-joint seam with a 5 mm wide exterior strap. Future investigations will involve studying the effects of more complex cylinder geometries, however, the purpose of this paper is to present preliminary results. The cylinder is sealed at both ends with 1.9 cm thick wooden end caps and is freely supported at the ends. The noise disturbances due to the propellers are modeled initially as monopole sources. Each monopole source is composed of a pair of 60-watt University Sound driver units. Extension tubes are attached to the driver units enabling the pair of drivers to more closely approximate a single point source. By using two driver units instead of one, source levels can be increased enough to eliminate most signal-to-noise ratio problems. In addition, this will enable the pair of drivers to be used as a dipole source for future investigations. A monopole source is mounted on each side of the cylinder at the axial centerline to simulate the noise disturbances due to the propellers. The source height can be varied to study the effect of asymmetric loading on synchrophasing, however, for this investigation both source heights are fixed at the vertical centerline of the cylinder. The sources are rigidly mounted to the grated floor of the anechoic chamber such that the end of the extension tubes are 10.8 cm from the cylinder. To simulate free-field conditions, the experiments are performed in a 2.3 x 2.6 x 4 m anechoic chamber which has a low frequency cutoff of 250 Hz.

A schematic diagram of the experimental setup showing model details and microphone locations is presented in Fig. 2. Three 6-mm-diameter condenser microphones are mounted on an interior traversing mechanism at radial positions $r/a = 0.150$, 0.513 , and 0.925 . The microphone cables are passed through a hole in one of the wooden end plates which is subsequently sealed with modeling clay. These three microphones are used to evaluate the axial, radial, and circumferential pressure distributions inside the cylinder. Another 6-mm-diameter condenser microphone is used to measure the axial and circumferential pressure distribution on the exterior of the cylinder. In addition, two 6-mm-diameter condenser microphones are positioned 5.4 cm directly in front of the two monopole sources and are used to set the amplitude and relative phase (i.e., synchrophase angle) of each source.

A schematic diagram of the data acquisition system is presented in Fig. 3(a). All microphone signals are conditioned with signal conditioners and amplified and filtered of low frequency noise before being fed into a switching box. Nine small accelerometers are mounted equally spaced around the circumference of the cylinder in the source plane ($x/a = 0.0$) to measure the modal response of the shell due to source excitation. The accelerometer signals are conditioned and are fed into the switching box. All of the microphone and accelerometer signals are in turn processed with a two channel Fast Fourier Transform Analyzer. The cutoff frequency was set to 1500 Hz giving a frequency bandwidth of 7.3 Hz. A phase meter and oscilloscope are used to monitor the amplitudes, relative phase, and waveforms of all the transducer signals.

A schematic diagram of the source generation system is presented in Fig. 3(b). The reference pure tone signal for the noise source is generated by a function generator and is monitored by a frequency counter. The reference signal is fed into a gain-phase board where the gain and phase of two channels are set independently based upon the signals from the source microphones. The signals from the gain-phase board are then amplified and sent to the monopole sources. A digital voltmeter is used to monitor the output voltages of the amplifiers to ensure that the sources are not being overloaded.

Figure 4 shows the coordinate system used in this investigation. The interior microphones were initially positioned horizontally in the source plane towards source I (i.e., $x/a = 0.0$, $\theta = 0^\circ$). Pressure measurements were recorded for the three radial microphone stations over the range of synchrophase angles of $\phi = 0$ to 360 using 45 degree phase increments. Additional pressure measurements were recorded at five degree phase increments around the optimum synchrophase angle of each interior microphone. While in the source plane ($x/a = 0.0$), this procedure is repeated in the upper half of the cylinder at four additional circumferential positions, $\theta = 45, 90, 135$, and 180 degrees. This procedure is also repeated in the horizontal source plane (at $\theta = 0^\circ$) for axial positions $x/a = 0.4, 0.8$ and 1.6 . Exterior microphone measurements were recorded at fifteen axial positions in the horizontal source plane (at $\theta = 0^\circ$) for synchrophase angles of $\phi = 0$ and 180 degrees. Finally, exterior microphone measurements were recorded in the propeller plane at seven circumferential positions for synchrophase angles of $\phi = 0$ and 180 degrees. All measurements were completed for

pure tone source conditions of 680 and 708 Hz. These frequencies were chosen because they are within a range of typical scaled fundamentals of the propeller noise. The fundamental frequency of the propeller noise is scaled based upon the diameters of business and small body aircraft to that of the fuselage model. A third case was run with the source conditions again set to 708 Hz. However, for this case a layer of 12.7-mm-thick flexible polyurethane polyester foam was placed on the interior of the cylinder covering 145 degrees of the bottom of the cylinder, in order to investigate the influence of cavity acoustic input impedance on the system response.

3. MODAL DECOMPOSITION OF SHELL VIBRATION

The radial vibration response of the cylinder was measured for the modal decomposition algorithm presented in the appendix. The relative amplitudes and phases of the nine equally spaced accelerometers were measured over a range of synchrophase angles from $\phi = 0$ to 360 degrees using 45 degree phase increments. Results from the decomposition algorithm defined the relative modal composition of the cylinder within the sampling restrictions of the transducers thereby enabling the dominant mode of the cylinder to be determined for various synchrophase angles. The modal composition of the cylinder provides physical insight in understanding how sound is transmitted into the model.

The decomposition technique used in this investigation is similar to methods proposed by Moore [5] and Silcox and Lester [6]. The radial displacement of a cylinder at any given time can be represented by a Fourier series of sines and cosines as follows.

$$\tilde{w}(\theta, t) = \sum_{n=0}^{\infty} [A_n \cos(n\theta) + B_n \sin(n\theta)] e^{j\omega t} \quad (1)$$

When a cylinder is excited, circumferential waves propagate in both directions around the cylinder combining to create an interference pattern or standing wave. To solve for the complex modal amplitudes A_n and B_n , equation (1) is multiplied by $\cos(m\theta)$ and $\sin(m\theta)$, respectively, and integrated from 0 to 2π . Thus,

$$\int_0^{2\pi} \tilde{w}(\theta) \cos(m\theta) d\theta = \sum_{n=0}^{\infty} \left[\int_0^{2\pi} A_n \cos(n\theta) \cos(m\theta) d\theta + \int_0^{2\pi} B_n \sin(n\theta) \cos(m\theta) d\theta \right] \quad (2)$$

$$\int_0^{2\pi} \underline{w}(\theta) \sin(m\theta) d\theta = \sum_{n=0}^{\infty} \left[\int_0^{2\pi} A_n \cos(n\theta) \sin(m\theta) d\theta + \int_0^{2\pi} B_n \sin(n\theta) \sin(m\theta) d\theta \right] \quad (3)$$

where $m = 0, 1, 2, 3, \dots, \infty$ and the time dependence $e^{j\omega t}$ has been omitted. By utilizing the orthogonality characteristics of the sine and cosine functions, equations (2) and (3) can be reduced and rearranged to solve explicitly for the modal amplitudes. The resulting equations are

$$A_n = \frac{1}{\epsilon\pi} \int_0^{2\pi} \underline{w}(\theta) \cos(n\theta) d\theta \quad (4)$$

$$B_n = \frac{1}{\epsilon\pi} \int_0^{2\pi} \underline{w}(\theta) \sin(n\theta) d\theta \quad (5)$$

where $\epsilon = 2$ for $n = 0$

$\epsilon = 1$ for $n > 0$

$n = 0, 1, 2, 3, \dots, \infty$.

If $\underline{w}(\theta)$ is known completely as a function of θ , all of the modal amplitudes can be determined. In practice, however, $\underline{w}(\theta)$ is known only at discrete points around the cylinder. Therefore, the integrals of equations (4) and (5) must be represented as summations of the form

$$A_n = \frac{1}{\epsilon\pi} \sum_{p=1}^N \underline{w}(\theta_p) \cos(n\theta_p) \Delta\theta_p \quad (6)$$

$$B_n = \frac{1}{\epsilon\pi} \sum_{p=1}^N \underline{w}(\theta_p) \sin(n\theta_p) \Delta\theta_p \quad (7)$$

where N_p is the number of circumferential base positions and $\Delta\theta_p = 2\pi/N_p$ for equally spaced base positions.

In practice, the assumed mode shapes are fitted to the measured data, thus, any measurement errors or contributions from modes excluded from the decomposition model could cause serious errors in the results of the decomposition. The decomposition will always reproduce the measured data within the constraints of the system, however, exclusion of significant higher order modes results in a folding back of these modes known as aliasing. How the aliasing occurs (i.e., which higher order fold back into which lower order modes) is dictated by the number of base points.

In this investigation, the highest order mode obtained from the decomposition model was the $n = 4$ mode. In practice, the most effectively excited modes are the $n = 0, 1$, and 2 modes. The decrease in the $n = 3$ and $n = 4$ modes indicates a general reduction in the levels of the higher order modes, thus, the decomposition was not expanded further.

4. RESULTS AND DISCUSSIONS

4.1 Driving Frequency of 680 Hz

The results presented below are from the case with pure tone source conditions of 680 Hz. Figures 5(a) and 5(b) show a comparison of the axial and circumferential pressure distributions on the exterior of the cylinder for synchrophasing angles of $\phi = 0$ and 180 degrees. Although propeller sources are better modeled as dipoles, the axial and circumferential pressure distributions on the exterior of the cylinder due to the monopole sources used in this investigation are surprisingly similar to those measured on the exterior of an actual twin-engine turboprop aircraft fuselage [7]. This result justifies the sources used in this investigation and eliminates the safety problems associated with using actual propeller sources. The axial pressure distribution on the exterior of the cylinder is symmetric about the propeller plane and decays about 13 dB by two cylinder radii. The similarity between this result and those from reference 7 implies that the pressure forcing function at the fuselage surface is due to the near field of each source or a very directional source. The synchrophase angle appears to have negligible effect on the axial pressure distribution at $\theta = 0$ degrees. However, the synchrophase angle has a significant effect on the circumferential pressure distribution for $\theta > 45$ degrees. This indicates that the near field of the source has substantially decayed in this region thereby allowing diffraction effects around the cylinder to become important. The circumferential pressure distribution is symmetric about the horizontal source plane and decays 13-16 dB for a synchrophase angle of $\phi = 0$ degrees and 40-42 dB for a synchrophase angle of $\phi = 180$

degrees. The more rapid decay in the circumferential pressure distribution for a synchrophase angle of $\phi = 180$ degrees can be explained using an interference interpretation. Near a point of symmetry between the sources (i.e., $\theta = 90^\circ$), cancellation occurs as the contribution from each source is relatively equal. However, in a region near $\theta = 0$ or 180 degrees the contribution from each individual source dominates the exterior pressure field and the synchrophase angle has little effect.

Figure 6 shows the relative circumferential modal amplitudes of the cylinder versus synchrophase angle in the source plane for modes $n = 0$ to 4. The modal response of the cylinder is dominated by the A_2 circumferential mode. For an ideal cylinder with the sources symmetrically positioned as shown in Fig. 2, the B_n modes should theoretically be zero. However, the decomposition results show significant B_n modes with the $n = 2$ mode dominating. The decomposition results indicate basically three levels of modal excitation. First, A_n modes are generated in the cylinder from direct source excitation. Second, the B_n modes are predominantly generated by a coupling effect with the A_n modes due to cylinder asymmetry and the presence of the butt-joint seam along the cylinder. The fact that the B_n modal amplitudes are generally very similar to the A_n modal amplitudes over the range of synchrophase angles supports this theory. Similar coupling behavior in asymmetric cylinders excited by an internal acoustic plane wave has been observed by Youri and Fahy [8]. Third, a fraction of the B_n modal amplitudes are generated due to slight source asymmetry. This fraction of B_n modal amplitudes are uncoupled to the A_n modes.

As discussed in reference 4, theoretically the optimum synchrophase angle for even A_n modes and odd B_n modes is $\phi = 180$ degrees. In contrast, the optimum theoretical synchrophase angle for odd A_n modes and even B_n modes is $\phi = 0$ degrees. The results of the decomposition are generally similar to the analytical results, however, increased modal response near $\phi = 45$ degrees tends to mask this effect somewhat. Discrepancies from the expected theoretical results are partly due to cylinder imperfections and associated mode coupling as discussed previously. The cylinder imperfections significantly alter the modal composition of the cylinder and the contained acoustic field, and thus will affect the results of this experimental investigation. These results illustrate the need for monitoring the vibration response of the cylinder in conjunction with the interior acoustic field in order to successfully explain the resultant effects.

Figure 7 shows the relative radial displacement and phase of the cylinder in the source plane ($x/a = 0.0$) for two contrasting synchrophase angles of 45 and 180 degrees. In practice, the radial response of the cylinder was measured only at the nine base points, however, the radial response at other circumferential positions can be interpolated for based upon the results from the decomposition model. This figure assumes that the decomposition model includes all contributing modes, thus, any measurement errors or aliasing effects could significantly alter the results of this figure. Based upon the decomposition results, the radial displacement of the cylinder is distorted somewhat indicating the complex vibration response of the cylinder. The relatively small radial displacements calculated near circumferential position $\theta = 90$

degrees are most likely due to the exterior seam which runs along the top of the cylinder at this position. The relative radial displacement decreases significantly when the synchrophase angle is changed from $\phi = 45$ degrees to $\phi = 180$ degrees. This result indicates that synchrophasing has potential uses in vibration control as well as interior noise control. Although all four lobes are not distinct, Figure 7 shows a mode shape somewhat similar to the A_2 mode with the phase changes of 180 degrees through nodal points being apparent. However, the mode shape is somewhat distorted due to significant contributions from the A_0 , B_1 , and B_2 modes.

Figure 8 shows the interior pressure measurements versus synchrophase angle in the source plane at the three radial microphone stations for circumferential position $\theta = 0$ degrees. The peak sound pressure level at this circumferential position is 116 dB. This figure shows that the potential noise reduction is a wide band phenomena with respect to the synchrophase angle. The results indicate that noise control by synchrophasing is not limited to just two and four bladed turboprops but can be used in multibladed turboprops. For example, if a synchrophaser controlling an eight bladed propeller had a shaft stability of $\pm 5^\circ$, this translates to $\pm 40^\circ$ of synchrophase angle stability. The corresponding minimum sound pressure level reduction is approximately 8dB over the synchrophase angle bandwidth. This is of the order of reduction measured in real aircraft using synchrophasing [2].

The potential noise reduction varies from 15-25 dB depending on radial position. The optimum synchrophase angles for the three radial stations range from $\phi = 190$ to $\phi = 225$ degrees. These results can be

explained by considering the radial vibration response of the shell. The monopole sources excite a series of circumferential modes in the shell wall which in turn couples to the contained acoustic field via the momentum boundary condition. Thus the total acoustic pressure at a given interior location consists of a superposition of varying contributions from the circumferential modes. The variations in the contributions depend on interior location and are dictated by the Bessel function coupling behavior of the circumferential modes. The dominant mode generated in the 680 Hz case is the $n = 2$ mode with significant contributions coming from the $n = 0$ and 1 modes. At circumferential position $\theta = 0$ degrees, the contributions to the interior pressure levels from the B_n modes are theoretically zero. With the dominant A_n mode being even (i.e., $n = 2$), this implies that the optimum synchrophase angle should be near $\phi = 180$ degrees as shown in Fig. 8. The small deviations from the expected optimum synchrophase angle of $\phi = 180$ degrees are due to minor contributions from the A_n and B_n modes which have an optimum synchrophase angle near $\phi = 0$ degrees. The minor contributions, from the B_n modes are caused by the coupling effects due to cylinder imperfections as discussed earlier. The variation of the optimum synchrophase angle with radial position is due to differing contributions from the circumferential modes at the different radial positions.

Interior pressure levels at $\theta = 0$ degrees are very sensitive to the synchrophase angle. This is true even near the cylinder wall at $r/a = 0.925$. However, as shown in Fig. 5(a) the exterior pressure distribution at $\theta = 0$ degrees is essentially unaffected by the synchrophase

angle. This result indicates the sound is not being transmitted directly into the cylinder via a localized area of the wall but instead excites a series of circumferential modes which subsequently couple to the interior acoustic field. Thus, the representation of an aircraft fuselage as a finite flat plate or curved panel may be inadequate at low frequencies.

The pressure response at radial position $r/a = 0.925$ indicates the transmission loss through the shell is as low as -3dB. Typical sealed shells normally give a significant transmission loss, however, in this case, the low transmission loss is apparently due to the interaction of the two sources. When a single source was used, a transmission loss of around 30dB was measured.

Figure 9 shows the interior pressure measurements versus synchrophase angle in the source plane at the three radial microphone stations for circumferential position $\theta = 45$ degrees. The peak sound pressure level at this circumferential position is 90 dB. In contrast, the peak sound pressure level at $\theta = 0$ degrees is 116 dB. The deterioration in the interior acoustic field is due to the reduction in contribution of the dominant A_2 mode at $\theta = 45$ degrees. Obviously, the need for noise reduction at this circumferential position is diminished. The potential noise reduction at $\theta = 45$ degrees is about 10 dB for radial stations $r/a = 0.513$ and 0.925 and about 23 dB for $r/a = 0.150$. The optimum synchrophase angle for all three radial stations has increased to near $\phi = 260$ degrees. At $\theta = 45$ degrees, contributions from all of the decomposed A_n and B_n modes will be present except for the A_2 and B_4 modes. This results in approximately equal contributions from modes

with an optimum synchrophase angle of $\phi = 180$ degrees and $\phi = 0$ (or 360) degrees. Thus, an optimum synchrophase angle of 260 degrees is not surprising. Due to a lack of dominance of modes with an optimum synchrophase angle of either $\phi = 0$ or 180 degrees, the potential noise reduction by the synchrophasing technique has decreased significantly for radial station $r/a = 0.513$ and 0.915 . The $n = 0$ mode is the only mode which theoretically contributes to the acoustic pressure at the centerline of the cylinder. Therefore, as the cylinder's centerline is approached, the $n = 0$ mode will begin to dominate and the potential noise reduction is again realized for radial station $r/a = 0.150$. This theory is supported by the fact that the optimum synchrophase angle at $r/a = 0.150$ has shifted back towards $\phi = 180$ degrees somewhat as would be expected for a dominant $n = 0$ mode.

Figure 10 shows the interior pressure measurements versus synchrophase angle in the source plane at the three radial microphone stations for circumferential position $\theta = 90$ degrees. The peak sound pressure level at this position is about 113 dB which is 3 dB below the peak sound pressure level recorded at $\theta = 0$ degrees. The potential noise reduction varies between 12-34 dB depending on radial position. The optimum synchrophase angle is $\phi = 180$ degrees for radial station $r/a = 0.513$ and 0.925 and $\phi = 0$ degrees for $r/a = 0.150$. At $\theta = 90$ degrees, the odd A_n modes and even B_n modes theoretically do not contribute to the interior acoustic field. This leads to a dominant A_2 mode and therefore will give good potential noise reduction and an optimum synchrophase angle near 180 degrees as measured at $r/a = 0.513$ and 0.925 . Hence, the pressure levels at radial position $r/a = 0.150$ are surprising

and difficult to explain. The pressure response at this radial position could be caused by one or a combination of several potentially contributing factors. First, a signal-to-noise ratio problem could cause spurious results near a low interior pressure response region. Second, the results could be partially caused by minor deviations in the circumferential microphone position. As the radial position of the microphone is reduced, any variation in cylindrical coordinate θ for a fixed error in microphone location will increase. Thus, close to the centerline small errors in microphone positioning may lead to larger contributions from other modes than near the shell wall. Third, shell asymmetry coupled with contributions from both A_n and B_n modes could also alter the interior acoustic field at $r/a = 0.150$.

Figure 11 shows the interior pressure measurements versus synchrophase angle in the source plane at the three radial microphone stations for circumferential position $\theta = 135$ degrees. The peak sound pressure level at this circumferential position is 87 dB indicating that the need for noise reduction at this position is comparatively less. The reduction in the interior acoustic field at this position is again due to a smaller contribution from the dominant A_2 mode. The results at circumferential position $\theta = 135$ degrees are generally similar to the results recorded at $\theta = 45$ degrees except that the optimum synchrophase angle at the three radial microphone stations has decreased to near $\phi = 90$ degrees. This result is due to the interior microphone being positioned symmetrically opposite to the $\theta = 45$ degree position. Theoretically, the results at $\theta = 135$ degrees should be a mirror image of those at $\theta = 45$ degrees through the line $\phi = 180$ degrees of the figures. Due

to the similarities of behaviors in both cases, results at $\theta = 135$ degrees can be explained by considering the radial vibration response of the shell as previously discussed for circumferential position $\theta = 45$ degrees.

Figure 12 shows the interior pressure measurements versus synchrophase angle in the source plane at the three radial microphone stations for circumferential position $\theta = 180$ degrees. The peak sound pressure level at this position is about 104 dB indicating that the need for noise reduction at this position is not as critical as at circumferential position $\theta = 0$ degrees. The results at $\theta = 180$ degrees are generally similar to those recorded at $\theta = 0$ degrees except the optimum synchrophase angle for radial position $r/a = 0.150$ has decreased to near $\phi = 90$ degrees. Due to the similarities, the results at $\theta = 180$ degrees can be explained by again considering the radial vibration response of the shell as previously discussed for circumferential position $\theta = 0$ degrees.

As shown in Figs. 8-12 the interior pressure levels in the source plane are generally greatest near the shell wall and decrease rapidly as the centerline of the cylinder is approached. The low pressure levels near the centerline of the cylinder ($r/a = 0.150$) are a result of the fact that the contributions to the interior acoustic field from all the modes except the $n = 0$ mode theoretically go to zero as the centerline of the cylinder is approached. Therefore, the pressure measurements at $r/a = 0.150$ are expected to be significantly lower than the other radial positions. This result gives additional support to the theory that the modal composition of the cylinder governs the interior acoustic field.

Figures 13, 14 and 15 show the interior pressure measurements

versus synchrophase angle in the source plane at the six circumferential microphone positions for radial stations $r/a = 0.150$, 0.513 and 0.925 , respectively. The interior pressure measurements versus synchrophase angle for $\theta > 90$ degrees vary as a mirror image of the results for $\theta < 90$ degrees except that the pressure levels for $\theta > 90$ degrees are generally about 5-20 dB lower than the pressure levels for $\theta < 90$ degrees. The nonsymmetric circumferential pressure distribution is probably caused by the presence of significant B_n modal amplitudes due to the imperfections in the shell.

Figures 8, 16, 17, and 18 show interior pressure measurements versus synchrophase angle at $\theta = 0$ degrees for the three radial microphone stations at axial position $x/a = 0.0$, 0.4 , 0.8 and 1.6 , respectively. At all four axial positions there is a sharp decrease in the radial pressure distribution from the shell wall to the shell centerline. The optimum synchrophase angle for all of these microphone positions is near $\phi = 180$ degrees, except for radial position $r/a = 0.150$ of Fig. 18. This indicates that the vibration response of the cylinder downstream of the source plane is probably still dominated by the A_2 mode. The spurious results of Fig. 18 for radial microphone station $r/a = 0.150$ are probably due to a combination of signal-to-noise ratio problem, microphone positioning errors, and cylinder asymmetry as discussed previously. Also, this result could be partially due to end effects (i.e., interior axial standing waves) which become more important as the interior acoustic field decreases near the centerline of the shell. These potential problems make it difficult to correlate the results with modal behavior.

Figures 19, 20, and 21 show the interior pressure measurements

versus synchrophase angle at $\theta = 0$ degrees for the four axial microphone positions at radial stations $r/a = 0.150, 0.513$ and 0.925 , respectively. The interior pressure levels at all three radial microphone stations are very high in the source plane and decrease rapidly with increasing axial position. This result is surprising for a finite cylinder and implies that the interior acoustic field is dominated by a near field in the source plane. The slight increase in the pressure levels at $x/a = 1.6$ are a result of a second peak in the axial standing wave. However, this standing wave peak is significantly lower than the dominant peak in the source plane. Thus, even for the finite unstiffened cylinder used in this experimental investigation the majority of the acoustic energy in the shell is located in a localized axial region near the source plane. This result supports the infinite shell model used in reference 4. Figures 19-21 also reveal that when the synchrophase angle is close to its optimum value then the sound pressure levels measured at various x/a positions are much closer in value. Thus, the main effect of synchrophasing is to eliminate the high acoustic near-field located near $x/a = 0.0$, causing the interior acoustic field to be more uniform.

The results of Figs. 8-21 indicate that the optimum synchrophase angle varies significantly with interior location. However, control of the interior acoustic field is needed only in the regions of high pressure response (e.g., $> 95\text{dB}$). In these regions, all the optimum synchrophase angles tend to converge near a single value of $\phi = 200$ degrees. Thus, a significant reduction in the interior pressure response can still be achieved in the regions of high acoustic levels. This reduction is not achieved at the expense of significantly increased

pressure response at other interior locations. In fact, the optimization tends to reduce the large pressure gradients within the shell and thus make the interior acoustic field more uniform. At an optimum synchrophase angle of $\phi = 200$ degrees, potential noise reductions of up to 20dB are achieved at some interior locations. Also, the global pressure response is reduced to below 95dB at all interior microphone locations.

4.2 Driving Frequency of 708 Hz

The results presented below are from the case with pure tone source frequency of 708 Hz. This frequency is again within the range of typical scaled fundamentals of the propeller noise. The driving frequency was changed to study the effects of frequency on synchrophasing. Figures 22(a) and 22(b) show a comparison of the axial and circumferential pressure distributions on the exterior of the cylinder for synchrophasing angles of $\phi = 0$ and 180 degrees. The results for the axial and circumferential pressure distributions for the 708 Hz case are very similar to those recorded for the 680 Hz case, hence, similar conclusions can be drawn. The nonsymmetric circumferential pressure distribution for synchrophase angle $\phi = 180$ degrees is probably due to slight microphone/source positioning errors.

Figure 23 shows the relative circumferential modal amplitudes of the cylinder versus synchrophase angle in the source plane for circumferential modes $n = 0$ to 4. As for the 680 Hz case, the modal response of the cylinder is dominated by the A_2 circumferential mode. The results of this case are again generally similar to the analytical

results. The minor discrepancies between these results and the analytical results are due to cylinder imperfections as discussed previously.

Figure 24 shows the axial distribution of the radial displacement of the cylinder in the source plane for synchrophase angles of $\phi = 0$ and 180 degrees. The radial vibration of the shell decreases dramatically outside a localized region of about one cylinder radius on either side of the source plane. This result supports the theory that the majority of the interior acoustic excitation occurs in a localized axial region near the source plane. This result also gives additional support to the infinite shell model utilized in reference 4. When the synchrophase angle is $\phi = 180$ degrees, the radial displacement is relatively constant with x/a . This again illustrates that the main effect of synchrophasing is to reduce the large cylinder responses located around the source plane ($x/a = 0.0$).

Figure 25 shows the relative radial displacement and phase of the cylinder in the source plane (i.e., $x/a = 0.0$) for synchrophase angles of $\phi = 0$ and 180 degrees. For the 708 Hz case, the relative radial displacement is approximately symmetric as expected for symmetrically positioned sources as shown in Fig. 2. Figure 25 also shows very closely the mode shape of the A_2 mode with two definite nodal lines. In this case, the amplitude of the remaining modes are comparatively lower than for the $f = 680$ Hz case and consequently the A_2 mode is more clearly demonstrated. The radial displacement reduces significantly for a synchrophase angle of $\phi = 180$ degrees indicating again the potential for vibration control as well as interior noise control.

Figures 26-30 show the interior pressure measurements versus syn-

chrophase angle in the source plane ($x/a = 0.0$) at the three radial microphone stations for circumferential positions $\theta = 0, 45, 90, 135$, and 180 degrees, respectively. The results and conclusions are generally similar to those of Figs. 8-12.

Figures 31, 32, and 33 show the interior pressure measurements versus synchrophase angle in the source plane ($x/a = 0.0$) at the six circumferential microphone positions for radial stations $r/a = 0.150, 0.513$ and 0.925 , respectively. The interior pressure measurements versus synchrophase angle for $\theta > 90$ degrees varies as a mirror image of the results for $\theta < 90$ degrees. This result is expected due to the symmetric source loading.

Figures 26, 34, 35, and 36 show the interior pressure measurements versus synchrophase angle at $\theta = 0$ degrees for the three radial microphone stations at axial positions $x/a = 0.0, 0.4, 0.8$ and 1.6 , respectively. At all four axial positions there is a sharp reduction in the radial pressure distribution from the shell wall to the shell centerline.

Figures 37, 38, and 39 show the interior pressure measurements versus synchrophase angle at $\theta = 0$ degrees for the four axial microphone positions at radial stations $r/a = 0.150, 0.513$, and 0.925 , respectively. As in the 680 Hz case, the interior pressure levels at the three radial microphone stations are very high in the source plane and decrease rapidly with increasing axial position. As discussed earlier, this result supports the infinite shell theory of reference 4.

The results of Figs. 26-39 indicate that the optimum synchrophase angle varies significantly with interior location. The pressure re-

sponse at radial position $r/a = 0.150$ tends to be consistently in excess of 10dB below the pressure response at the other microphone locations. Thus, in evaluating an overall optimum synchrophase angle, the results at radial position $r/a = 0.150$ need not be considered. In contrast to the 680 Hz case, the remaining regions of high pressure response still have a wide range of optimum synchrophase angles. This result decreases the global potential noise reduction significantly. For an optimum synchrophase angle of $\phi = 250$ degrees, the global noise reduction is limited to less than 7dB in the source plane, however, the interior acoustic field does tend to be more uniform at this synchrophase angle. This wide range of optimum synchrophase angles is probably due to contributions from two well-coupled modes with contrasting optimum synchrophase angles. The synchrophasing technique can be effective in controlling contributions from a set of modes with an optimum synchrophase angle of $\phi = 0$ degrees or a set of modes with an optimum synchrophase angle of $\phi = 180$ degrees, but the effectiveness of the technique is seriously impaired by significant contributions from both sets of contrasting modes. In regions where the contributions one of the two contrasting modes was minimal (e.g., at $\theta = 90$ degrees), the localized noise reduction was greatly improved. Thus synchrophasing does appear to be an effective noise control technique but the technique can effectively control only one of the two sets of contrasting modes of comparable amplitude.

4.3 Effect of Interior Acoustic Damping Material

The results presented below are from the case with pure tone source

conditions of 708 Hz and a layer of 12.7 mm thick flexible polyurethane polyester foam covering 145 degrees on the bottom inside of the cylinder. The exterior pressure distributions in the axial and circumferential directions are assumed to be identical to those recorded from the previous case without the internal polyester foam and therefore were not repeated.

Figure 40 shows the relative circumferential modal amplitudes of the cylinder versus synchrophase angle in the source plane for circumferential modes $n = 0$ to 4. The modal response of the cylinder is dominated by the A_2 mode except near its optimum synchrophase angle of $\phi = 180$ degrees. Near $\phi = 180$ degrees, the modal response of the cylinder is dominated by the A_3 and A_1 modes both of which have an optimum synchrophase angle near $\phi = 0$ degrees. In contrast to the 680 Hz case, the modes are somewhat decoupled apparently due to the presence of the foam, indicating that the internal acoustic field may play some role in modal coupling. Deviations from the theoretical modal composition of the cylinder are relatively minor and are probably due to cylinder imperfections, slight source asymmetries, and the presence of the polyester foam in the cylinder.

Figure 41 shows the relative radial displacement and phase of the cylinder in the source plane ($x/a = 0.0$) for synchrophase angles $\phi = 0$ and 180 degrees. The relative radial displacement is nearly symmetric as expected for a symmetrically loaded cylinder. The radial displacement again decreases significantly for a synchrophase angle of $\phi = 180$ degrees indicating the potential for vibration control as discussed earlier. Again the presence of the foam can be seen to have "cleaned

up" (i.e., decoupled) the cylinder mode shapes.

Figure 42 shows the interior pressure measurements versus synchrophase angle in the source plane ($x/a = 0.0$) at the three radial microphone stations for circumferential position $\theta = 0$ degrees. The peak sound pressure level at this circumferential position is 98 dB. The interior pressure levels have been reduced significantly from the previous two cases due to the absorption from the polyester foam. The potential noise reduction is about 10-13 dB at all three microphone stations. The optimum synchrophase angle is about $\phi = 120$ degrees for radial stations $r/a = 0.513$ and 0.925 and about $\phi = 200$ degrees for radial station $r/a = 0.150$. As before, these results can be explained by considering the radial vibration of the cylinder. At $\theta = 0$ degrees, the B_n modes theoretically do not contribute to the interior acoustic field. The dominant mode excited in the cylinder is the A_2 mode over most of the range of synchrophase angles, however, near $\phi = 180$ degrees, the A_1 and A_3 modes dominate the shell response. This results in limited potential noise reduction and synchrophase angles somewhat shifted off the $\phi = 180$ degrees position as can be seen in Fig. 42 for radial microphone stations $r/a = 0.513$ and 0.925 . The results at $r/a = 0.150$ are due to the reduced contributions from all the modes except the A_0 mode which results in an optimum synchrophase near $\phi = 180$ degrees. However, it can be seen from Figures 42-46 that significant sound reduction due to synchrophasing can still be obtained with a damped interior acoustic space. In addition, the synchrophase curves are generally similar to the case without damping. This result suggests that the coupled shell-interior acoustic space system is responding in

predominantly in a "shell" type free mode and the interior acoustic field is being forced into motion by the shell response. In other words for the frequencies considered here the interior acoustic field is not being excited at one its natural cavity modes and thus damping does not have a large effect on interior modal response except to reduce the sound levels somewhat due to absorption.

Figure 43 shows the interior pressure measurements versus synchrophase angle in the source plane ($x/a = 0.0$) at the three radial microphone stations for circumferential position $\theta = 45$ degrees. The peak sound pressure level at this circumferential position is about 91 dB indicating again that the need for potential noise reduction at $\theta = 45$ degrees is lessened. The reduction in the interior pressure levels at this position are due to a decrease in the contribution from the dominant A_2 mode. As discussed previously, the A_2 and B_4 modes do not theoretically contribute to the interior acoustic field at $\theta = 45$ degrees. This indicates that the interior acoustic field will be predominantly governed by the A_0 and A_4 modes with an optimum synchrophase angle of $\phi = 180$ degrees and A_1 and A_3 modes which have an optimum synchrophase angle of near $\phi = 0$ degrees. This results in a reduced potential noise reduction and an optimum synchrophase angle between $\phi = 225$ and 360 degrees.

Figure 44 shows the interior pressure measurements versus synchrophase angle in the source plane ($x/a = 0.0$) at the three radial microphone stations for circumferential position $\theta = 90$ degrees. The peak sound pressure level is 100 dB. The results and conclusions of this figure are essentially identical to those of Fig. 10.

Figure 45 shows the interior pressure measurement versus synchrophase angle in the source plane ($x/a = 0.0$) at the three radial microphone stations for circumferential position $\theta = 135$ degrees. The peak sound pressure level is about 92 dB indicating again that the need for noise reduction at this position is minimal. This result is due to the reduced contribution of the dominant A_2 mode at this angle as discussed previously. The reduced potential noise reduction and optimum synchrophase angle at radial stations $r/a = 0.513$ and 0.925 are due to the dominant contributions from the A_0 , A_1 , A_3 , and A_4 modes as discussed for circumferential position $\theta = 45$ degrees. The results at circumferential position $\theta = 135$ degrees should theoretically be a mirror image of the results at $\theta = 45$ degrees. The discrepancies at radial station $r/a = 0.150$ are probably due to a signal-to-noise ratio problem caused by the low pressure response at this location.

Figure 46 shows the interior pressure measurements versus synchrophase angle in the source plane ($x/a = 0.0$) at the three radial microphone stations for circumferential position $\theta = 180$ degrees. As discussed previously, the B_n modes do not theoretically contribute to the interior acoustic field at this circumferential position. This results in dominant A_2 and A_3 modes which have optimum synchrophase angles of $\phi = 180$ and 0 degrees, respectively. This, in turn, causes reduced potential noise reductions and optimum synchrophase angles near $\phi = 270$ degrees. The lack of good potential noise reduction at $r/a = 0.150$ as observed at circumferential position $\theta = 0$ degrees is again probably due to a signal-to-noise ratio problem, however, the need for noise control at either of these locations is minimal.

Figures 42-46 all show a rapid decrease in the interior acoustic field near the centerline of the cylinder. As discussed previously, the reduction in the acoustic field is due to the characteristic that all modes except the $n = 0$ mode have very low pressure amplitudes near the shell centerline.

Figures 47, 48, and 49 show the interior pressure measurements versus synchrophase angle in the source plane at the six circumferential microphone positions for radial stations $r/a = 0.150$, 0.513 , and 0.925 , respectively. As in the previous two cases, the interior pressure measurements versus synchrophase angle for $\theta > 90$ degrees generally vary as a mirror image of the results of $\theta < 90$ degrees. This result is not surprising considering the symmetric source loading.

Figures 42, 50, 51 and 52 show the interior pressure measurements versus synchrophase angle at $\theta = 0$ degrees for the three radial microphone stations at axial positions $x/a = 0.0$, 0.4 , 0.8 , and 1.6 , respectively. A rapid reduction in the radial pressure distribution near the shell centerline is observed at all four axial positions.

Figures 53, 54, and 55 show the interior pressure measurements versus synchrophase angle at $\theta = 0$ degrees for the four axial microphone positions at radial stations $r/a = 0.150$, 0.513 , and 0.925 , respectively. The interior axial pressure distribution at all three radial stations is generally more uniform than either of the previous two cases without foam. This result is due to absorption of sound by the polyester foam located on the interior of the cylinder.

The results of Figs. 42-55 again indicate that the optimum synchrophase angle varies significantly with interior location. As in the

previous cases, the pressure response at radial position $r/a = 0.150$ tends to be consistently low and thus need not be considered when determining an overall optimum synchrophase angle. The remaining regions of high pressure response again have a wide range of optimum synchrophase angles. This result is due to the same reasons as given for the previous case. The overall optimum synchrophase angle for this case appears to be around $\phi = 180$ degrees. This reduces the interior response to below 96dB at all the interior microphone locations. This represents a global reduction of around 5dB indicating again the loss in effectiveness of the synchrophasing technique when significant contributions from two contrasting modes are present. Similar to the previous case, in a region where theoretically one set of contrasting modes do not contribute to the interior pressure response (e.g., at $\theta = 90$ degrees), the potential noise reduction is significantly enhanced. Thus, the synchrophasing technique can effectively control the contributions from one of the two sets of contrasting modes, however, an alternate technique is needed to control the remaining set of modes.

The results of Figs. 5(a), 21, 22(a), 39, and 55 show that the axial shell insertion loss varies dramatically with synchrophase angle for all three cases. Thus, stabilization of the relative rotational phase of each propeller is essential before meaningful interior noise measurements can be obtained. This result supports the use of the experimental model for preliminary investigations since the synchrophase angle can be easily fixed, eliminating fluctuations in the interior acoustic field. The insertion loss presented by the shell wall is also better physically interpreted as a loss due to the modal response of the

whole continuous cylinder surface rather than an attenuation due to a flat plate.

Although an infinite shell model with dipole sources is used in the analytical investigation of reference 4, the predicted synchrophasing characteristics of reference 4 are nearly identical to those obtained in this experimental investigation. The analytical exterior axial and circumferential pressure distributions are similar to those presented in Figs. 5 and 22 even though dipoles were used to model the propeller sources instead of monopoles. The optimum synchrophase angle and degree of attenuation from the analytical investigation closely resemble the results presented here for the various interior microphone positions. Also, the analytical interior pressure distribution at $\theta = 0$ degrees was found to be very sensitive to the synchrophase angle while the exterior pressure distribution was unaffected by the synchrophase angle. Similar experimental results are shown in Figs. 5(a) 21, 22(a), 39, and 55. The analytical interior acoustic field was dominated by a near field in the source plane implying that the majority of acoustic energy flows into the shell in an axially localized region near the source plane. Surprisingly, similar results were obtained for internal pressure amplitude distribution from this experimental investigation even though a finite shell was used. This outcome implies that the end caps have a negligible effect on the interior acoustic field near the source plane primarily due to "forced" response of the interior acoustic field. Thus, the results of this experimental investigation substantiate the assumptions of the infinite shell model used in reference 4.

5. CONCLUDING REMARKS

A simplified model of an aircraft fuselage was used to perform an experimental investigation of synchrophasing. The basic characteristics of synchrophasing have been defined. Potential noise reductions of 10-34 dB were measured throughout the interior of the cylinder with a reasonable bandwidth of reduction. That is, the reduction is not limited to a narrow range of synchrophasing angles, but is present over a relatively wide range of synchrophase angles near the optimum. As discussed previously, this result is critical for the effective use of synchrophasing on multibladed turboprops.

The optimum synchrophase angle and the degree of attenuation varies with interior location and frequency due to the interior acoustic response consisting of a series of modes varying in coordinate position and with differing optimum synchrophase angles. The interior acoustic field of the cylinder was found to be dominated by pressure levels near the source plane thus implying that an infinite cylinder is a reasonable model of an aircraft fuselage. Due to the variation in optimum synchrophase angle with interior location, it will be necessary to optimize a space averaged measure of interior SPL's. The authors suggest that the spatially averaged energy content of the acoustic field may be a more relevant parameter to optimize. This would result in a reduction of energy content of the whole interior field with the emphasis being where the levels are loudest. Also, the synchrophasing technique seems to be an effective noise control method for only one of the two sets of contrasting modes. For optimum noise reduction, an alternate technique is needed to control the remaining set of contrasting modes if present.

A computer algorithm was developed to decompose the modal composition of the cylinder for a range of synchrophase angles. The decomposition algorithm was found to be an essential tool for investigating the mechanisms of sound transmission into the cylinder. Modal decomposition results suggest that transmission of low frequency sound into aircraft cabins is governed by modal cylinder vibration rather than localized transmission. Thus, low frequency sound transmission into an aircraft fuselage is localized in the axial direction but nonlocalized in the circumferential direction. The cylinder response in the circumferential direction from Figs. 25 and 41 could be viewed as being localized. However, to successfully explain the resulting interior pressure response, the global response of the shell must be considered (i.e., the modal response of the shell must be evaluated). Also, the results indicate that the near-field or directional characteristics of propeller sources in a real aircraft strongly determine the cylinder modal response and thus the nature of the transmission phenomena. Asymmetries in the cylinder were found to couple cylinder circumferential modes of vibration. Thus, any type of structural modifications (i.e., internal floors, ribs, etc.) will strongly affect the transmission of sound into the cylinder. Internal acoustic damping was found to have little effect on the measured results except to somewhat reduce the interior sound pressure levels and decouple the circumferential modes, indicating that the internal acoustic field may play some modal coupling roll as well as cylinder asymmetries.

The aircraft fuselage model and experimental procedure utilized in this investigation have been shown to be successful in defining the

characteristics of synchrophasing and other interior noise effects as well as giving insight into the mechanisms of sound transmission into aircraft cabins. The beginning of an experimental data base has been developed, however, further studies are needed to completely understand the synchrophasing concept as well as other interior noise effects. Possible future investigations include studying the effects of multiple pure tones, the presence of an internal floor, asymmetric source loading, ribs, stiffeners, vibrational inputs at the wing attachments, utilizing a secondary vibration control system in conjunction with the synchrophasing, internal damping, and implementing dipole sources instead of monopole sources to investigate the directional influence of the sources.

6. REFERENCES

1. Metzger, F. B., "Strategies for Aircraft Interior Noise Reduction in Existing and Future Propeller Aircraft," SAE Paper 810560, 1981.
2. Johnston, J. F., Donham, R. E., and Guinn, W. A., "Propeller Signatures and Their Use," AIAA Paper 80-1035, 1980.
3. Magliozzi, B., "Synchrophasing for Cabin Noise Reduction of Propeller-Driven Airplanes," AIAA Paper 83-0717, 1983.
4. Fuller, C. R., "Noise Control Characteristics of Synchrophasing--An Analytical Investigation," AIAA Paper 84-2369, 1984.
5. Moore, C. J., "Measurement of Radial and Circumferential Modes in Annular and Circular Fan Ducts," Journal of Sound and Vibration, Vol. 62, No. 2, 1979, pp. 235-256.
6. Silcox, R. J., and Lester, H. C., "Sound Propagation Through a Variable Area Duct: Experiment and Theory," AIAA Journal, Vol. 20, No. 10, 1982, pp. 1377-1384.
7. Mixson, J. S., Barton, C. K., Piersol, A. G., and Wilby, J. F., "Characteristics of Propeller Noise on an Aircraft Fuselage Related to Interior Noise Transmission," AIAA Paper 70-0646, 1979.
8. Yousri, S. N. and Fahy, F. J., "Distorted Cylindrical Shell Response to Internal Acoustic Excitation Below the Cut-off Frequency," Journal of Sound and Vibration, Vol. 52, No. 3, 1977, pp. 441-452.

NOMENCLATURE

A_n	=	complex modal amplitude coefficients, Eq. (1)
a	=	radius of test cylinder, 0.254 m
B_n	=	complex modal amplitude coefficients, Eq. (1)
f	=	frequency
j	=	$\sqrt{-1}$
m	=	$0, 1, 2, \dots, \infty$
N_p	=	number of measuring points
n	=	circumferential mode number
p	=	$1, 2, 3, \dots, N_p$
r, θ, x	=	cylindrical coordinates
t	=	time
w	=	radial displacement
$\Delta\theta_p$	=	$2\pi/N_p$
ϵ	=	constant, $\epsilon = 2$ for $n = 0$; $\epsilon = 1$ for $n > 0$
ϕ	=	synchrophase angle
ω	=	circular frequency

APPENDIX
MODAL DECOMPOSITION ALGORITHM


```

DIMENSION AR(5),AI(5),BR(5),BN(5,50),V(11),PHI(50)
DIMENSION PHAN(5,50),PHBN(5,50),V1(11),PHASE1(11)
DIMENSION WRE(11),WIM(11)
C*****C
C C DEFINE THE INTEGRATION LIMITS AND CONSTANTS C
C C C C
C*****C
PI=3.1415927
A=0.00
B=2.0*PI
C*****C
C C READ THE NUMBER OF BASE POINTS , THE NUMBER OF SYNCHROPHASE ANGLES, C
C C AND THE RADIAL DISPLACEMENT AND PHASE OF THE CYLINDER AT EACH BASE C
C C POINT C
C*****C
WRITE(6,50)
50 FORMAT(/////////)
READ(5,*),M,NPHI
DO 900 K=1,NPHI
  READ(5,*),PHI(K),(W(1),PHASE(1),I=1,M)
C*****C
C C INITIALIZE THE REAL AND IMAGINARY C
C C COMPONENTS OF THE MODAL AMPLITUDES C
C*****C
DO 100 J=1,5
  AR(J)=0.0
  AI(J)=0.0
  BR(J)=0.0

```

```

      BI(J)=0.0
      CONTINUE
C*****
C
C CONVERT PHASE(I) FROM DEGREES TO RADIANS
C
C*****
      DO 150 J=1,M
        PHASE(I)=PHASE(I)*PI/180.0
      CONTINUE
C*****
C
C CALCULATE THE REAL AND IMAGINARY COMPONENTS
C OF THE COMPLEX FUNCTION TO BE INTEGRATED
C
C*****
      DO 200 J=1.5
        N=J-1
        DO 200 I=1,M
          THETA(I)=2.0*PI*(J-1)/M
          AR(J)=AR(J)+V(I)*COS(PHASE(I))*COS(N*THETA(I))
          AI(J)=AI(J)+V(I)*SIN(PHASE(I))*COS(N*THETA(I))
          BR(J)=BR(J)+V(I)*COS(PHASE(I))*SIN(N*THETA(I))
          BI(J)=BI(J)+V(I)*SIN(PHASE(I))*SIN(N*THETA(I))
        CONTINUE
C*****
C
C CALCULATE MODAL AMPLITUDES AND THEIR RELATIVE PHASES
C
C*****
      E=1.0
      IF(N.EQ.0)E=2.0
      AN(J,K)=2.0*SORT(AR(J)**2+AI(J)**2)/(E*M)
      BN(J,K)=2.0*SORT(BR(J)**2+BI(J)**2)/(E*M)

```

```

      PHIBN(I,K)=0.0
      PHIAN(J,K)=ATAN2(AI(J),AR(J))
      IF (J.EQ. 1) GO TO 250
      PHIBN(J,K)=ATAN2(BI(J),BR(J))
250    CONTINUE
C*****
C INITIALIZE THE REAL AND IMAGINARY COMPONENTS
C OF THE REGENERATED RADIAL DISPLACEMENTS
C
C*****
      DO 300 I=1,M
      VRE(I)=0.0
      VIM(I)=0.0
300    CONTINUE
C*****
C REGENERATE THE RADIAL DISPLACEMENT AND PHASE OF THE CYLINDER
C AT EACH BASE POINT BY BACK SUBSTITUTING THE MODAL AMPLITUDES
C INTO THE FOURIER SERIES
C
C*****
      DO 400 I=1,M
      DO 350 J=1.5
      N=J-1
      VRE(I)=VRE(I)+AN(J,K)*COS(PHIAN(J,K))*COS(N*THETA(I))
      +BN(J,K)*COS(PHIBN(J,K))*SIN(N*THETA(I))
      VIM(I)=VIM(I)+AN(J,K)*SIN(PHIAN(J,K))*COS(N*THETA(I))
      +BN(J,K)*SIN(PHIBN(J,K))*SIN(N*THETA(I))
350    CONTINUE
      VI(I)=SQRT(VRE(I)**2+VIM(I)**2)
      PHASE(I)=ATAN2(VIM(I),VRE(I))
400    CONTINUE

```



```

C*****C
DO 700 J=1,M
  IF(PHASE1(J)*180.0/PI
    IF(PHASE1(J).LT.0.0)PHASE1(J)=PHASE1(J)+360.0
    WRITE(6,550)THETA(J),V1(J),PHASE1(J)
  CONTINUE
700  WRITE(6,750)
  FORMAT(//,14X,'OUTPUT MODAL AMPLITUDES',//,
  * 1X,'MODE NO.',9X,'AN',23X,'BN',/)
  DO 850 I=1,5
    N=I-1
    WRITE(6,800)N,AN(I,K),BN(I,K)
    FORMAT(3X,12,8X,F8.3,17X,F8.3)
  CONTINUE
800  CONTINUE
900  CONTINUE
C*****C
C C C C C PRINT THE RELATIVE MODAL AMPLITUDES FOR EACH SYNCHROPHASE ANGLE C C C
C*****C
WRITE(6,950)
950  FORMAT(//,30X,'MODAL AMPLITUDES',/)
  WRITE(6,1000)
1000  FORMAT(1X,'SYNCHRO',5X,'N=0',9X,'N=1',9X,'N=2',9X,
  * 'N=3',9X,'N=4',/, 'ANGLE',/, 'AN',4X,'BN',4X,'AN',4X,
  * 'BN',4X,'AN',4X,'BN',4X,'AN',4X,'BN',4X,'AN',4X,'BN',/)
  DO 1100 K=1,NPHI
    WRITE(6,1050)PHI(K), (AN(J,K),BN(J,K),J=1,5)
    FORMAT(2X,F4.0,2X,10F6.3)
  CONTINUE
1100  CONTINUE
  WRITE(6,1150)
1150  FORMAT(////)
  STOP
  END
C*****C

```

FIGURES

ORIGINAL PAGE IS
OF POOR QUALITY

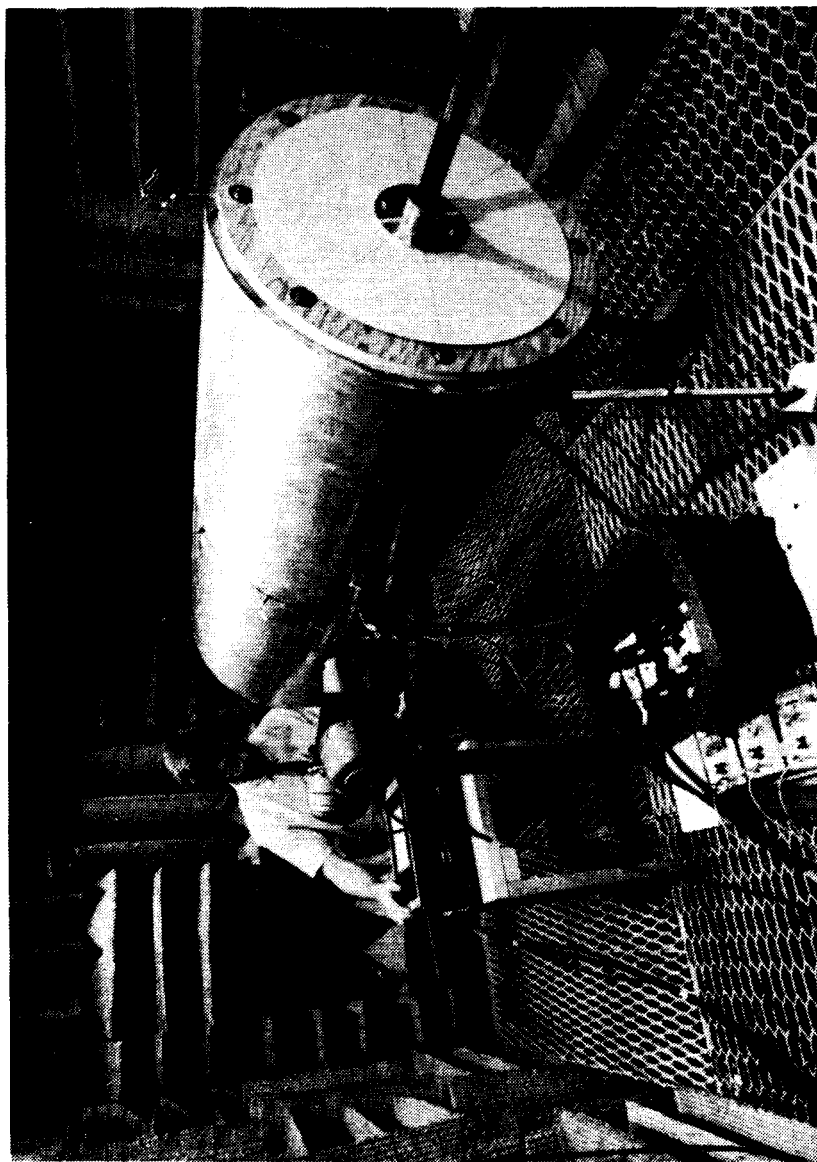


Fig. 1. Photograph of Experimental Setup.

ORIGINAL PAGE
OF POOR QUALITY

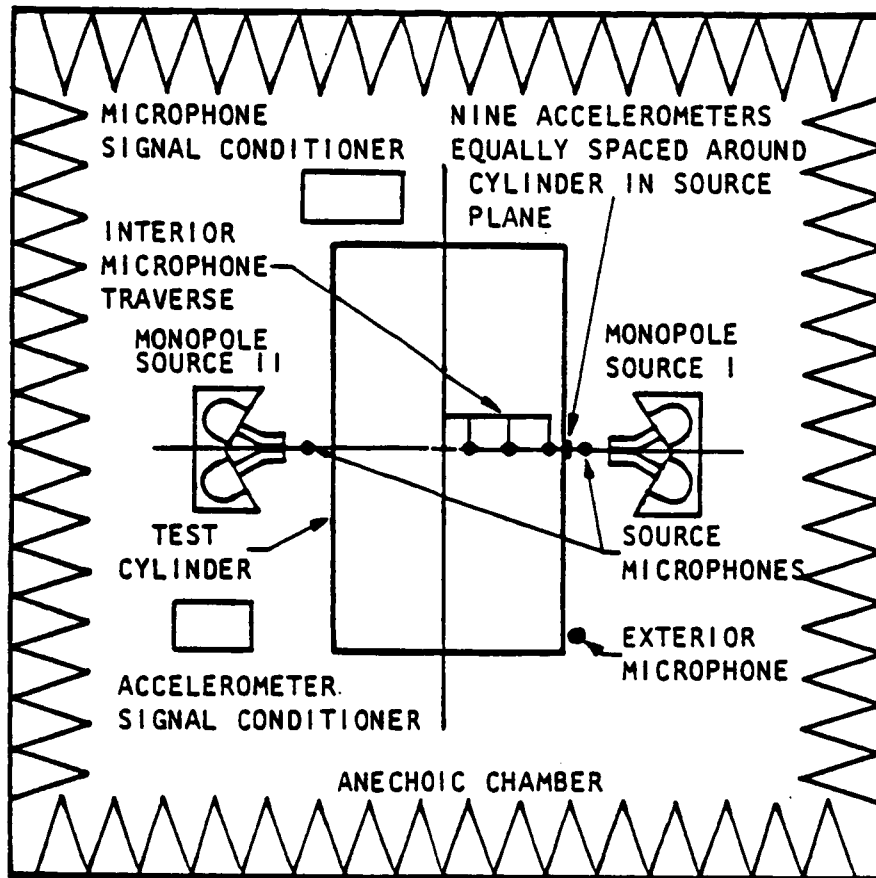
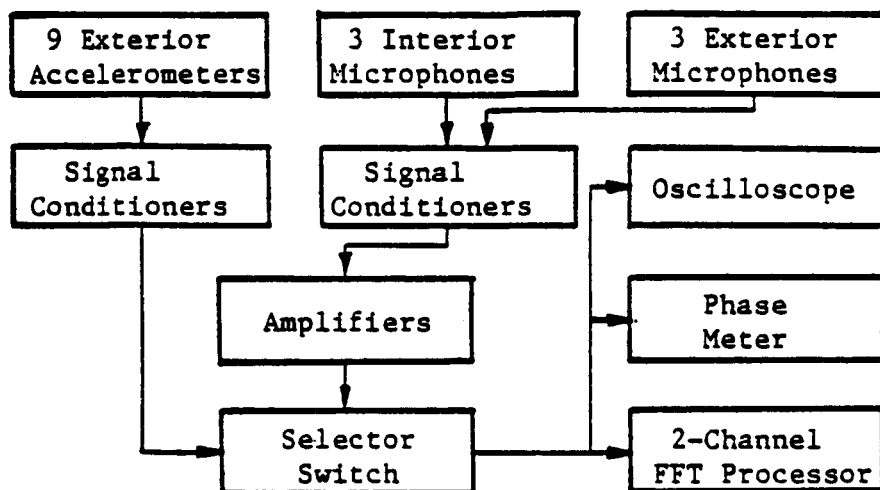
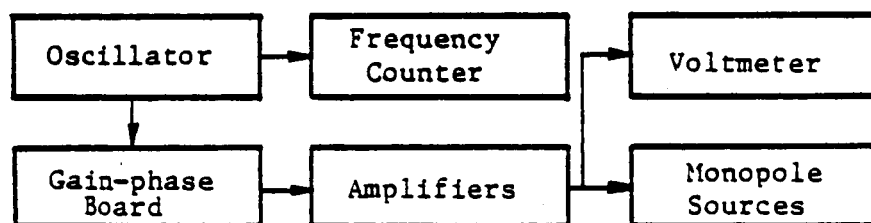


Fig. 2. Schematic Diagram of Experimental Setup.



(a) Data Acquisition System



(b) Source Generation System

Fig. 3. Schematic Diagram of Instrumentation.

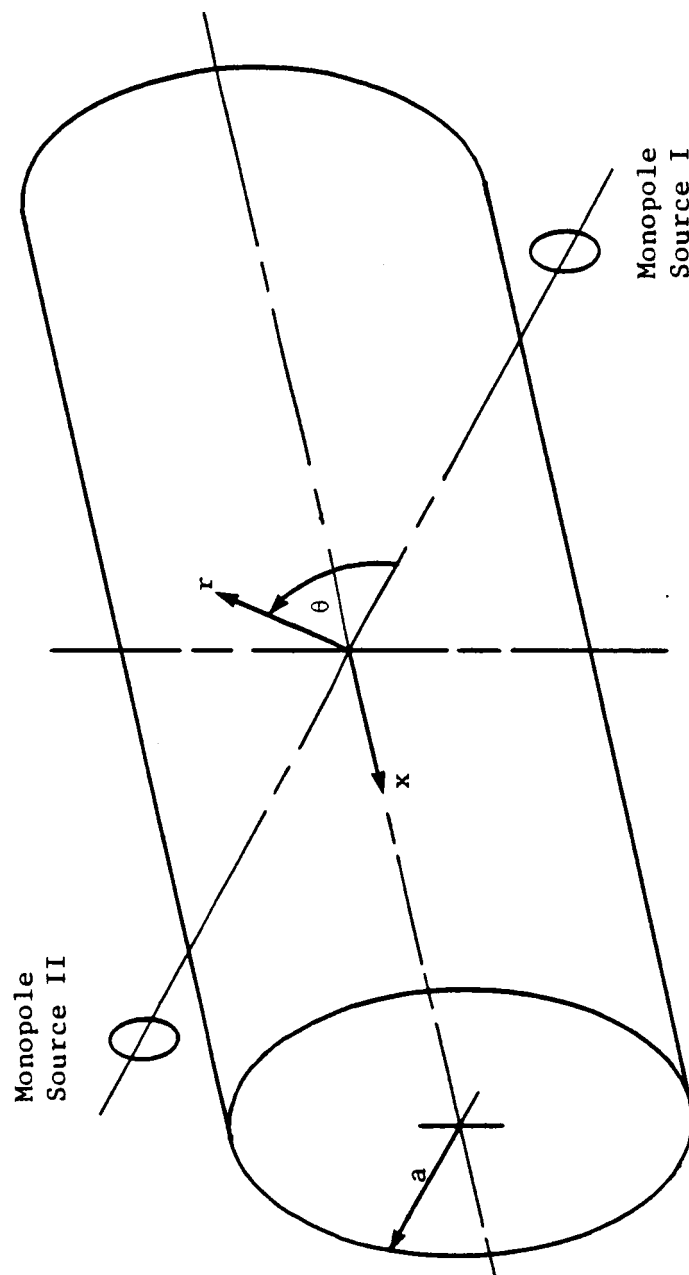
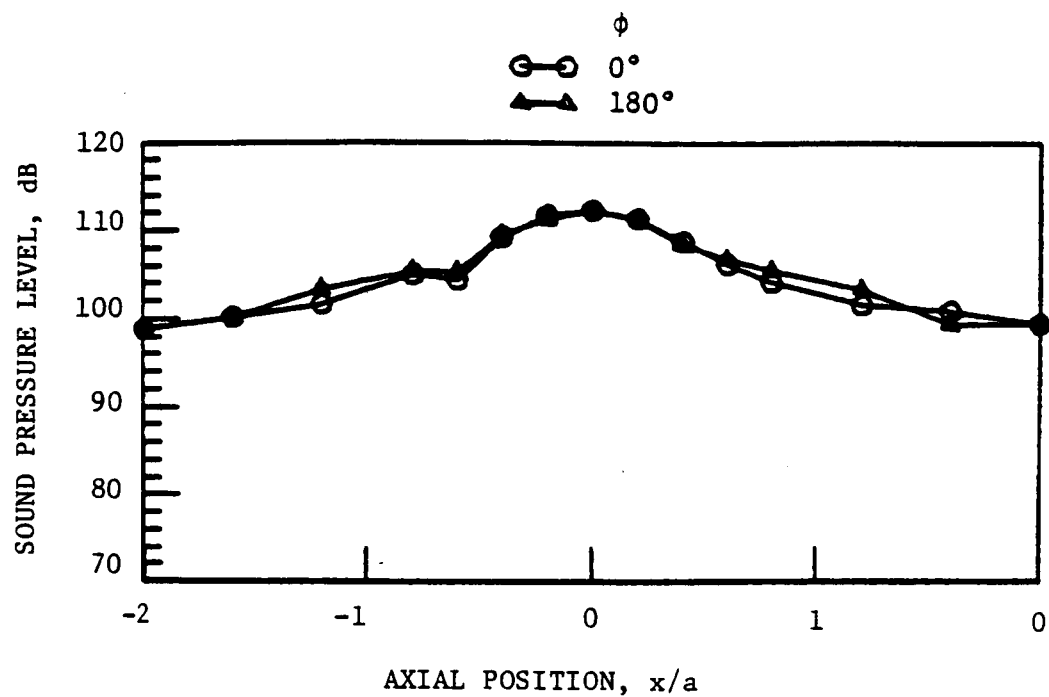
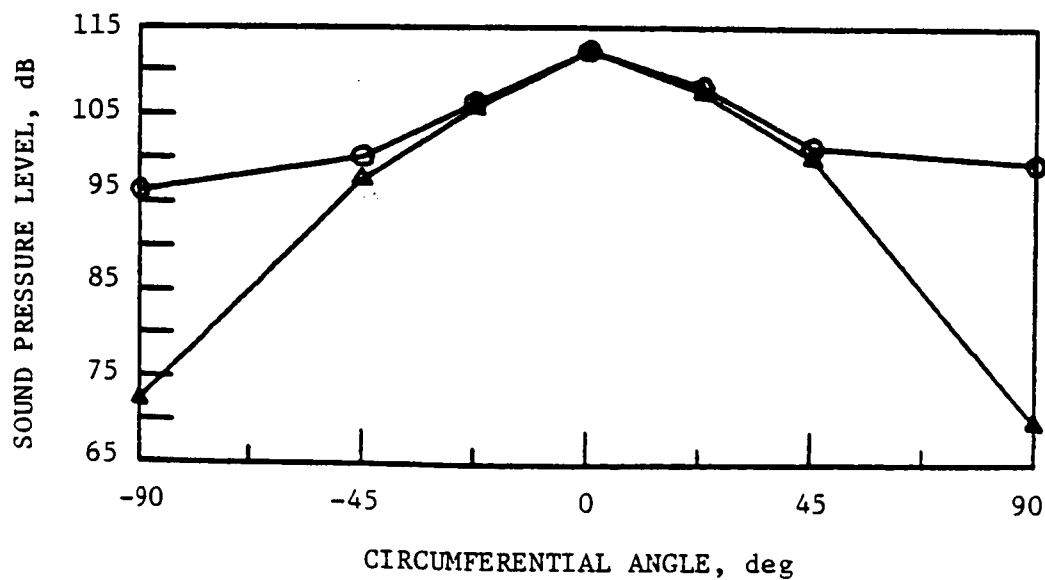


Fig. 4. Coordinate System.



(a) Axial Pressure Distribution at $\theta = 0^\circ$



(b) Circumferential Pressure Distribution at $x/a = 0.0$

Fig. 5. Exterior Pressure Measurements on Cylinder for $f = 680$ Hz.

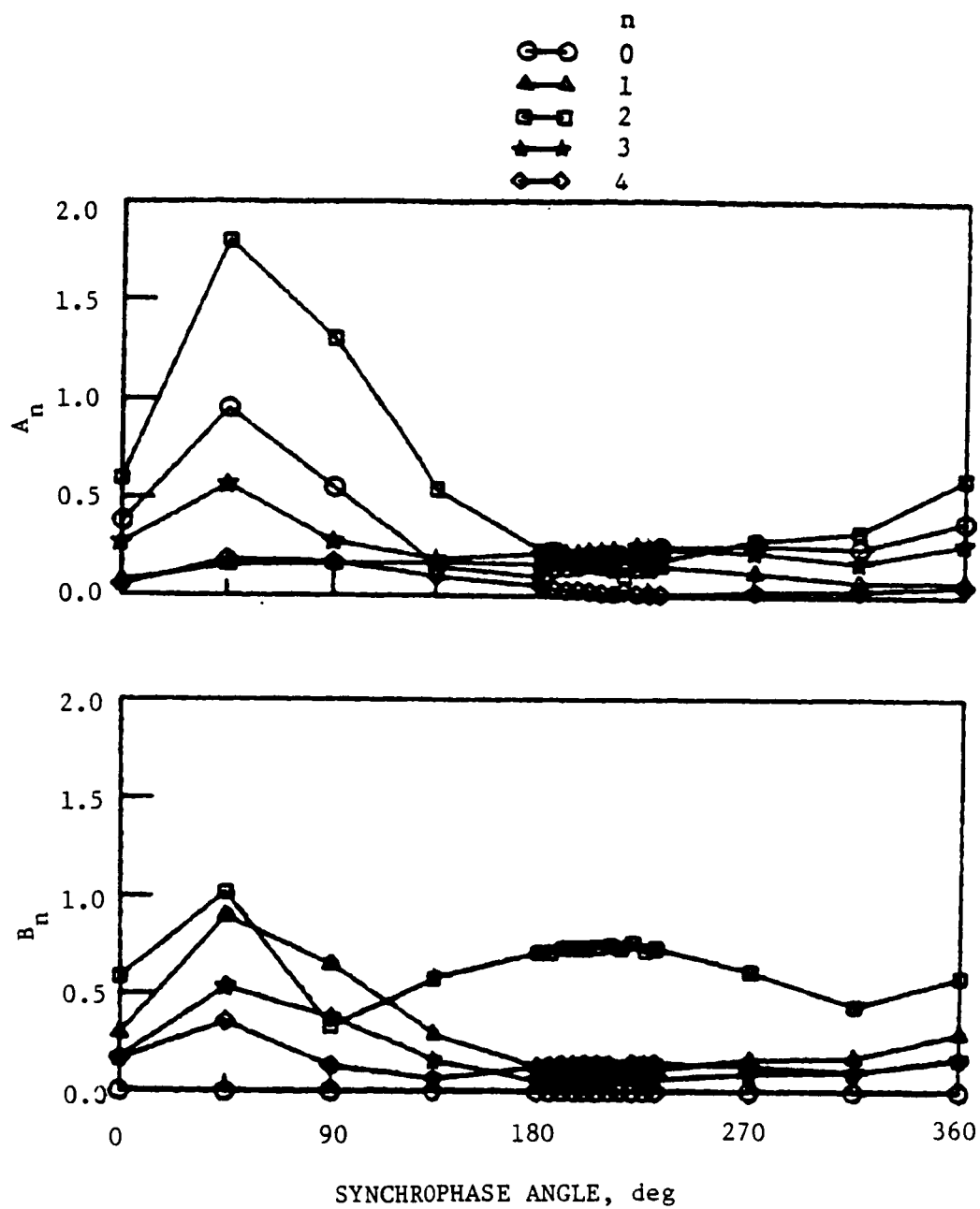


Fig. 6. Relative Modal Amplitudes of the Cylinder at $x/a = 0.0$ and $f = 680$ Hz.

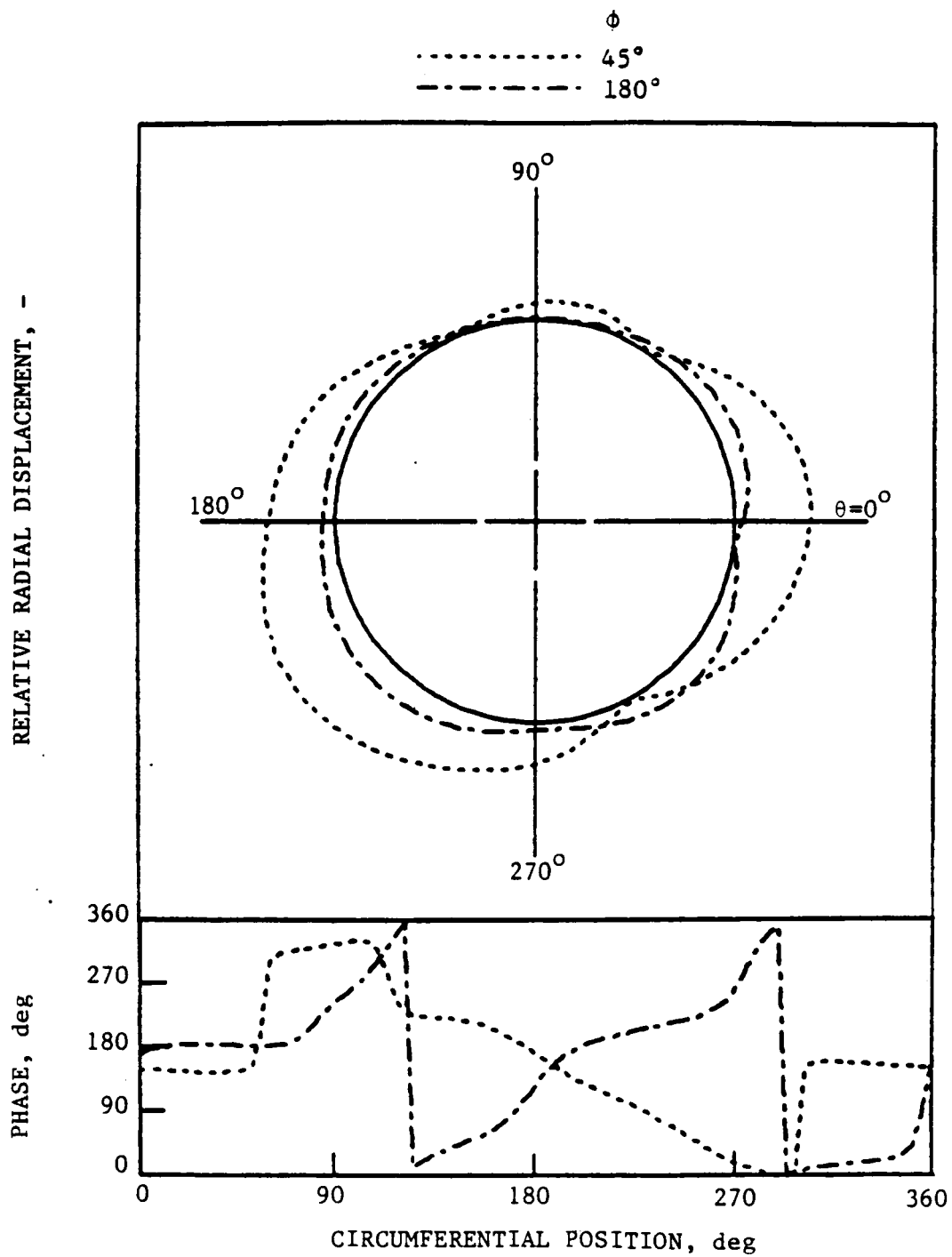


Fig. 7. Relative Radial Displacement and Phase of the Cylinder at $x/a = 0.0$ and $f = 680$ Hz.

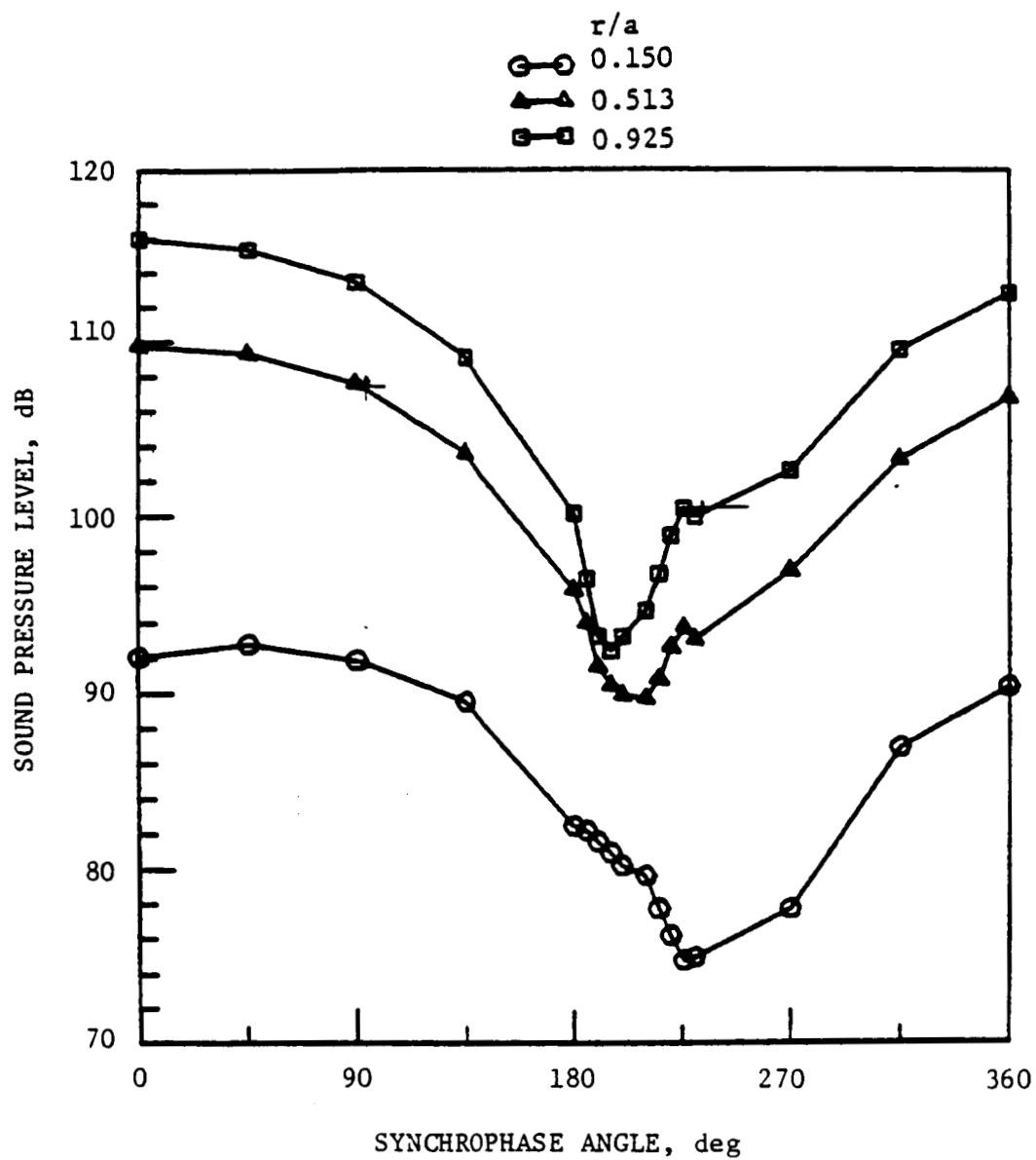


Fig. 8. Interior Pressure Measurements at $x/a = 0.0$, $\theta = 0^\circ$, and $f = 680$ Hz.

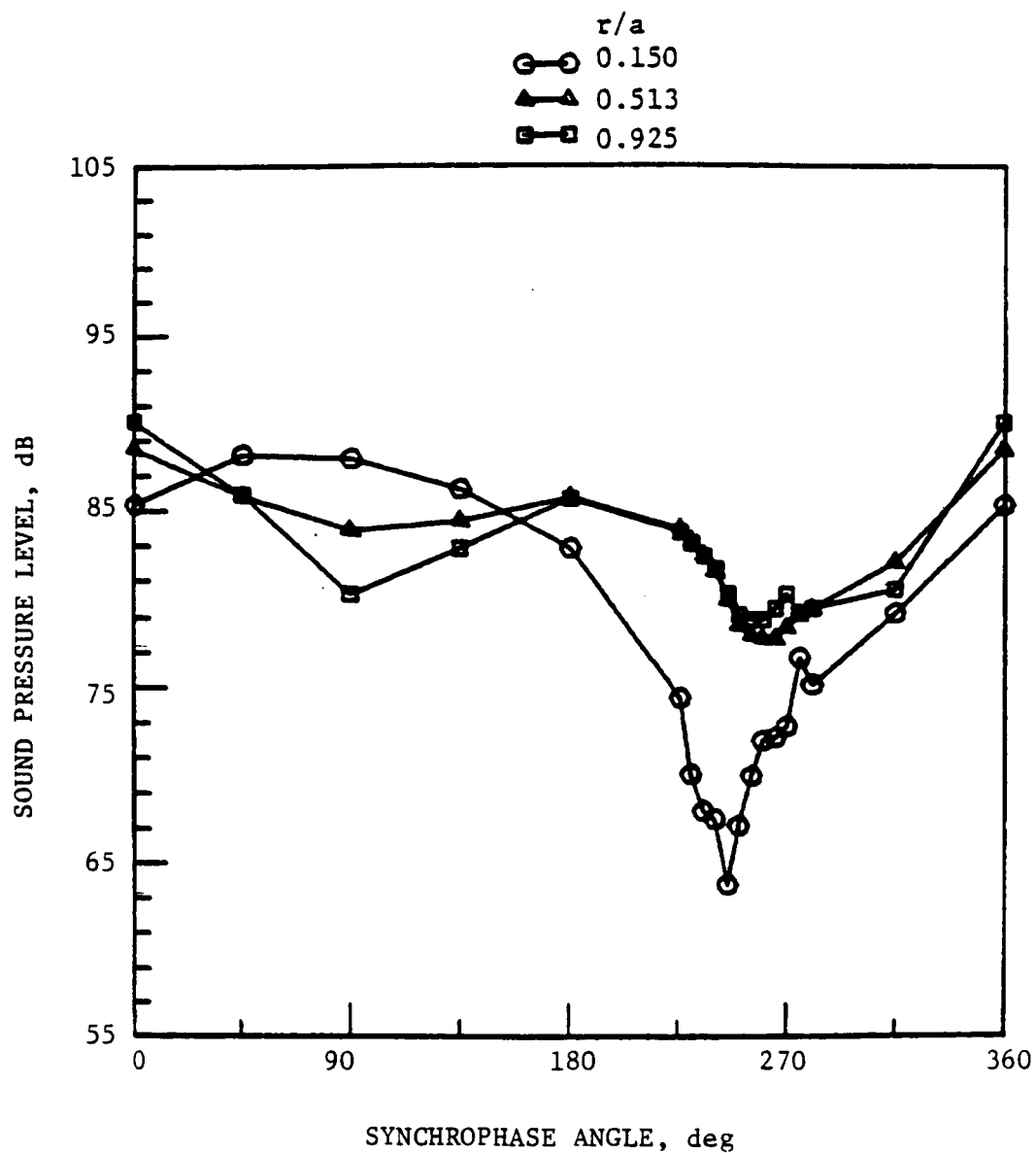


Figure 9. Interior Pressure Measurements at $x/a = 0.0$, $\theta = 45^\circ$, and $f = 680$ Hz.

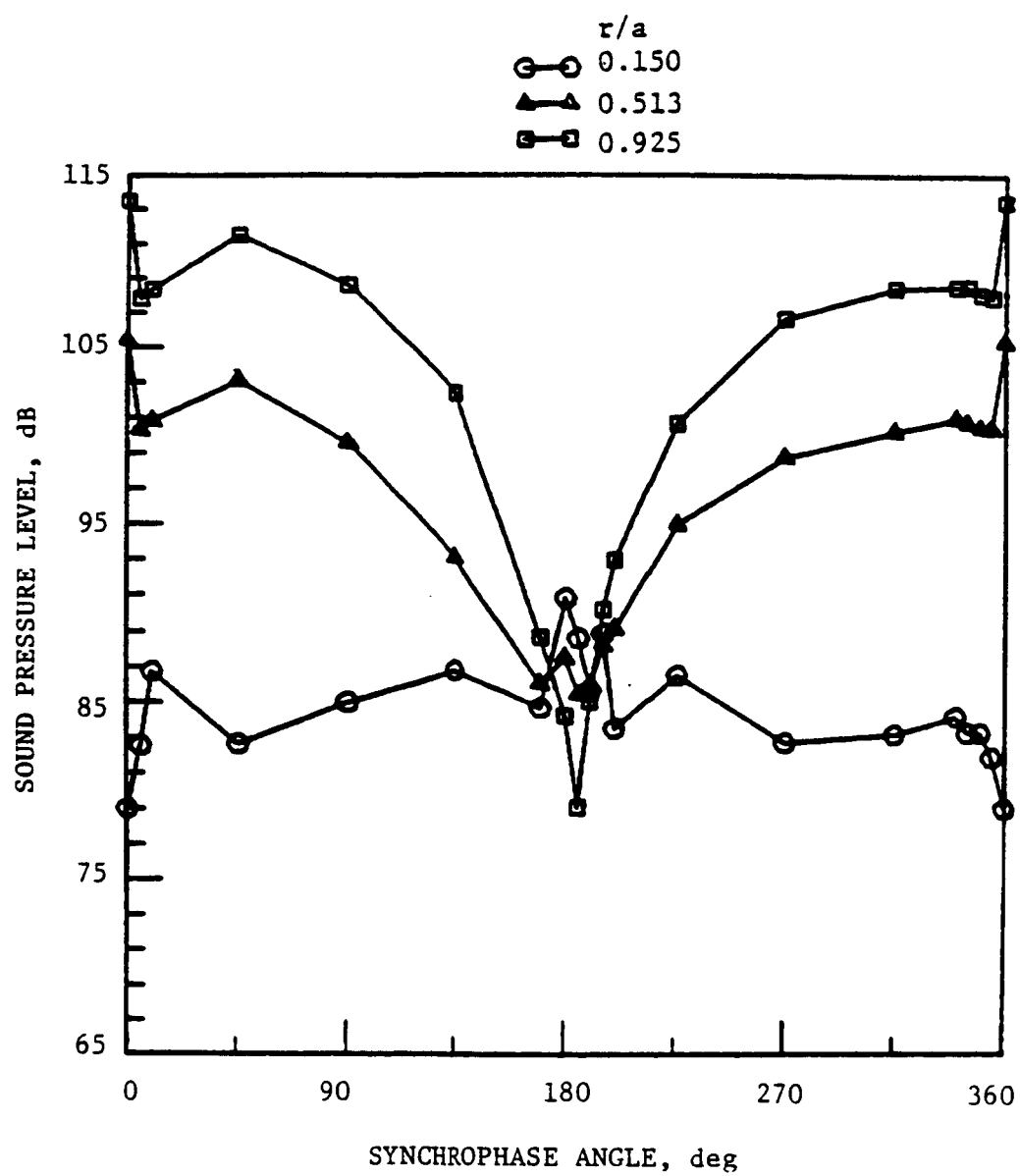


Fig. 10. Interior Pressure Measurements at $x/a = 0.0$, $\theta = 90^\circ$, and $f = 680$ Hz.

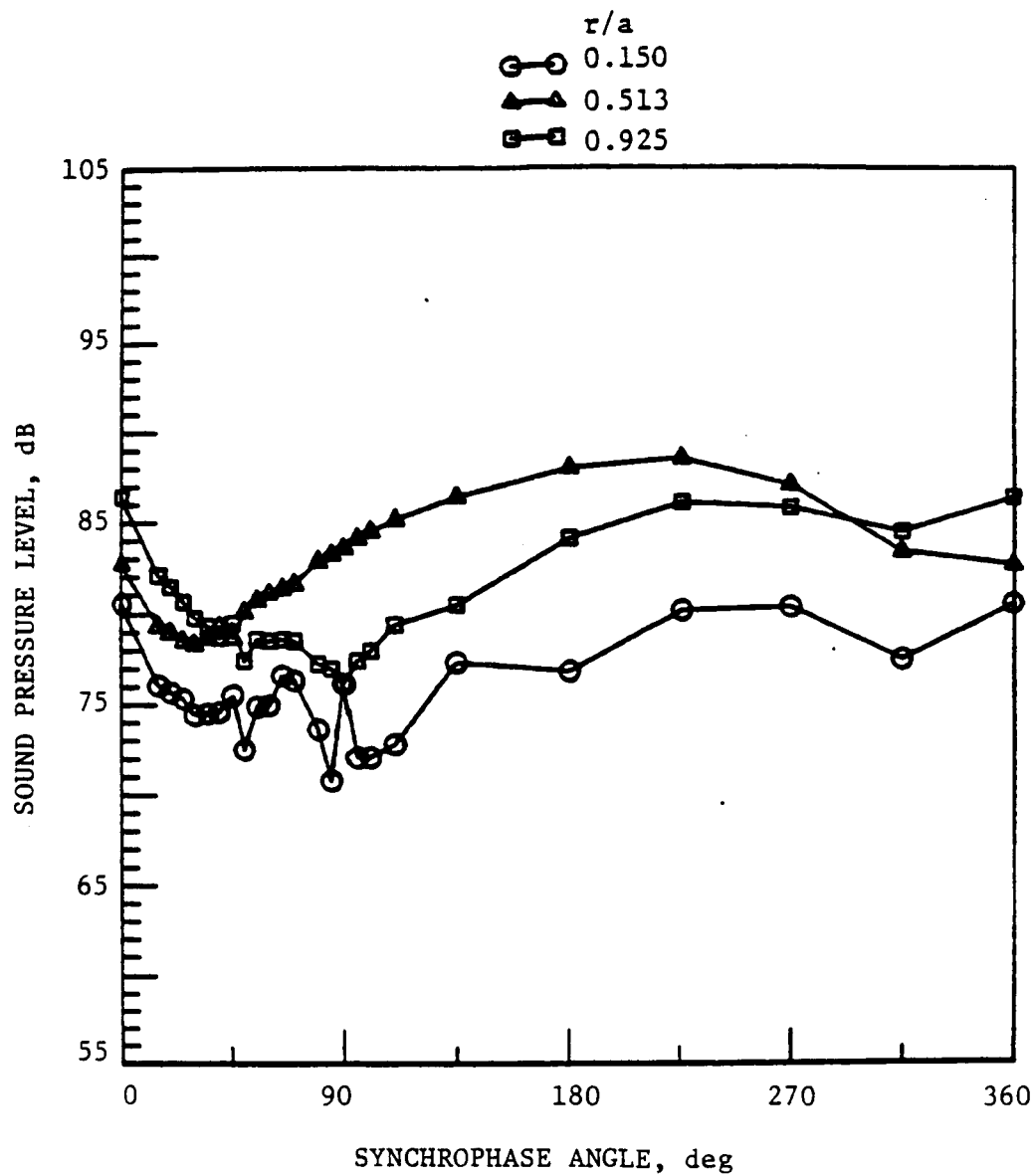


Fig. 11. Interior Pressure Measurements at $x/a = 0.0$, $\theta = 135^\circ$, and $f = 680$ Hz.

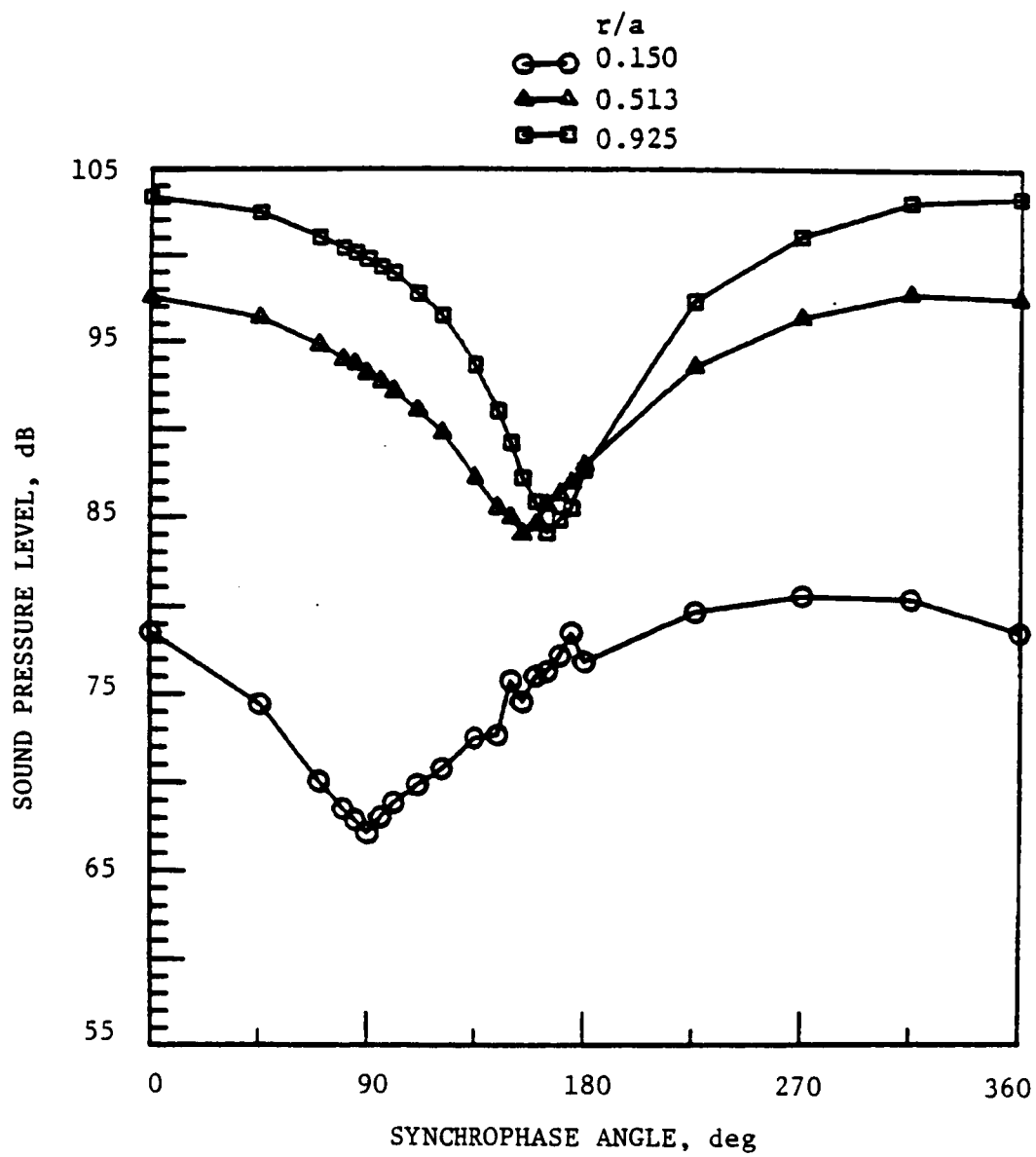


Fig. 12. Interior Pressure Measurements at $x/a = 0.0$, $\theta = 180^\circ$, and $f = 680$ Hz.

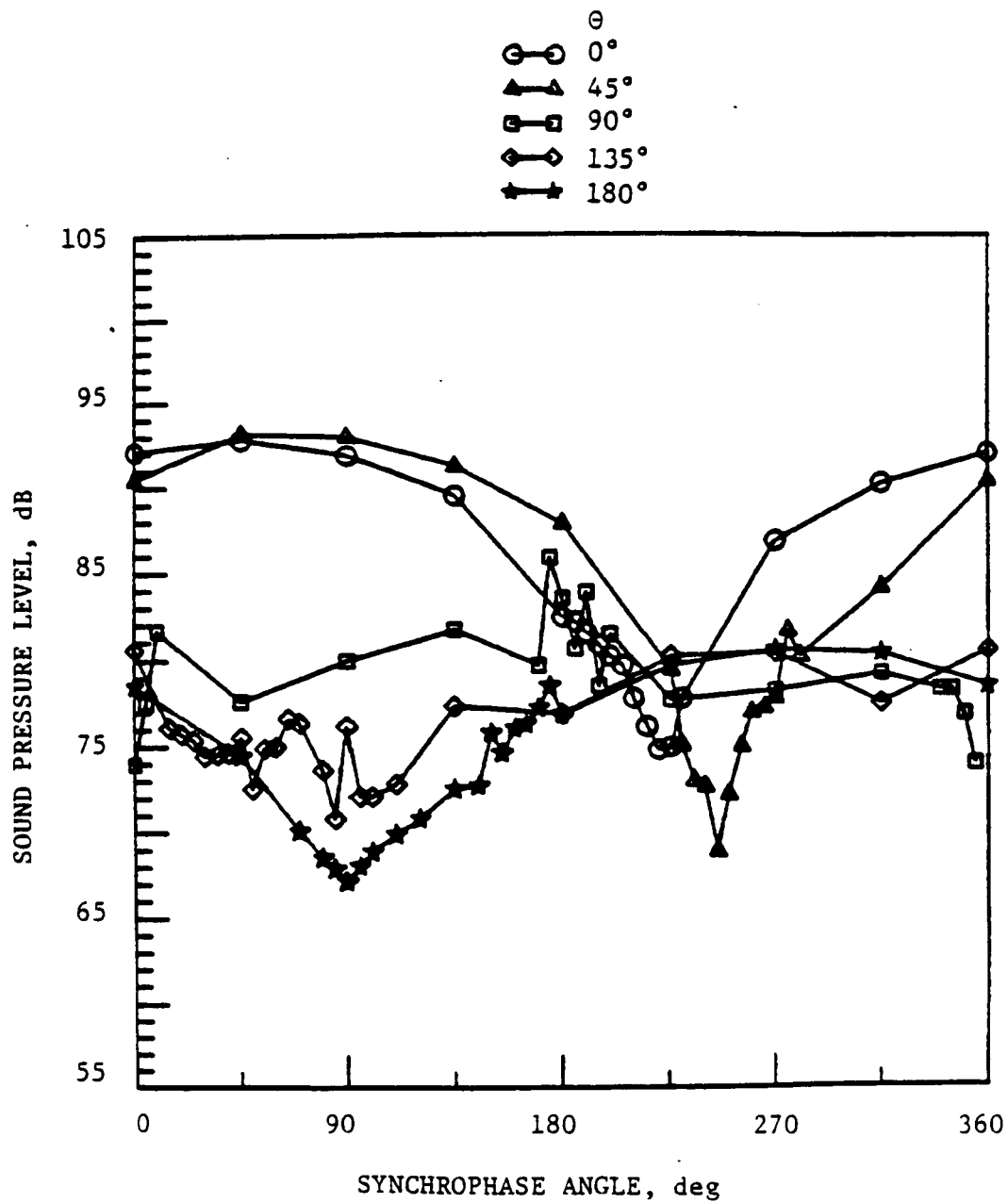


Fig. 13. Interior Pressure Measurements at $x/a = 0.0$, $r/a = 0.150$, and $f = 680$ Hz.

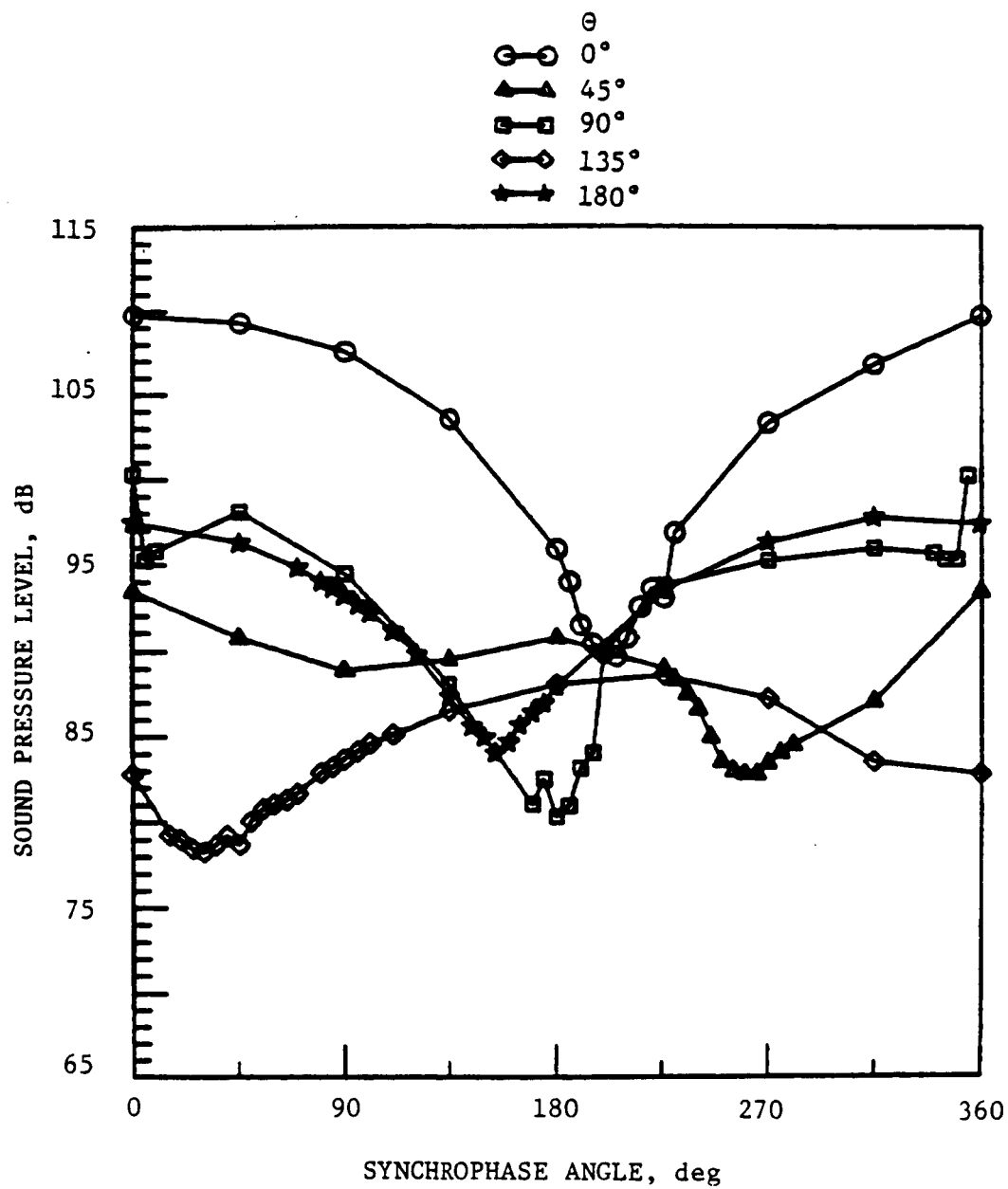


Fig. 14. Interior Pressure Measurements at $x/a = 0.0$, $r/a = 0.513$, and $f = 680$ Hz.

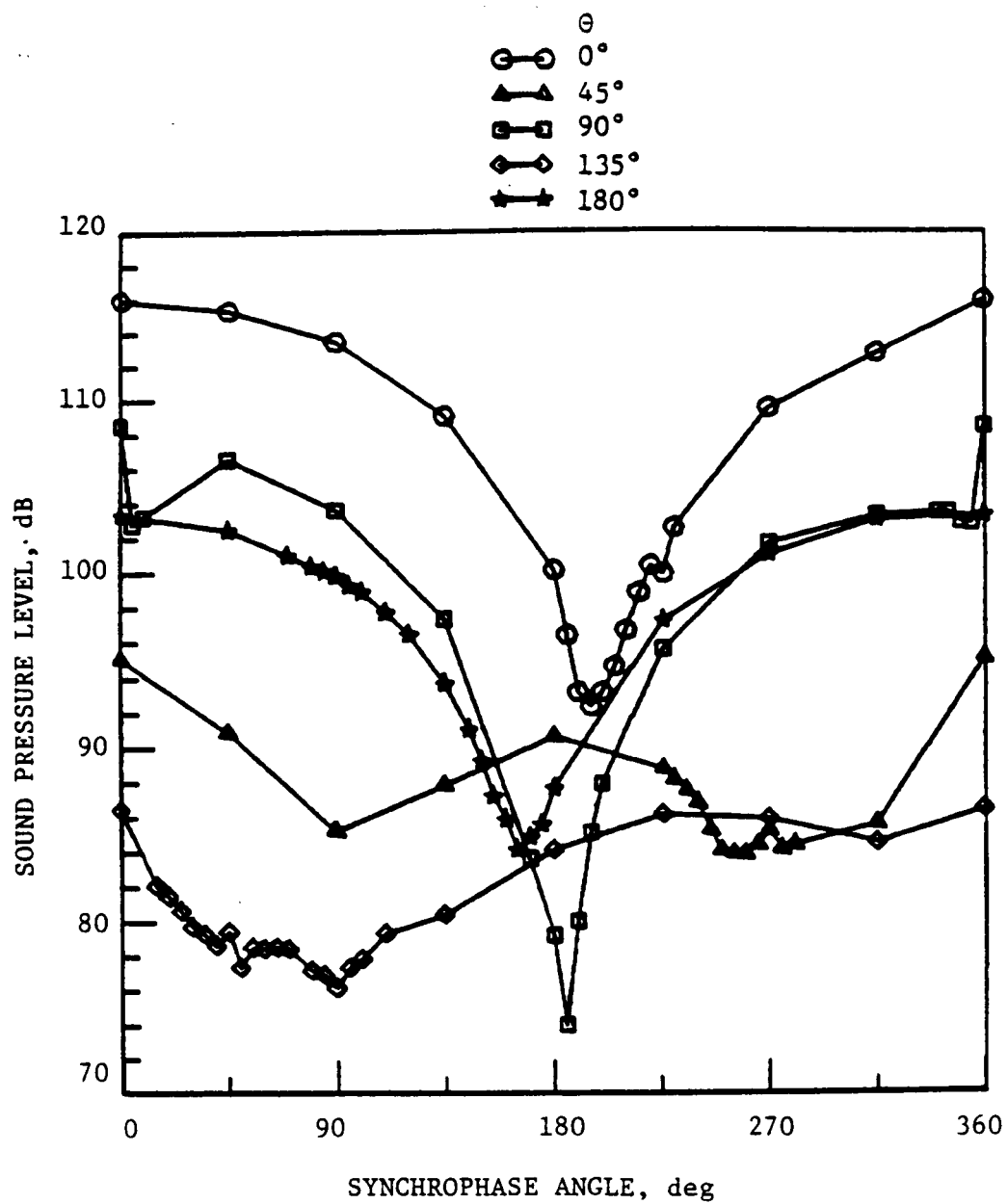


Fig. 15. Interior Pressure Measurements at $x/a = 0.0$, $r/a = 0.925$, and $f = 680$ Hz.

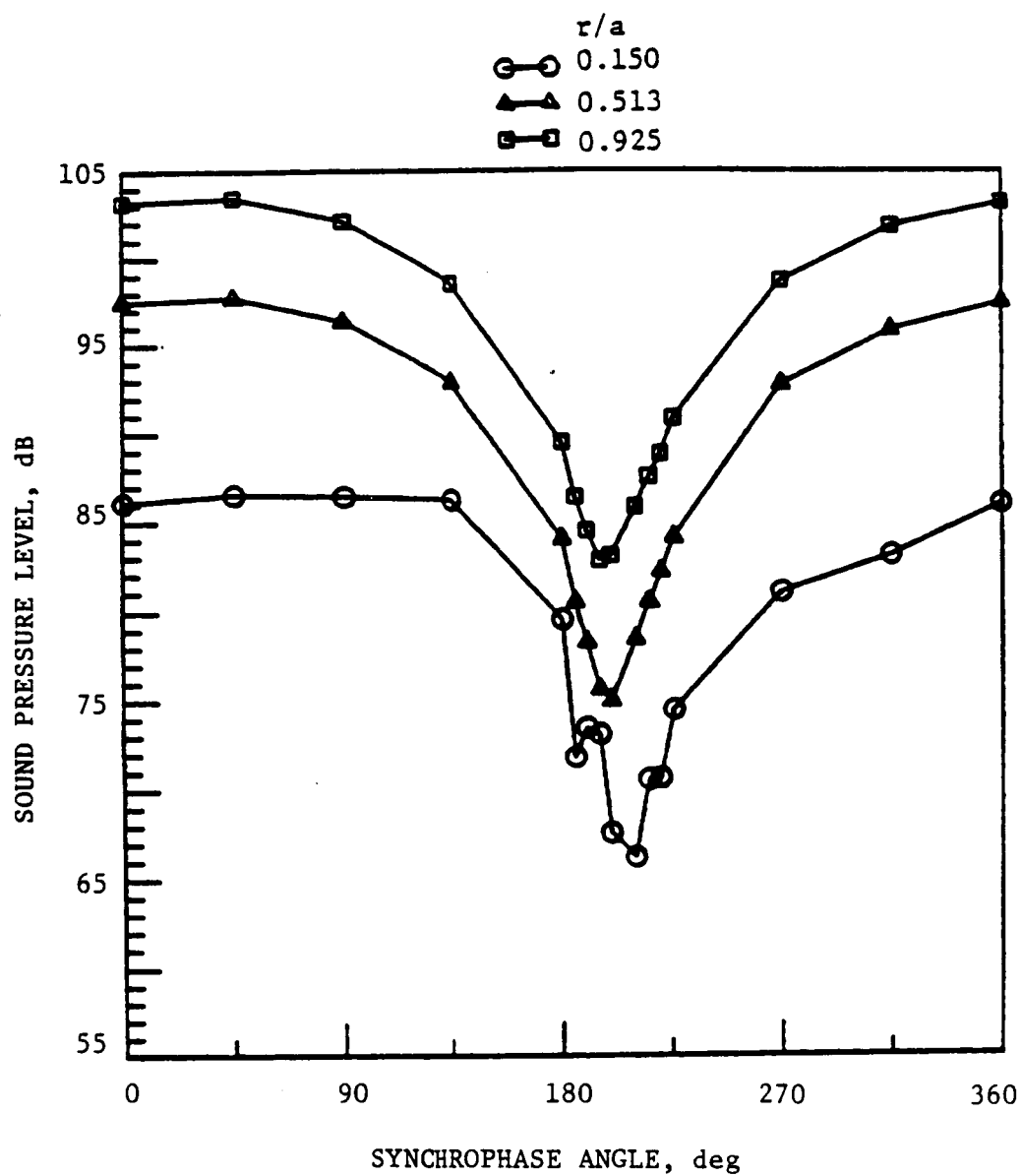


Fig. 16. Interior Pressure Measurements at $x/a = 0.4$, $\theta = 0^\circ$, and $f = 680$ Hz.

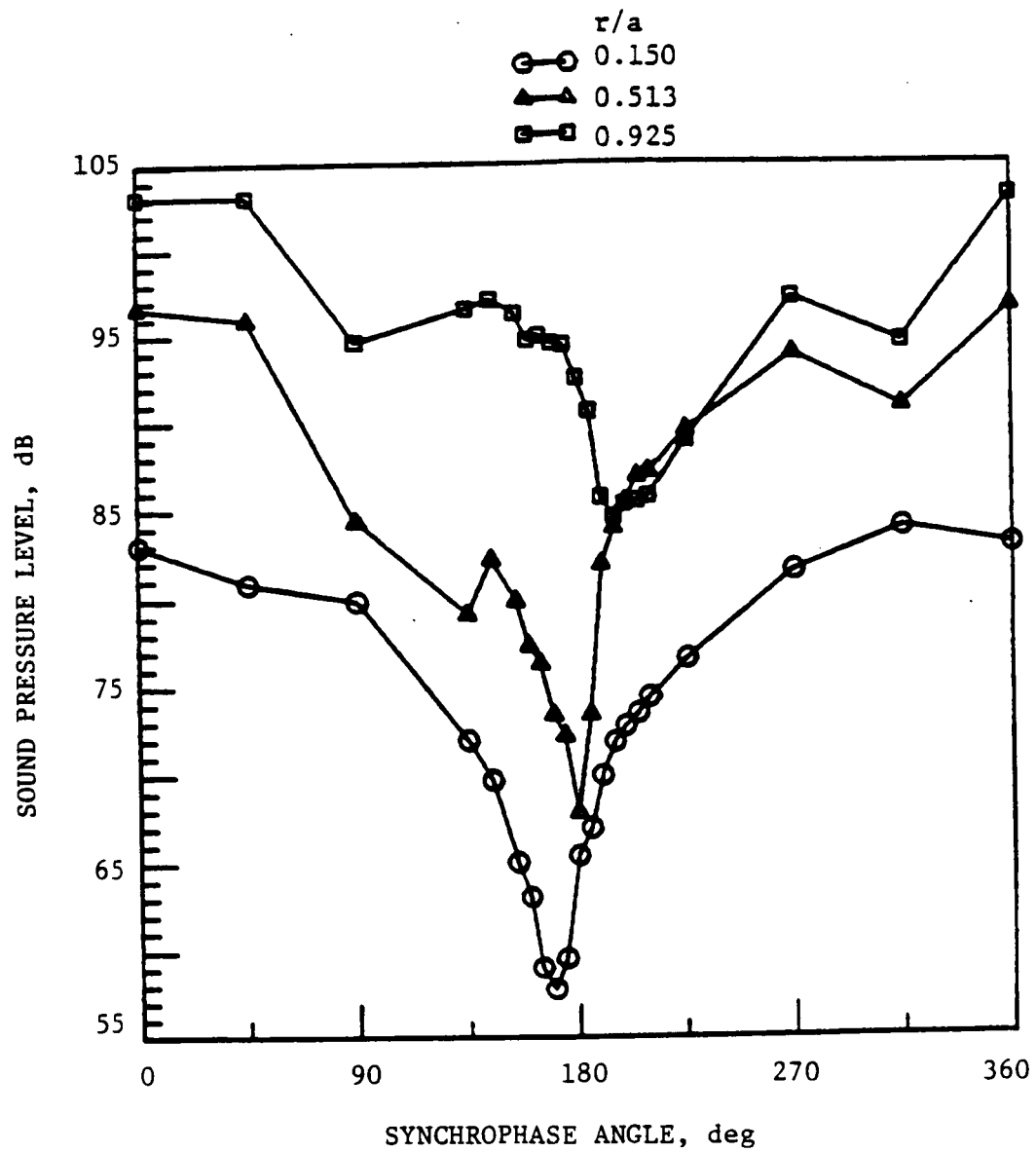


Fig. 17. Interior Pressure Measurements at $x/a = 0.8$, $\theta = 0^\circ$, and $f = 680$ Hz.

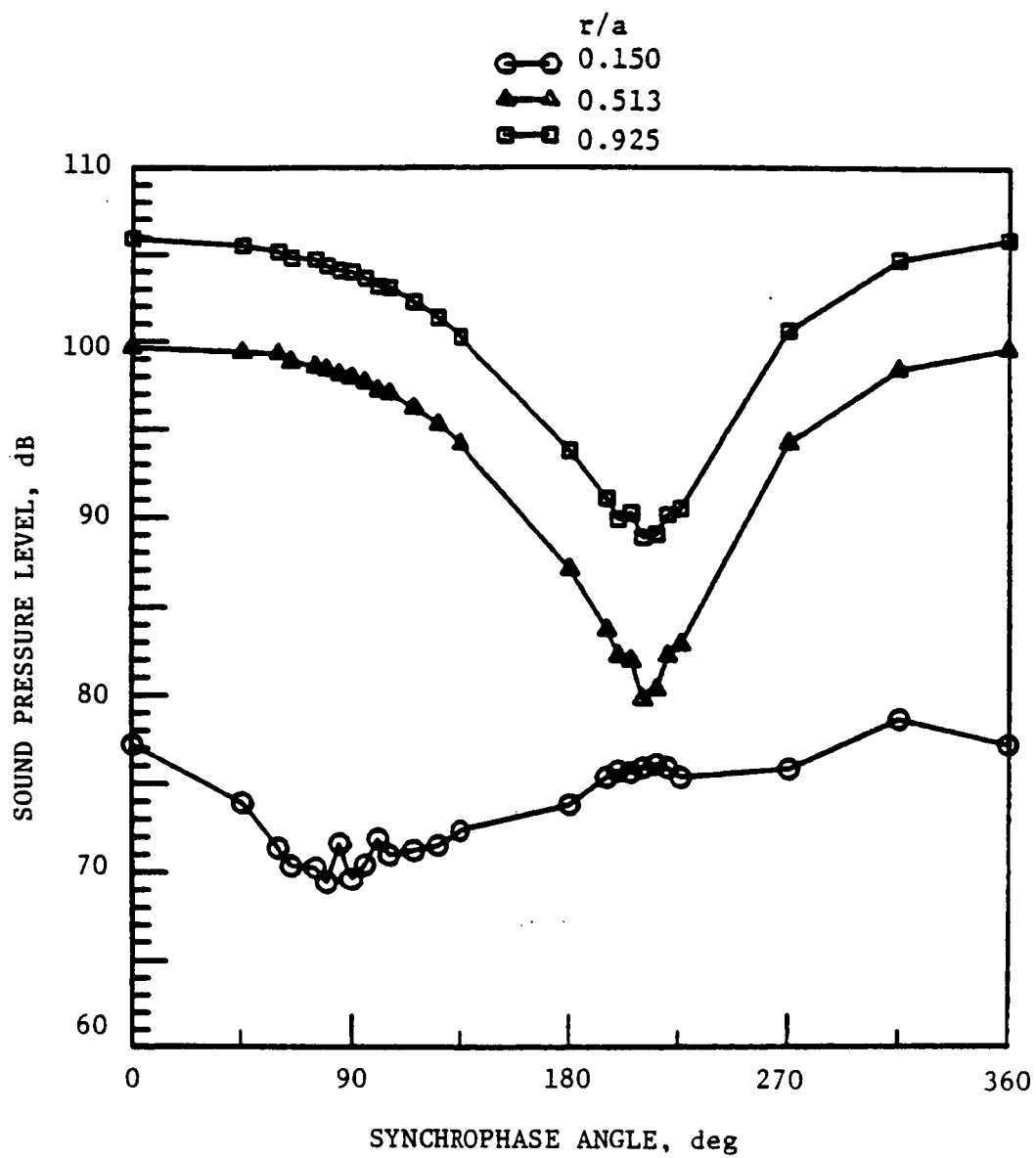


Fig. 18. Interior Pressure Measurements at $x/a = 1.6$, $\theta = 0^\circ$, and $f = 680$ Hz.

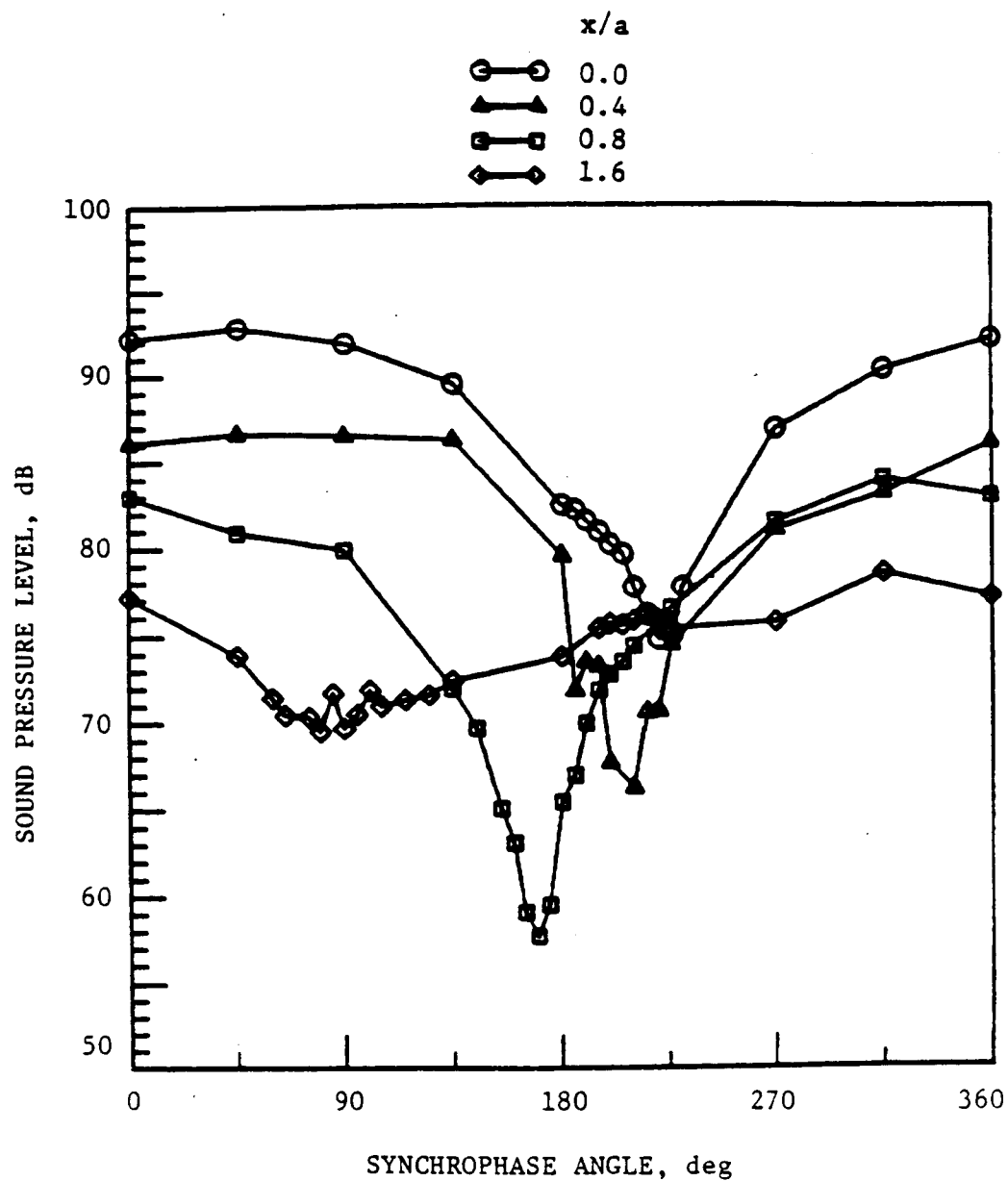


Fig. 19. Interior Pressure Measurements at $r/a = 0.150$, $\theta = 0^\circ$, and $f = 680$ Hz.

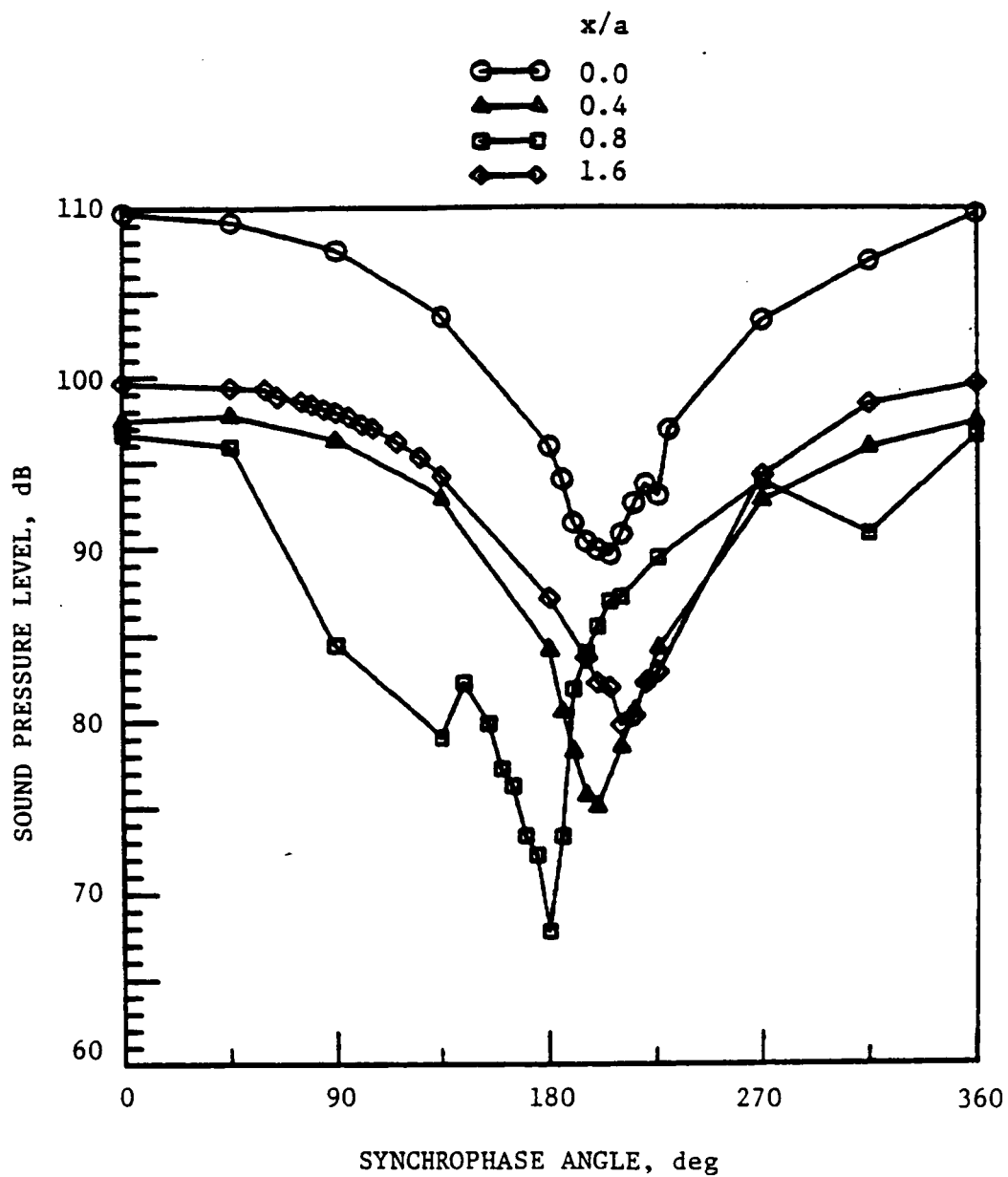


Fig. 20. Interior Pressure Measurements at $r/a = 0.513$, $\theta = 0^\circ$, and $f = 680$ Hz.

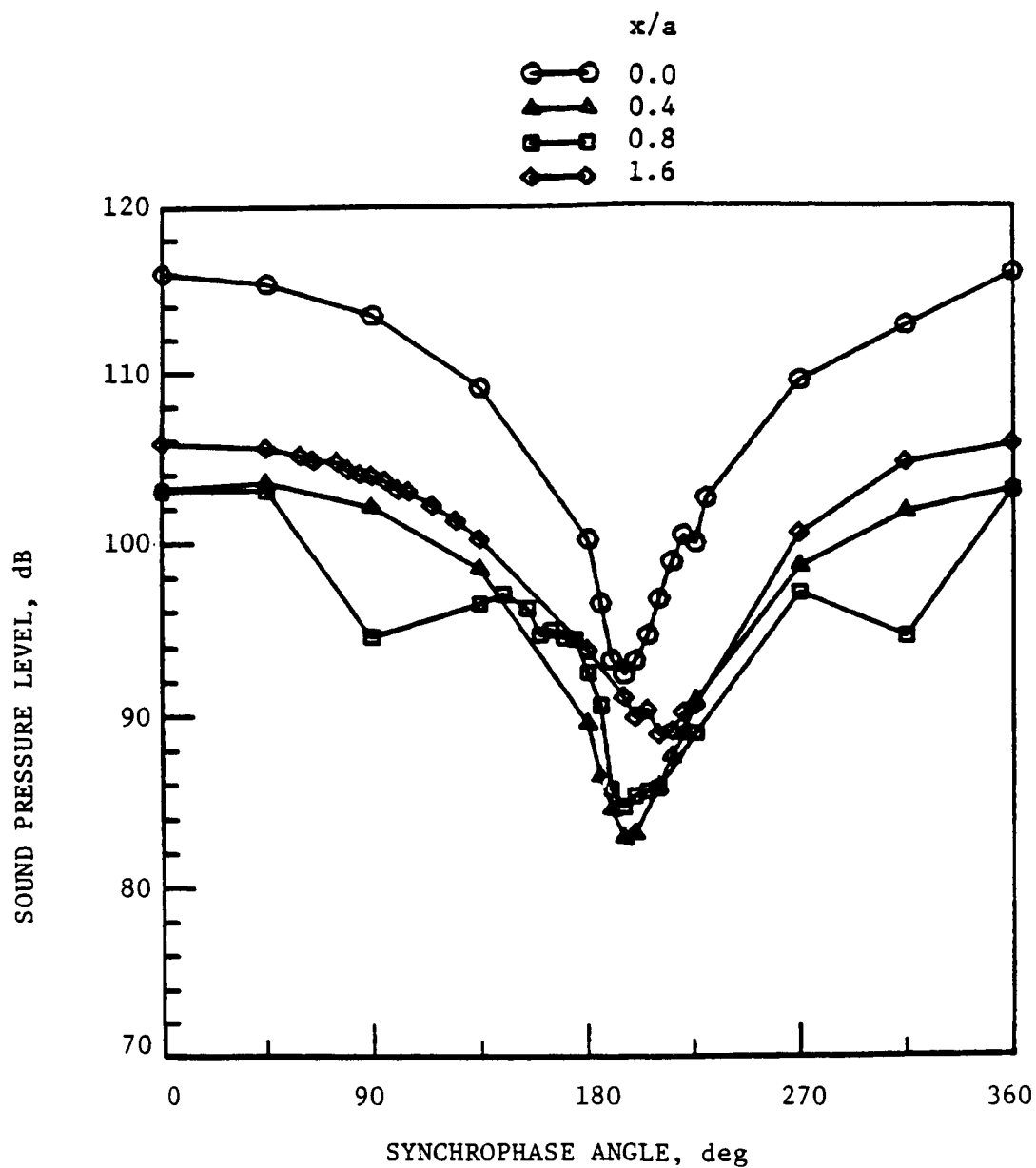
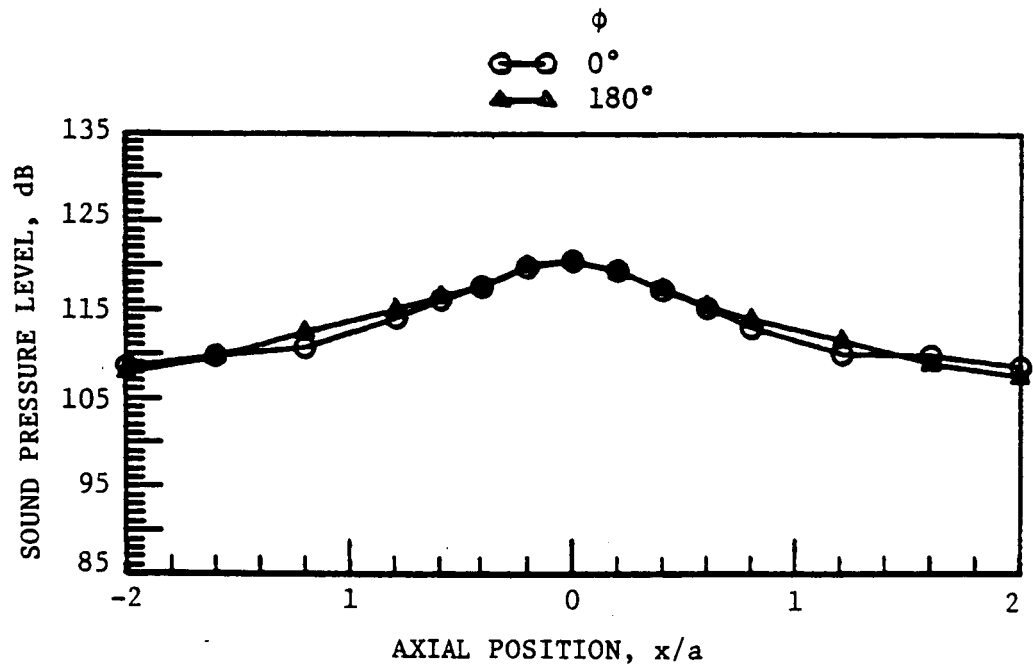
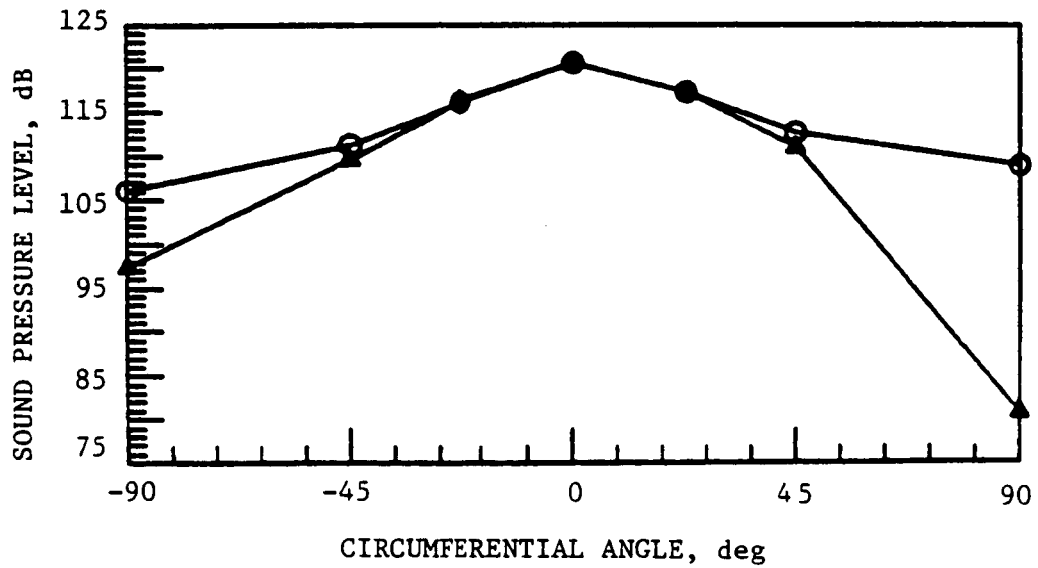


Fig. 21. Interior Pressure Measurements at $r/a = 0.925$, $\theta = 0^\circ$, and $f = 680$ Hz.



(a) Axial Pressure Distribution at $\theta = 0^\circ$



(b) Circumferential Pressure Distribution at $x/a = 0.0$

Fig. 22. Exterior Pressure Measurements on Cylinder for $f = 708$ Hz.

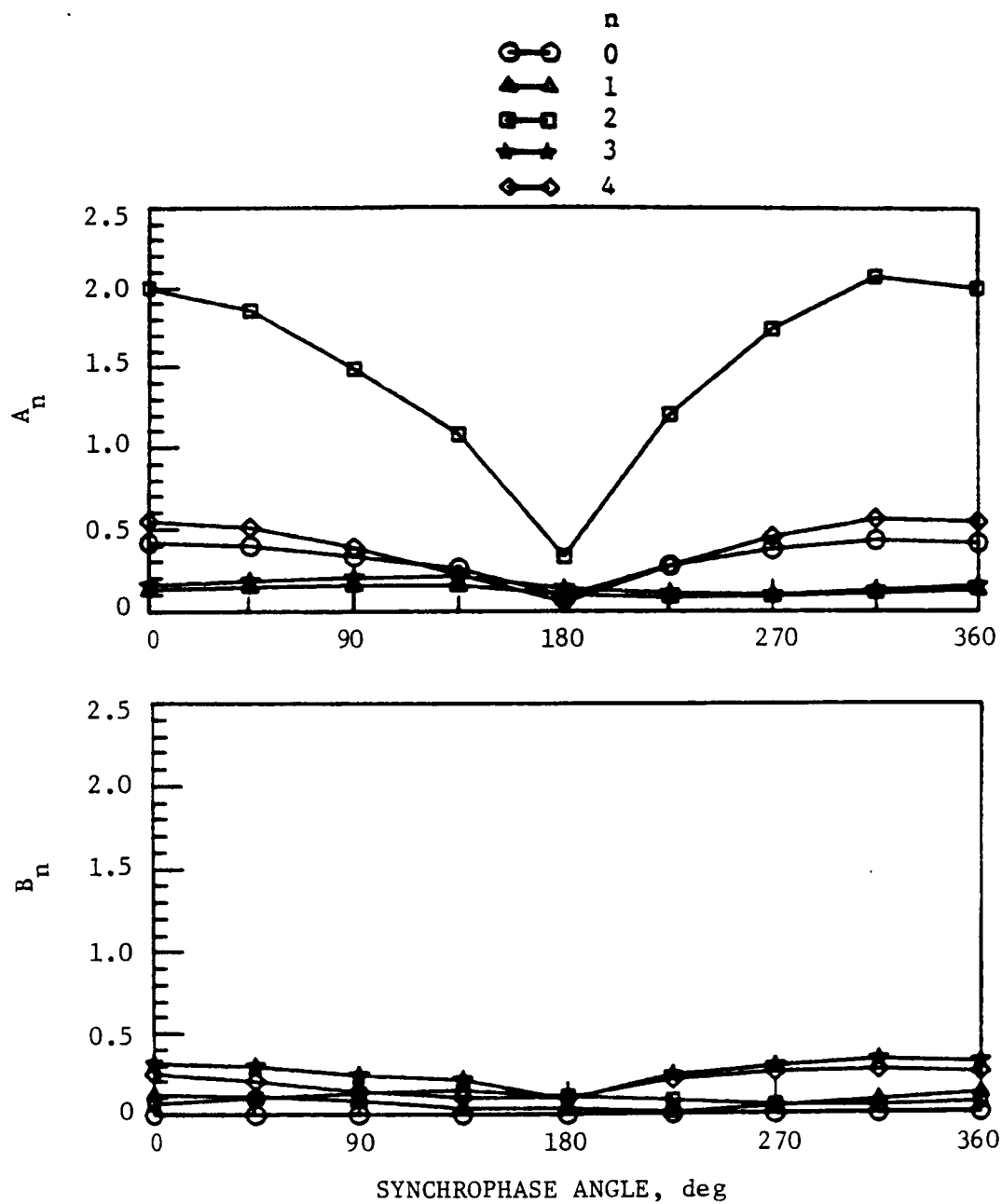


Fig. 23. Relative Modal Amplitudes of the Cylinder at $x/a = 0.0$ and $f = 708$ Hz.

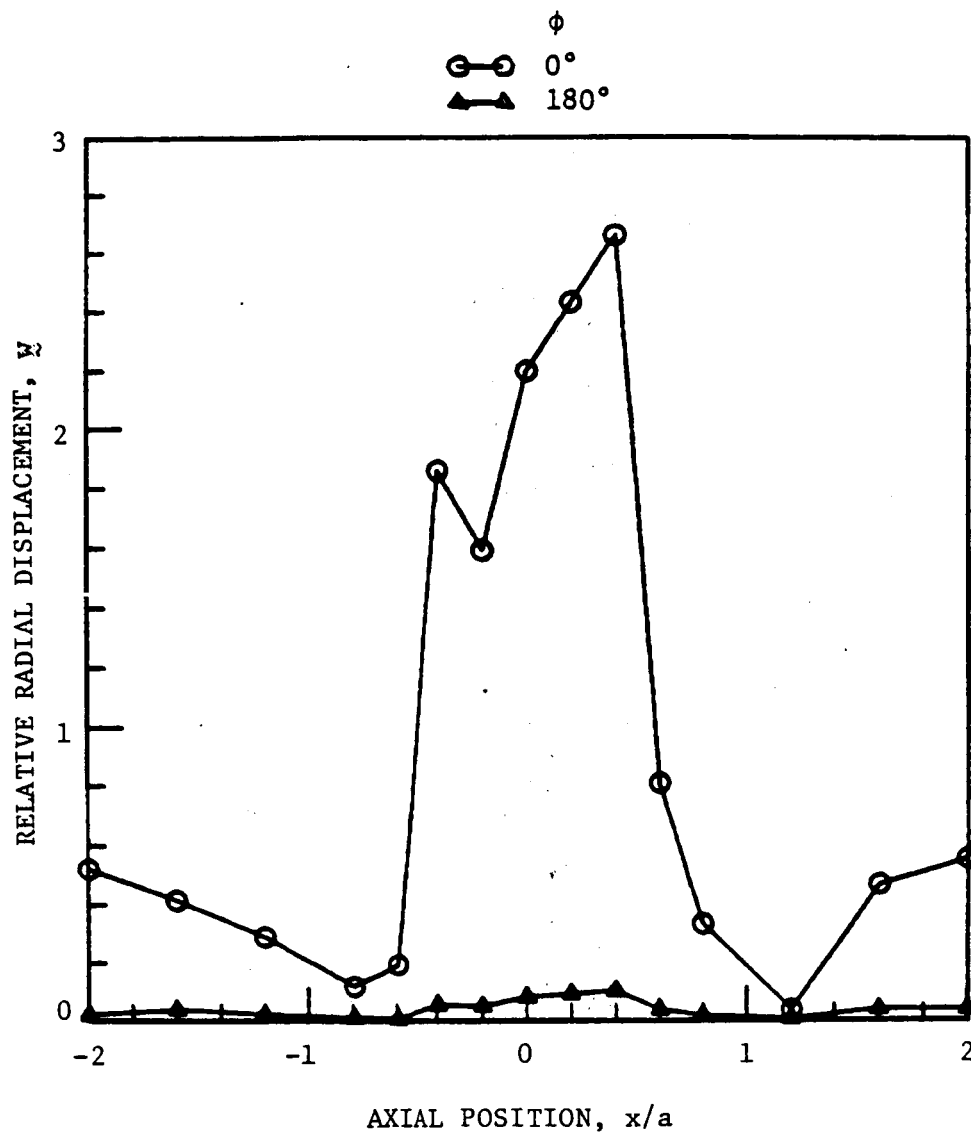


Fig. 24. Axial Distribution of the Radial Displacement of the Cylinder at $\theta = 0^\circ$ and $f = 708$ Hz.

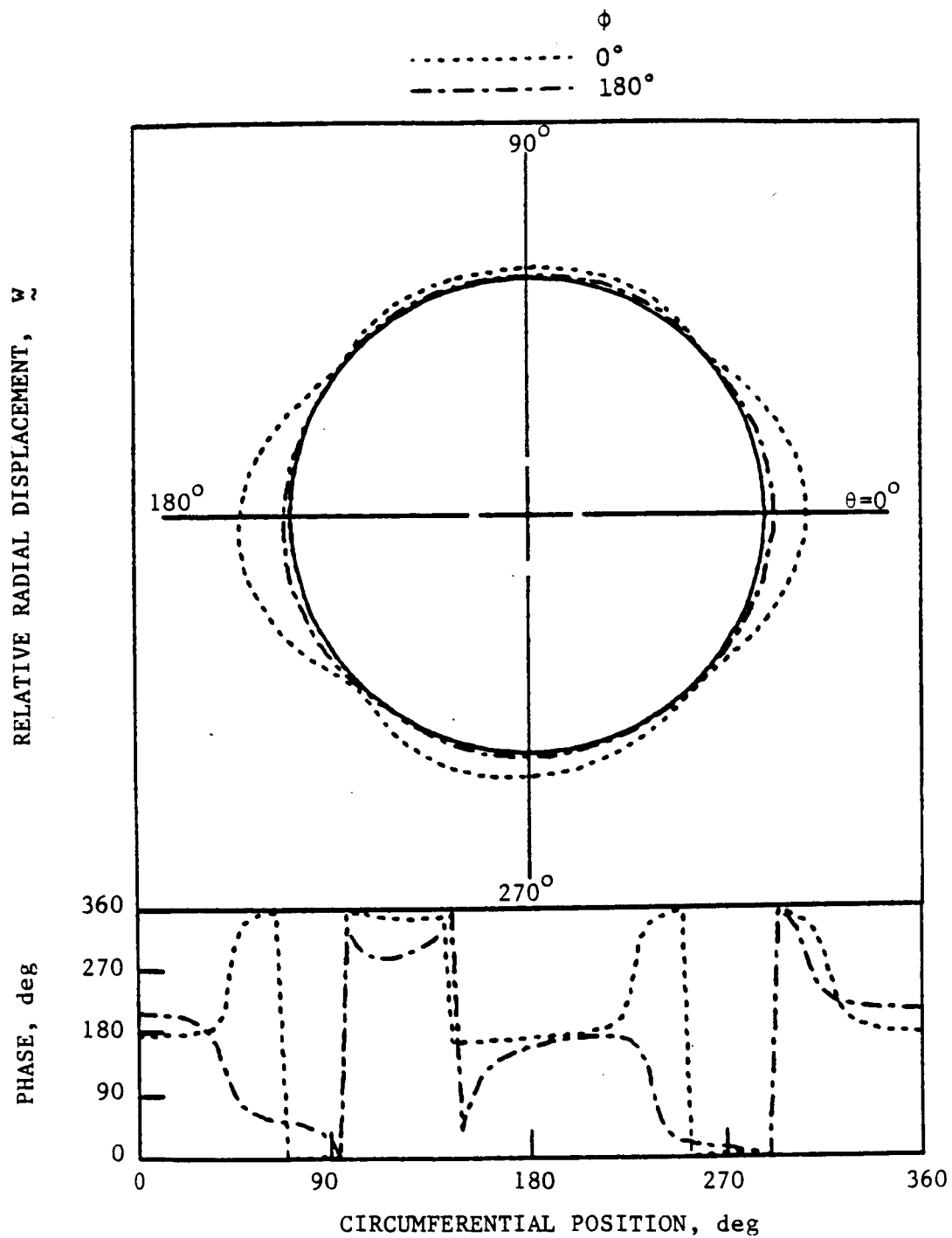


Fig. 25. Relative Radial Displacement and Phase of the Cylinder at $x/a = 0.0$ and $f = 708$ Hz.

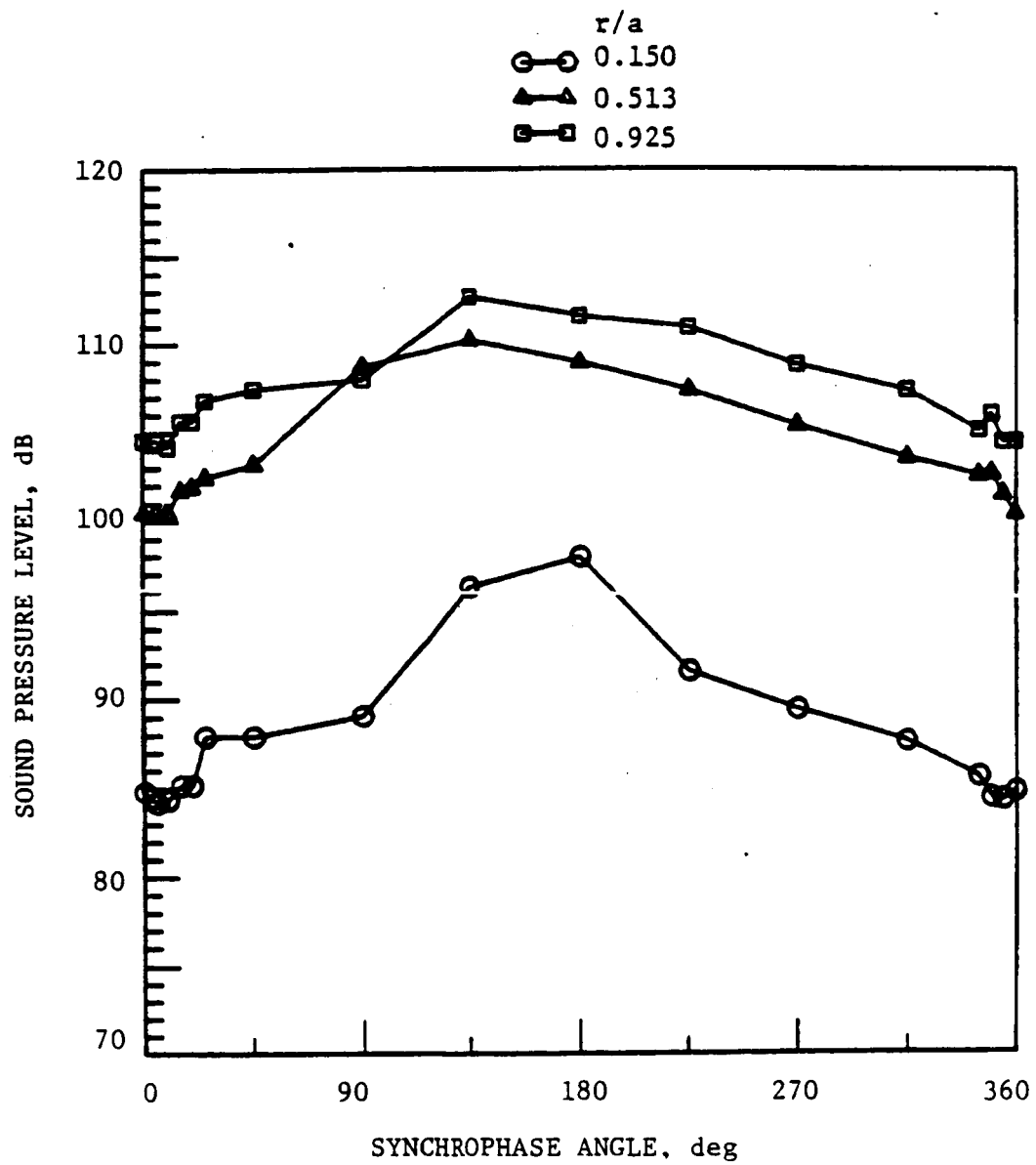


Fig. 26. Interior Pressure Measurements at $x/a = 0.0$, $\theta = 0^\circ$, and $f = 708$ Hz.

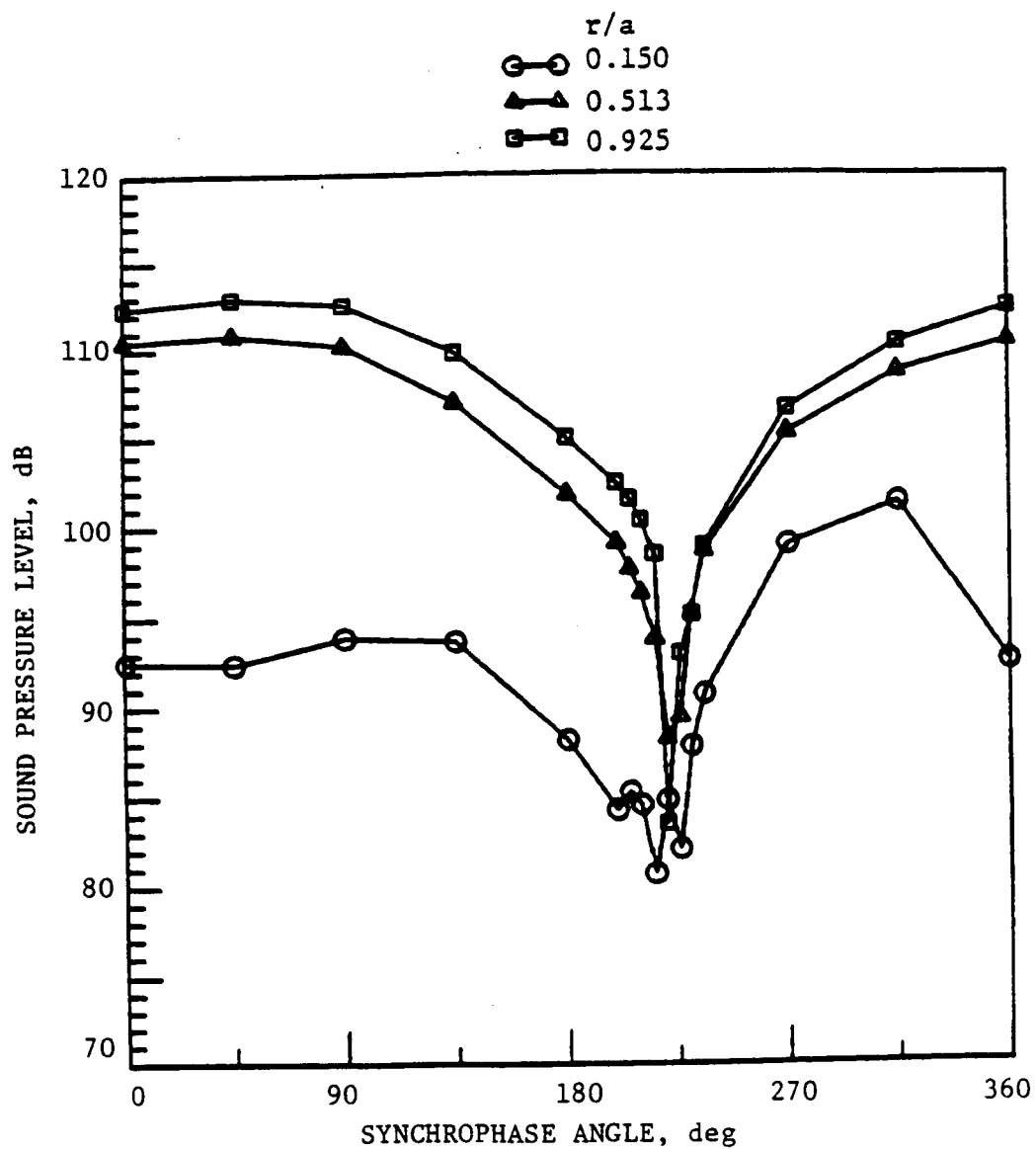


Fig. 27. Interior Pressure Measurements at $x/a = 0.0$, $\theta = 45^\circ$, and $f = 708$ Hz.

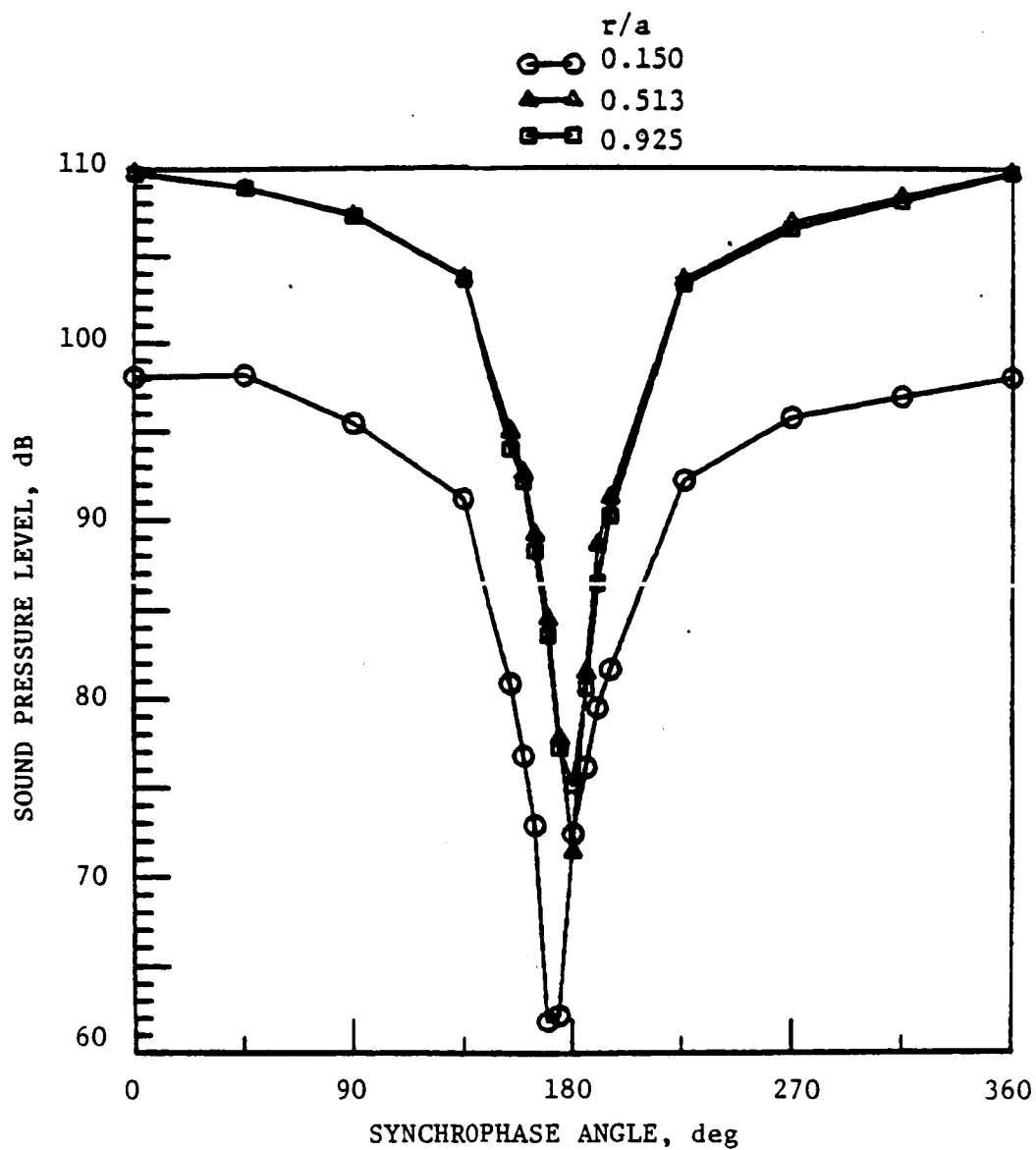


Fig. 28. Interior Pressure Measurements at $x/a = 0.0$, $\theta = 90^\circ$, and $f = 708$ Hz.

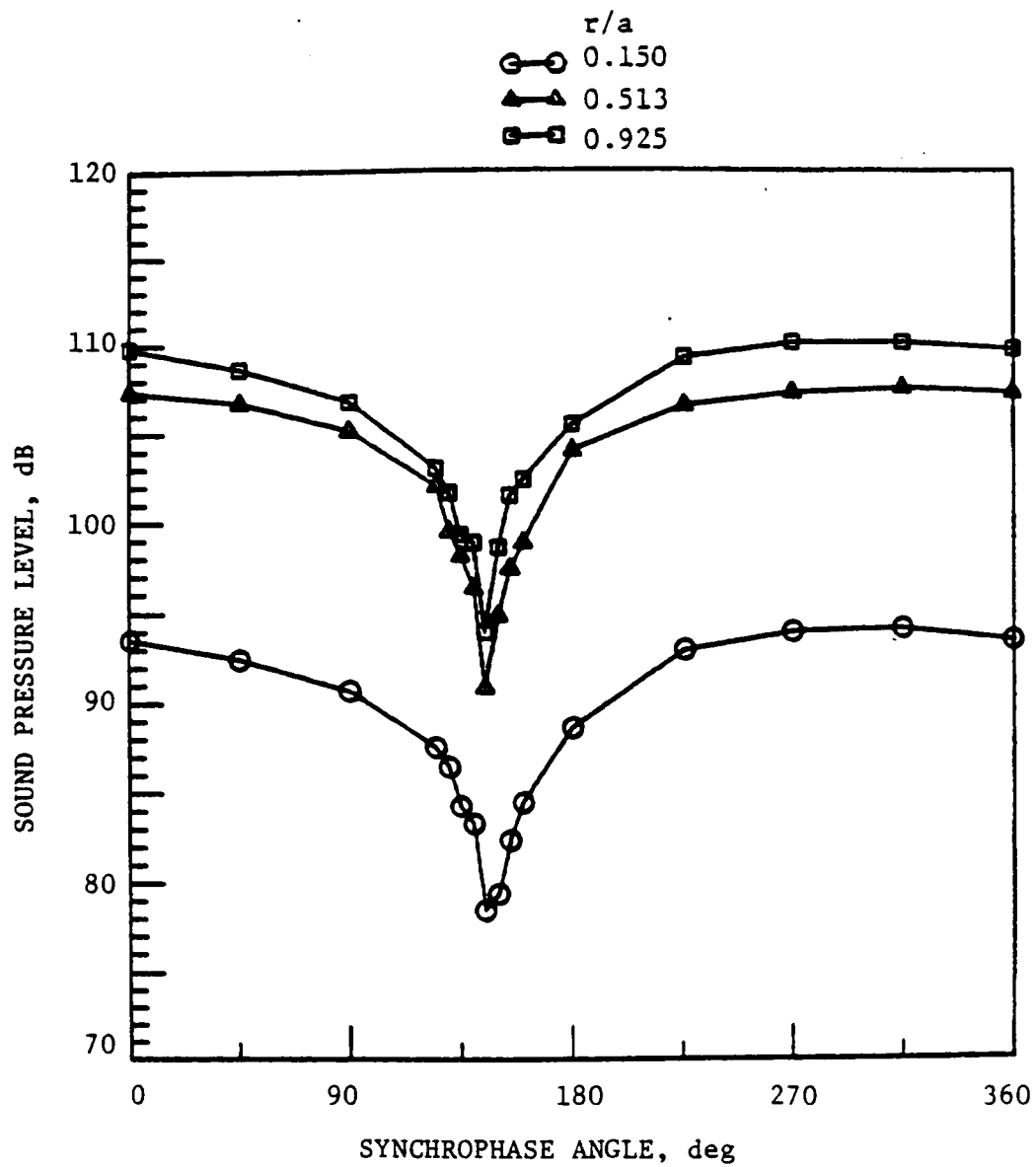


Fig. 29. Interior Pressure Measurements at $x/a = 0.0$, $\theta = 135^\circ$, and $f = 708$ Hz.

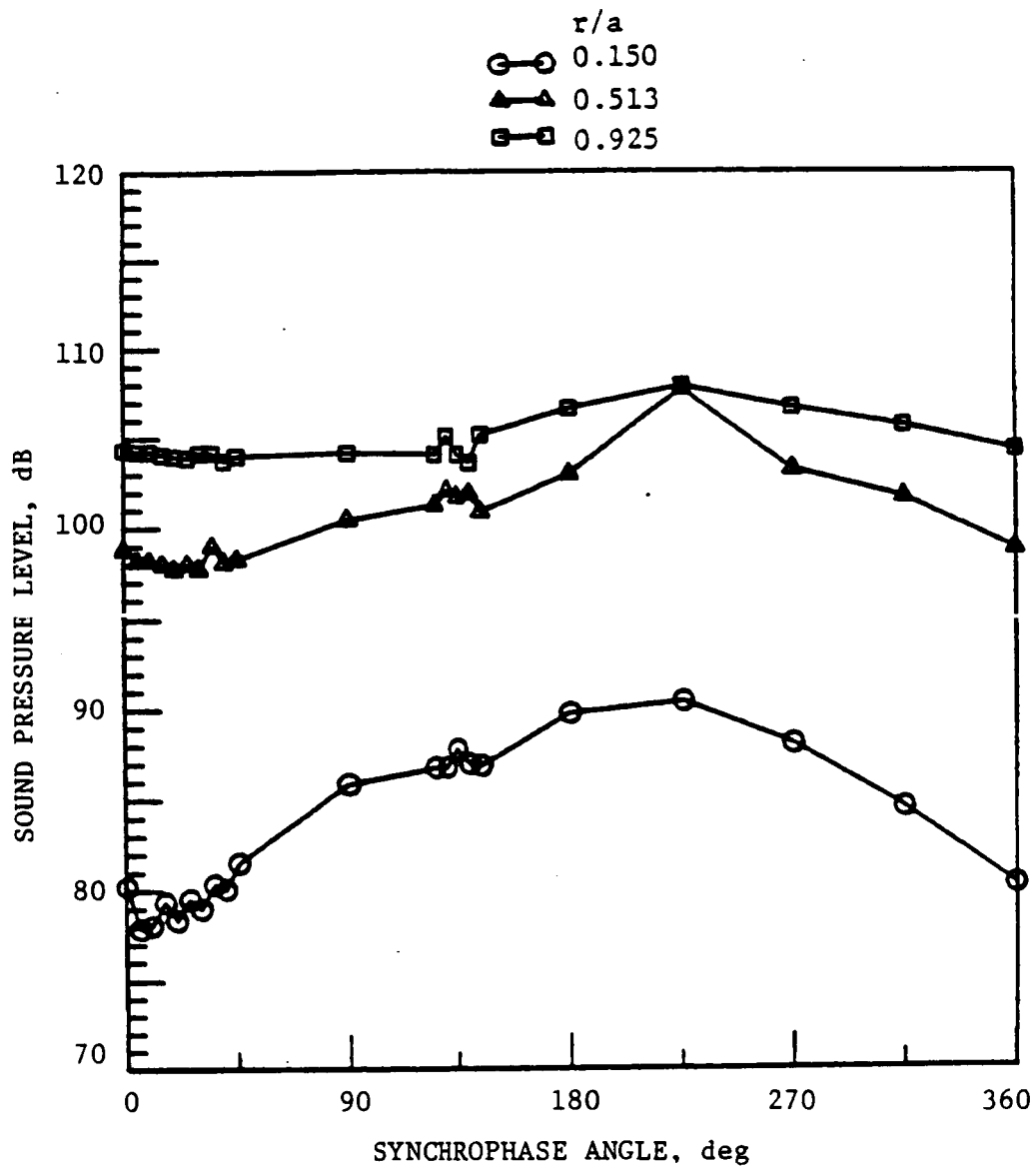


Fig. 30. Interior Pressure Measurements at $x/a = 0.0$, $\theta = 180^\circ$, and $f = 708$ Hz.

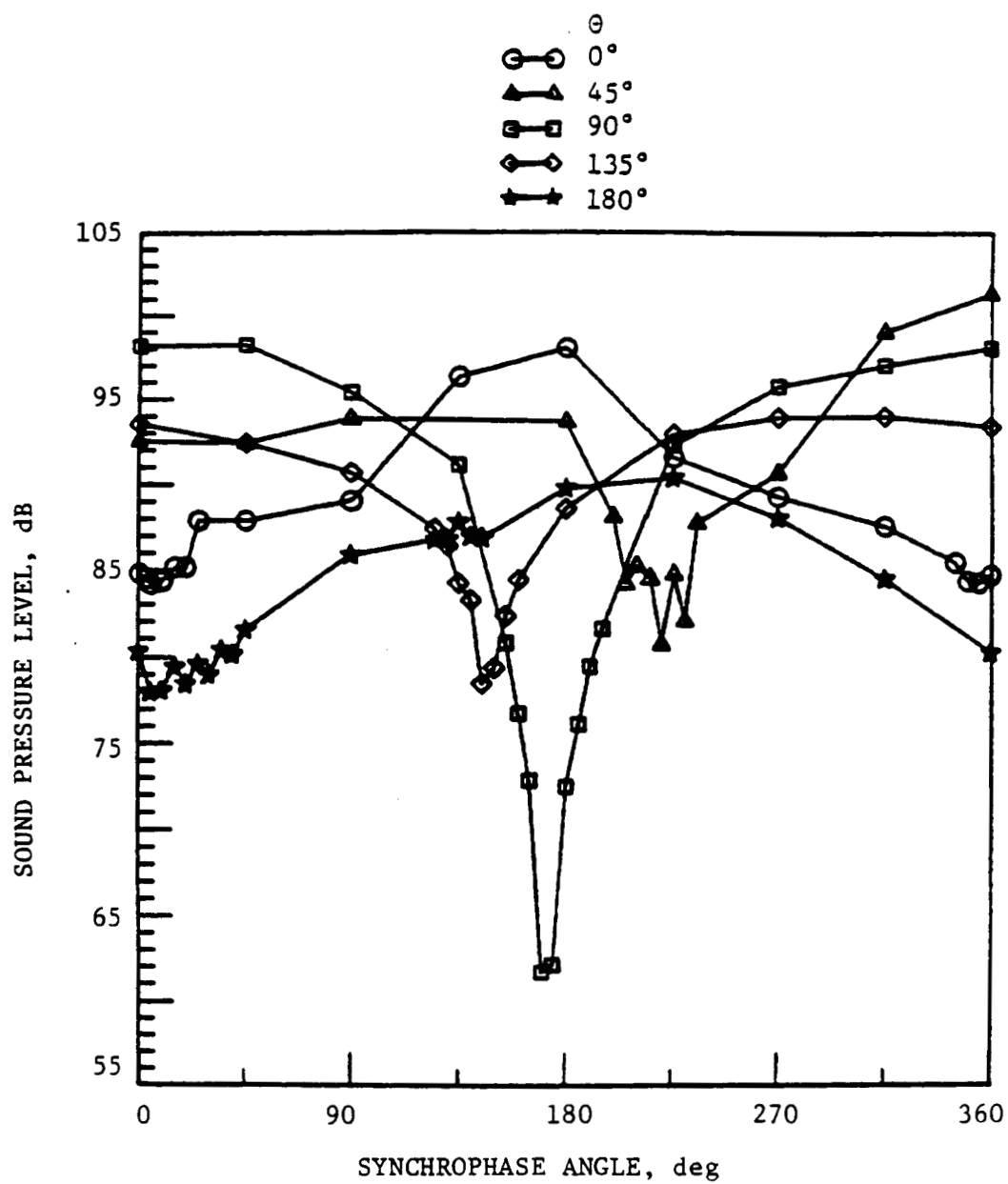


Fig. 31. Interior Pressure Measurements at $x/a = 0.0$, $r/a = 0.150$, and $f = 708$ Hz.

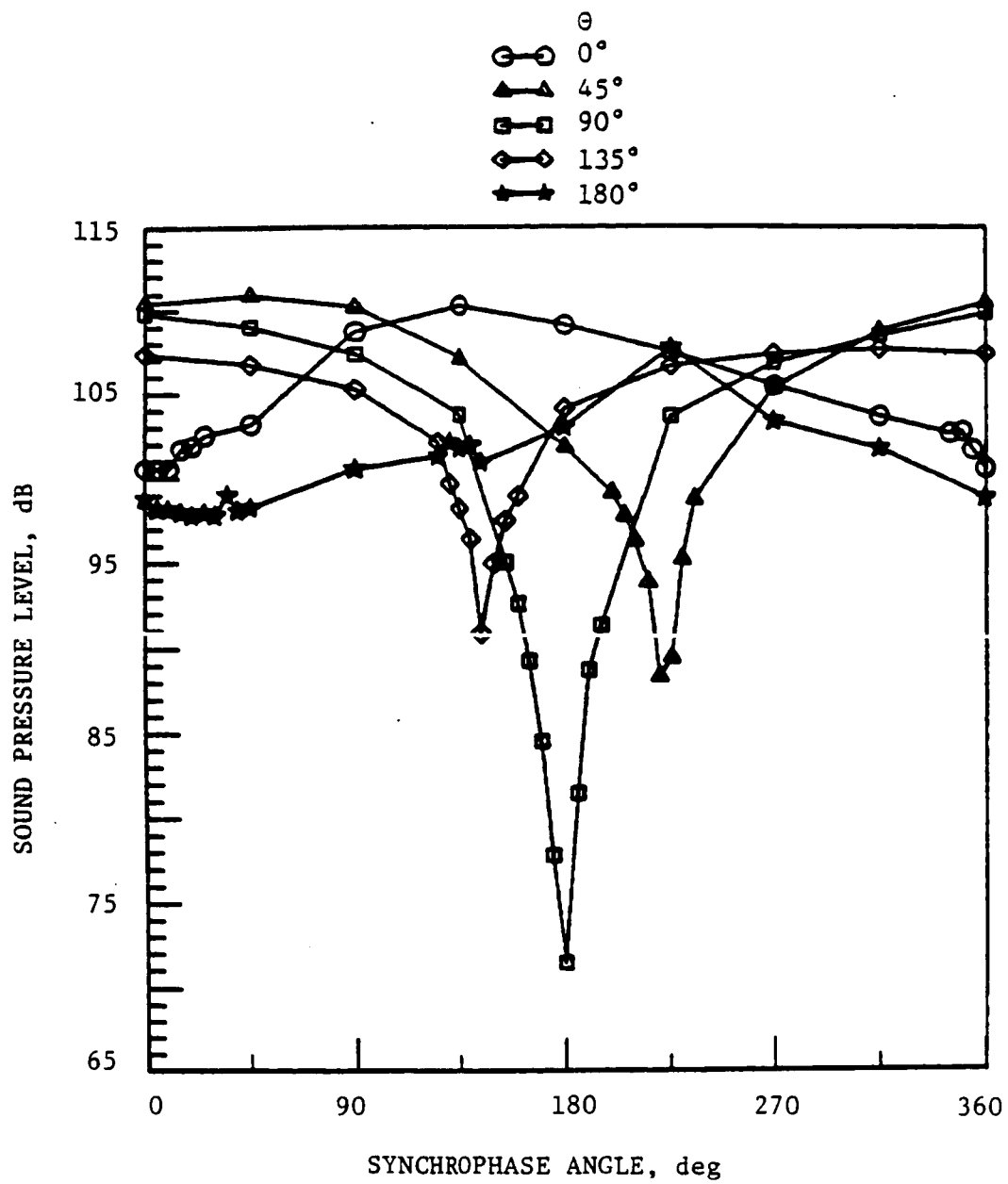


Fig. 32. Interior Pressure Measurement at $x/a = 0.0$, $r/a = 0.513$, and $f = 708$ Hz.

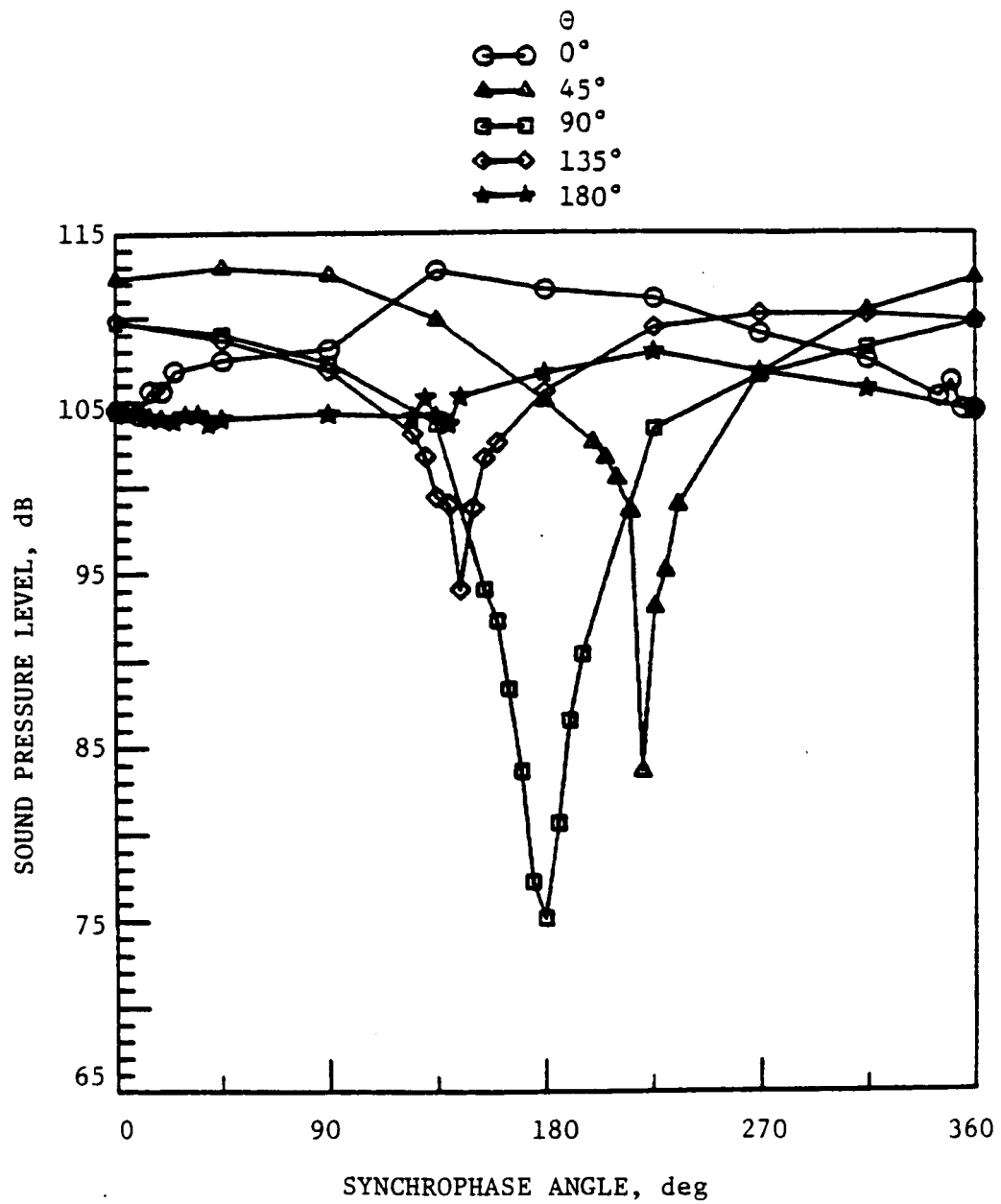


Fig. 33. Interior Pressure Measurements at $x/a = 0.0$, $r/a = 0.925$, and $f = 708$ Hz.

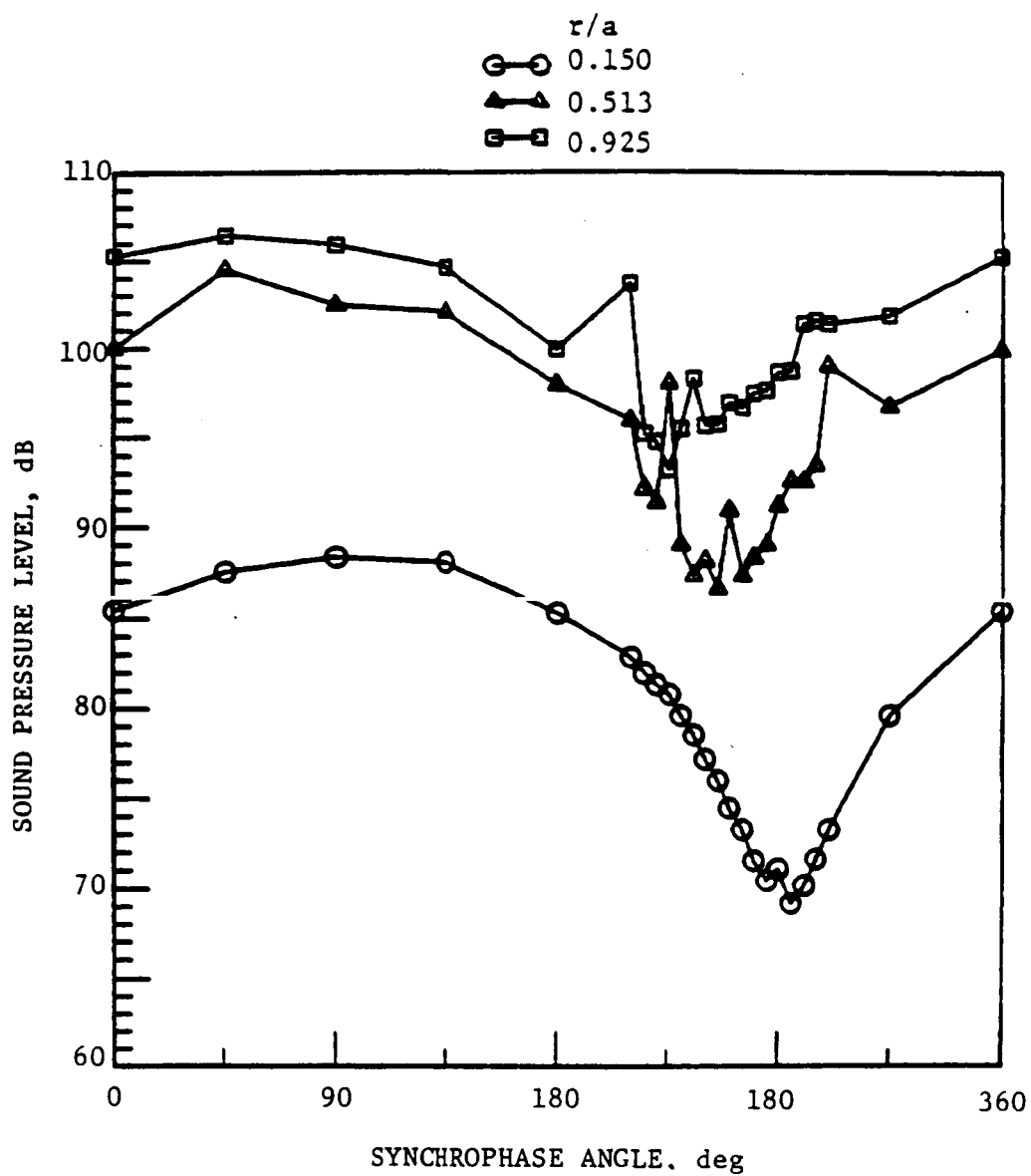


Fig. 34. Interior Pressure Measurements at $x/a = 0.4$, $\theta = 0^\circ$, and $f = 708$ Hz.

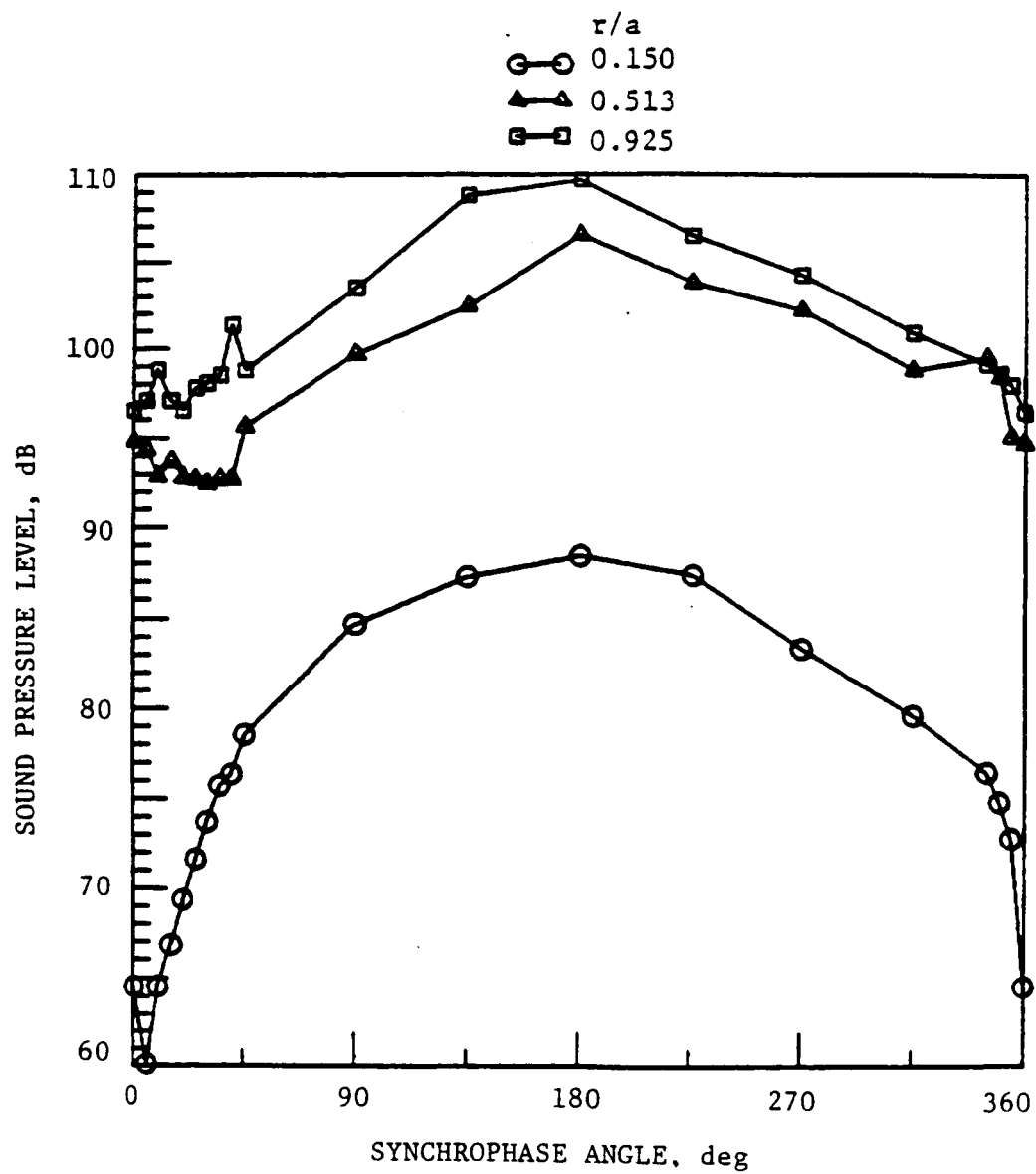


Fig. 35. Interior Pressure Measurements at $x/a = 0.8$, $\theta = 0^\circ$, and $f = 708$ Hz.

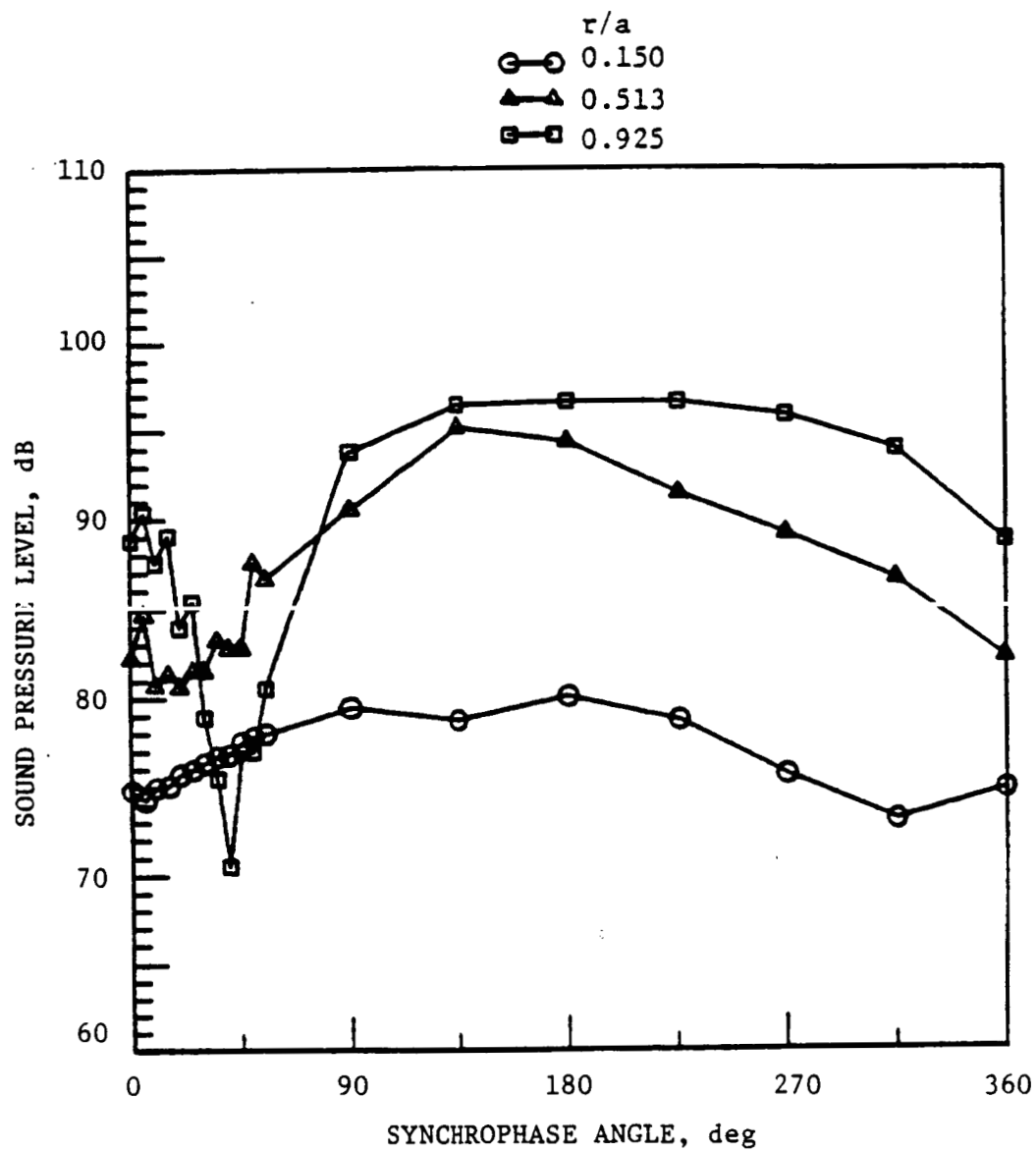


Fig. 36. Interior Pressure Measurements at $x/a = 1.6$, $\theta = 0^\circ$, and $f = 708$ Hz.

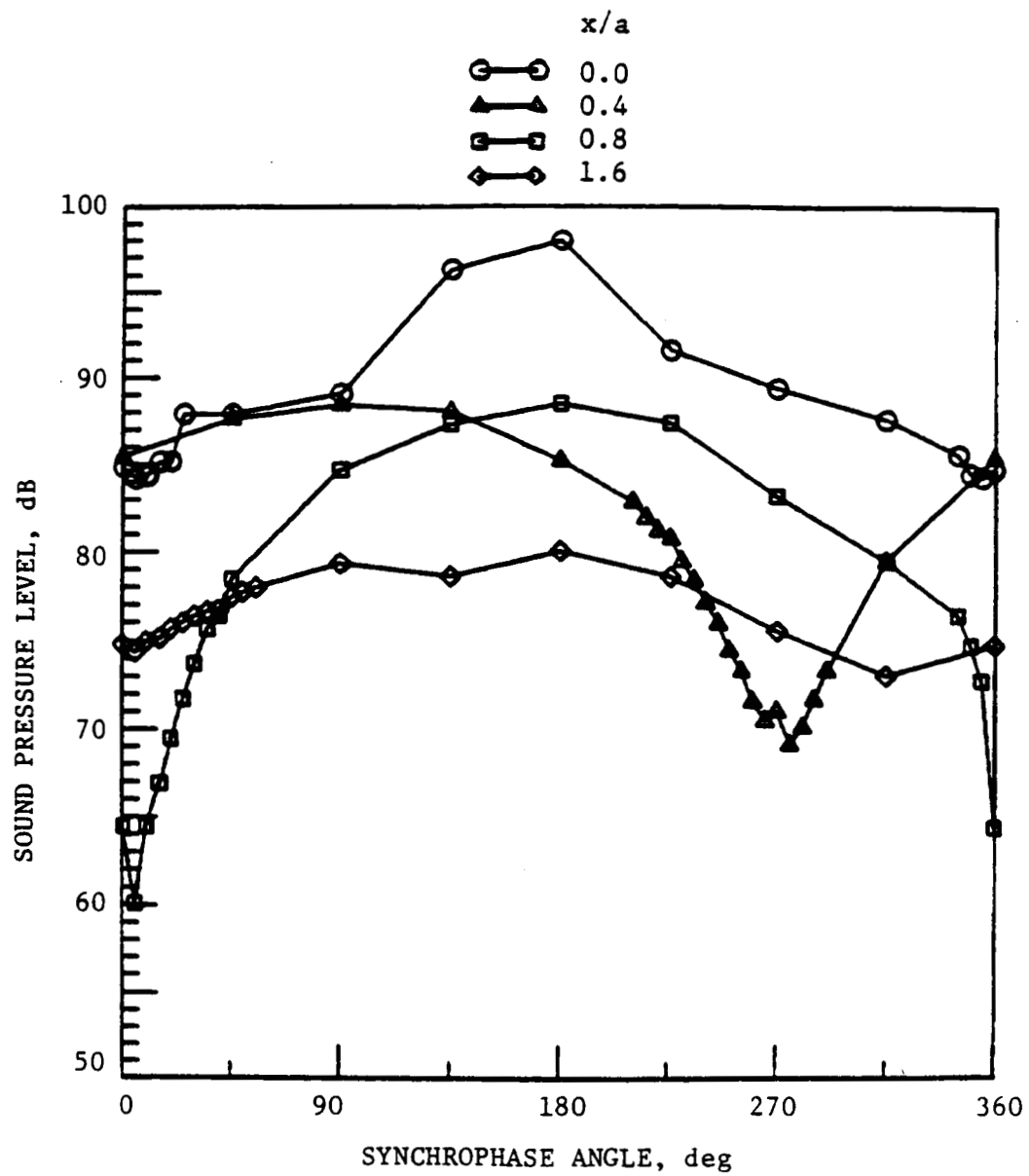


Fig. 37. Interior Pressure Measurements at $r/a = 0.150$, $\theta = 0^\circ$, and $f = 708$ Hz.

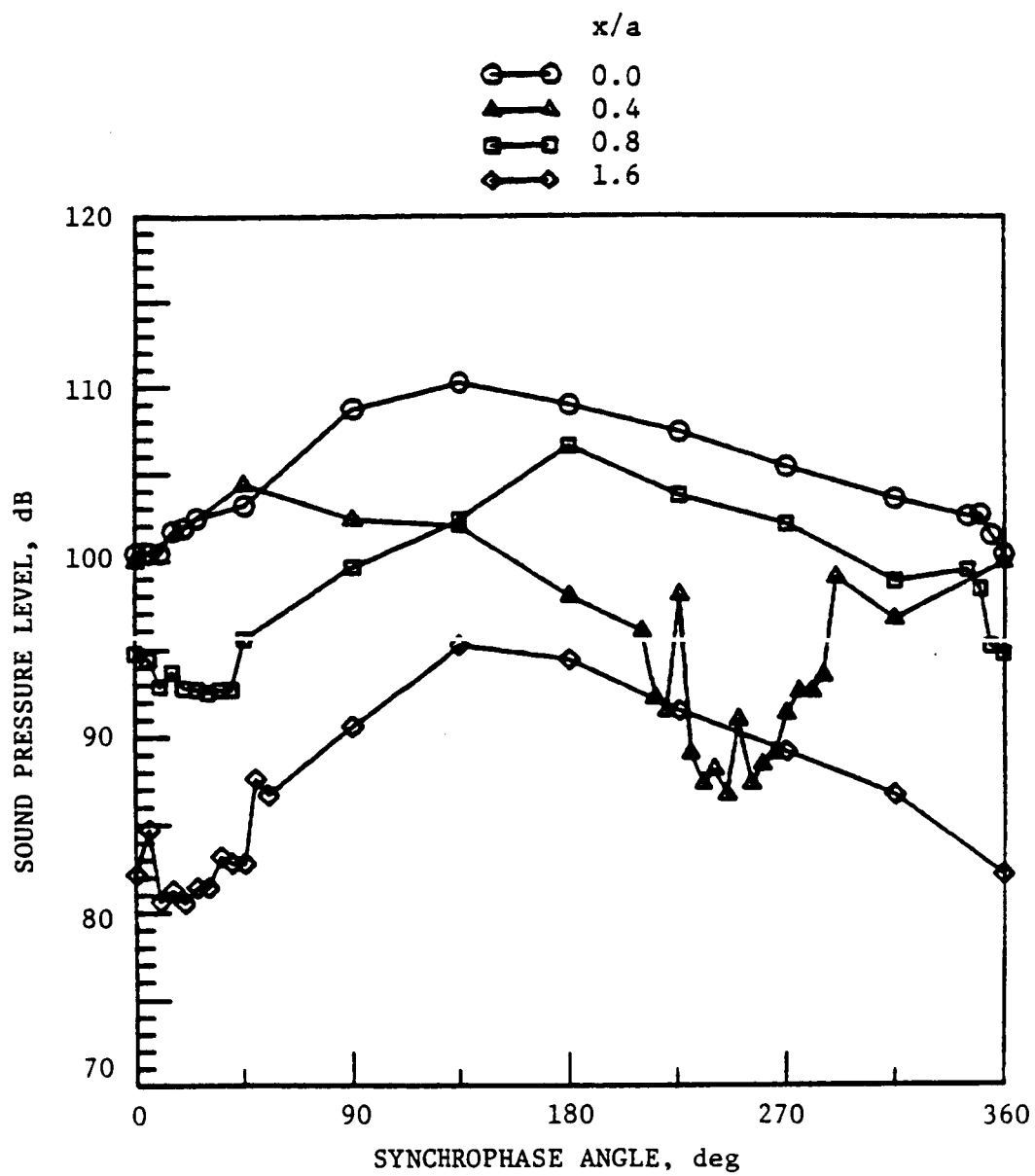


Fig. 38. Interior Pressure Measurements at $r/a = 0.513$, $\theta = 0^\circ$, and $f = 708$ Hz.

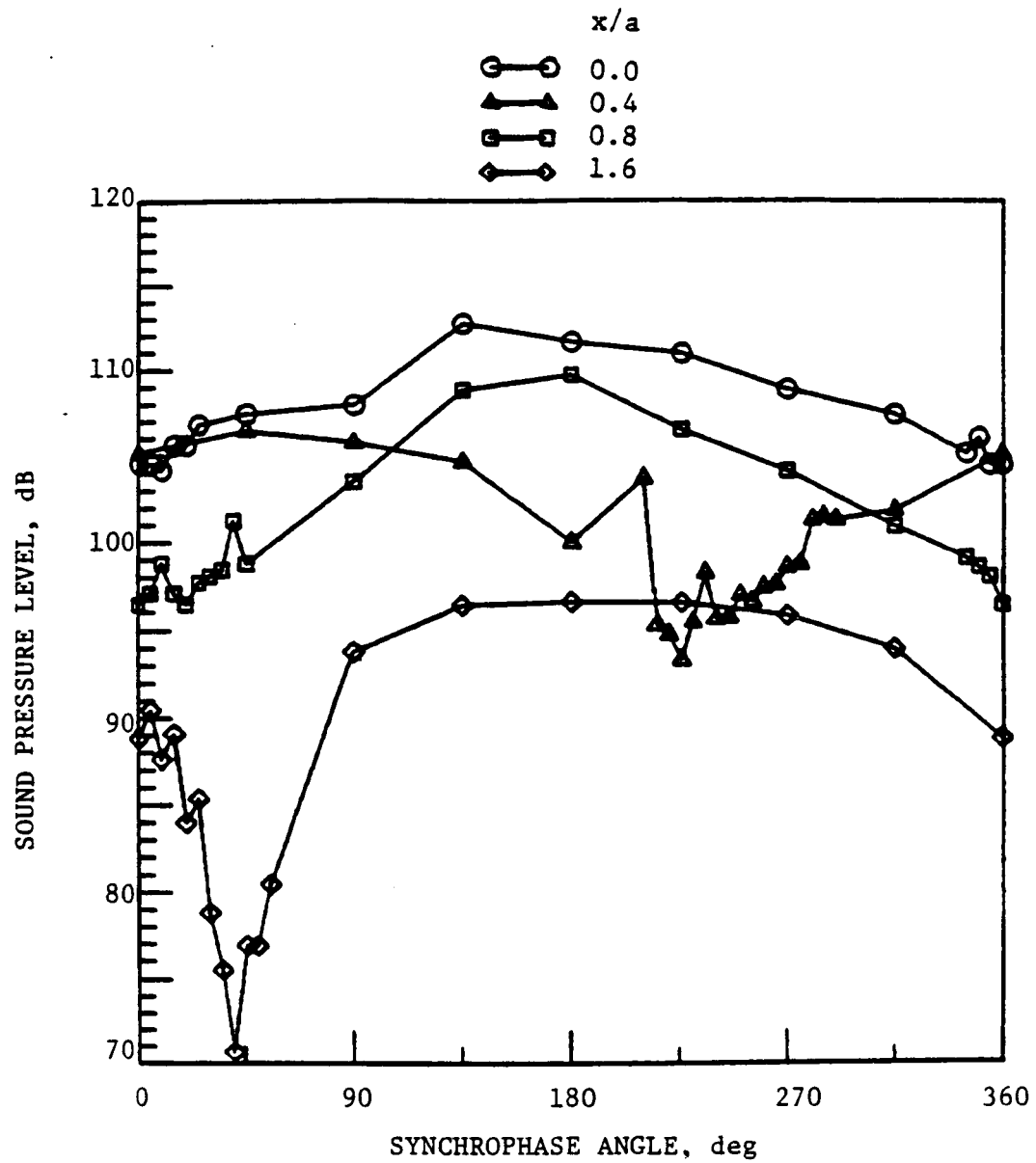


Fig. 39. Interior Pressure Measurements at $r/a = 0.925$, $\theta = 0^\circ$, and $f = 708$ Hz.

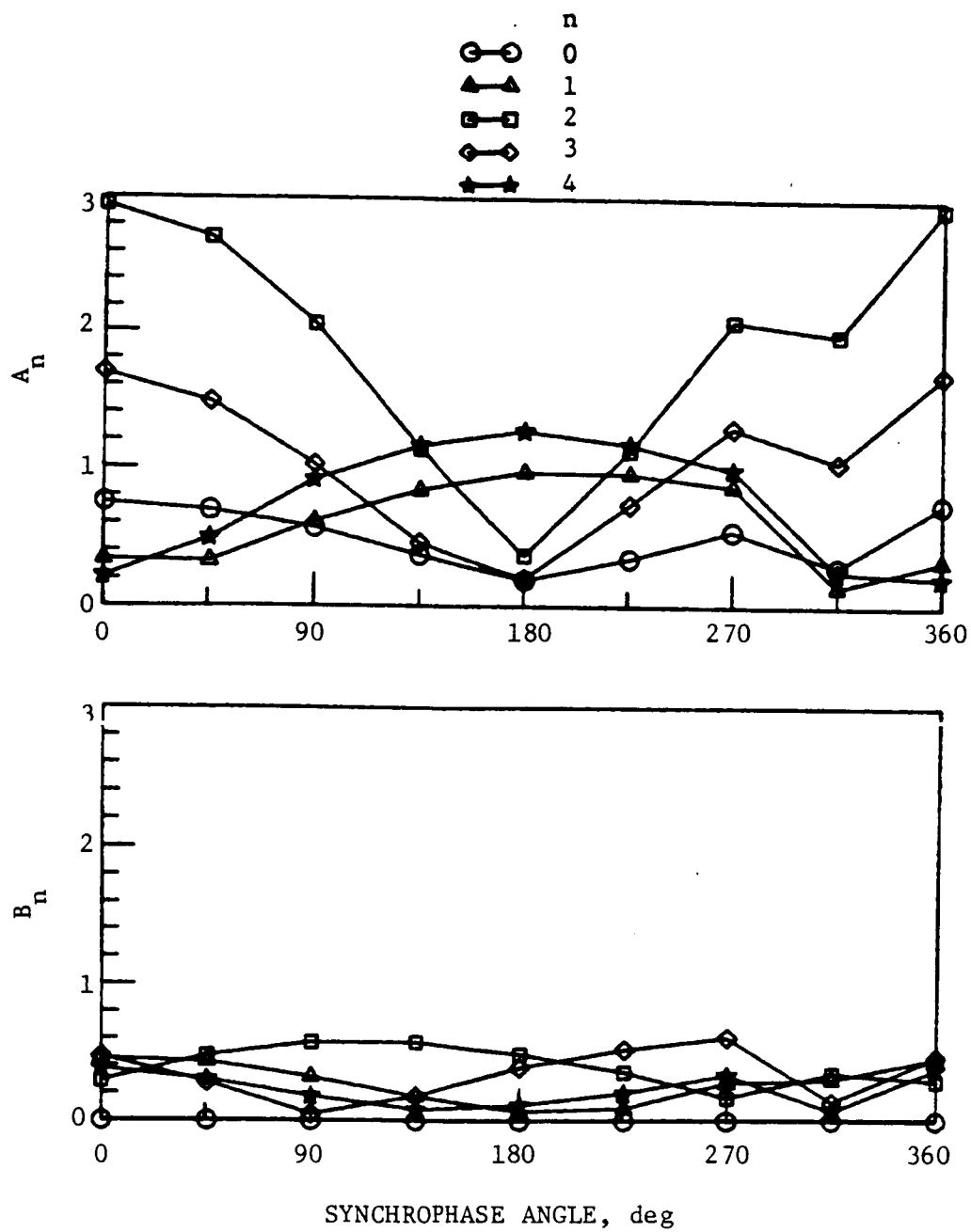


Fig. 40. Relative Modal Amplitudes of the Cylinder at $x/a = 0.0$ and $f = 708$ Hz with Internal Acoustic Damping.

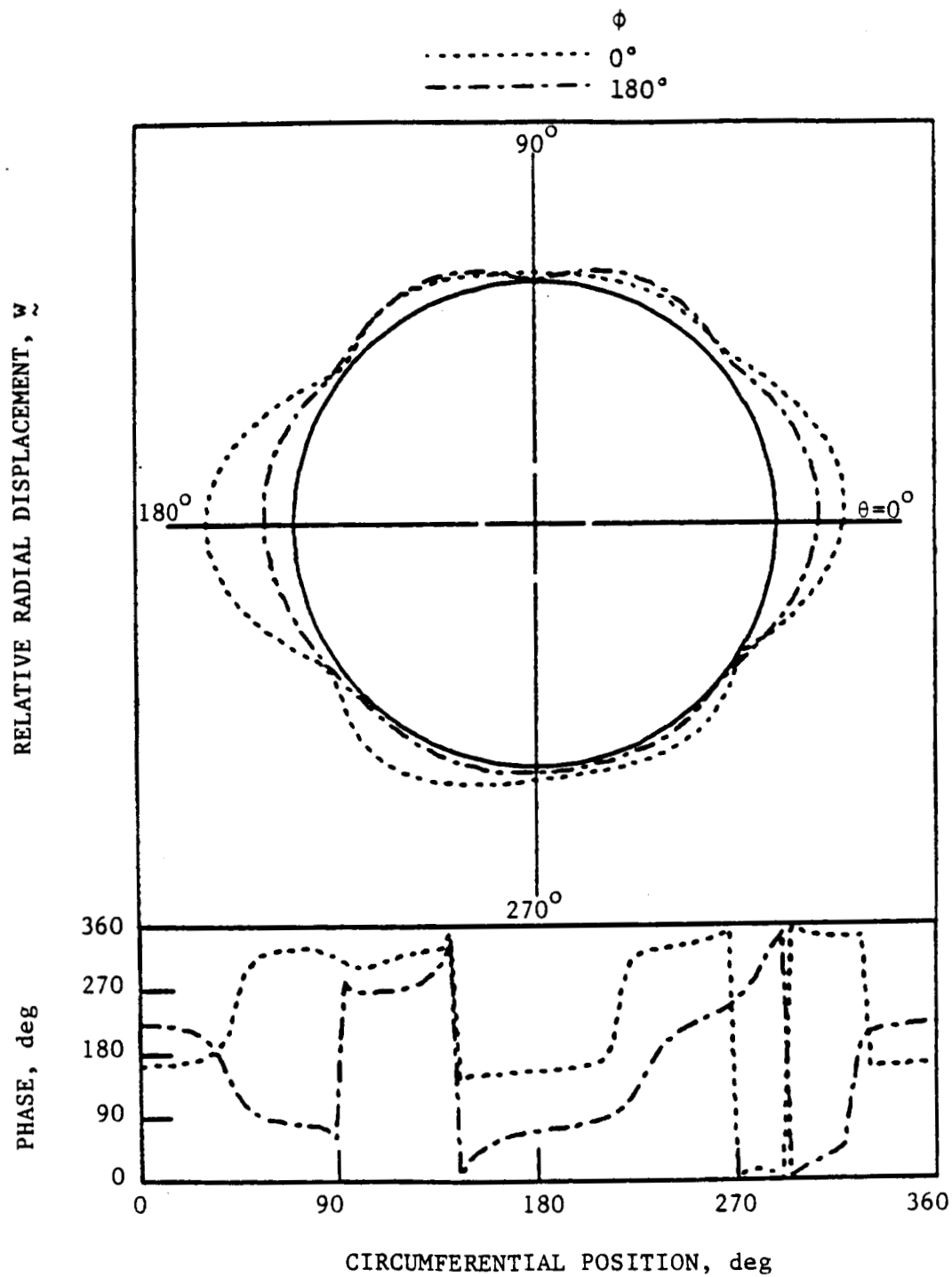


Fig. 41. Relative Radial Displacement and Phase of the Cylinder at $x/a = 0.0$ and $f = 708$ Hz with Internal Acoustic Damping.

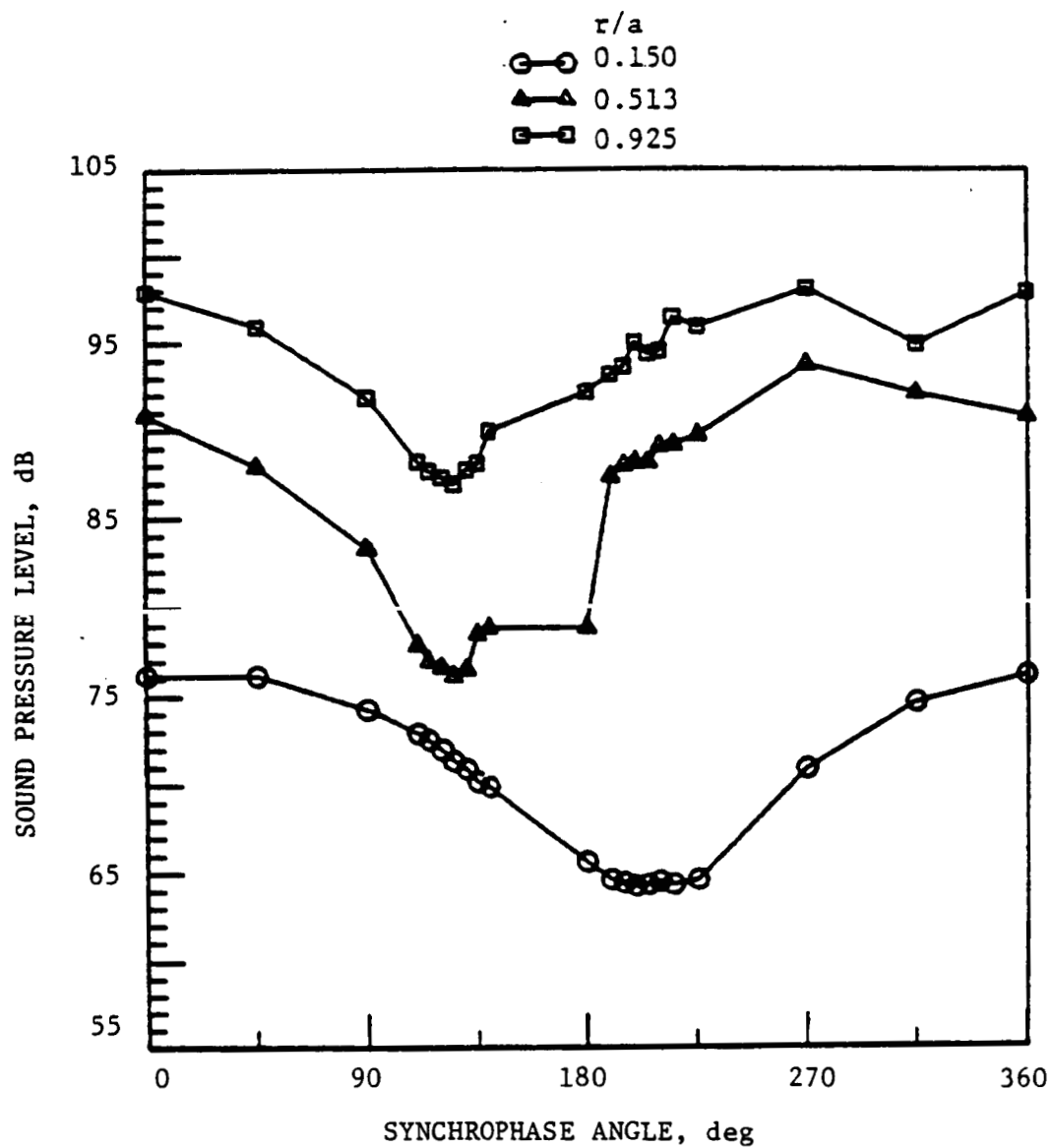


Fig. 42. Interior Pressure Measurements at $x/a = 0.0$, $\theta = 0^\circ$, and $f = 708$ Hz with Internal Acoustic Damping.

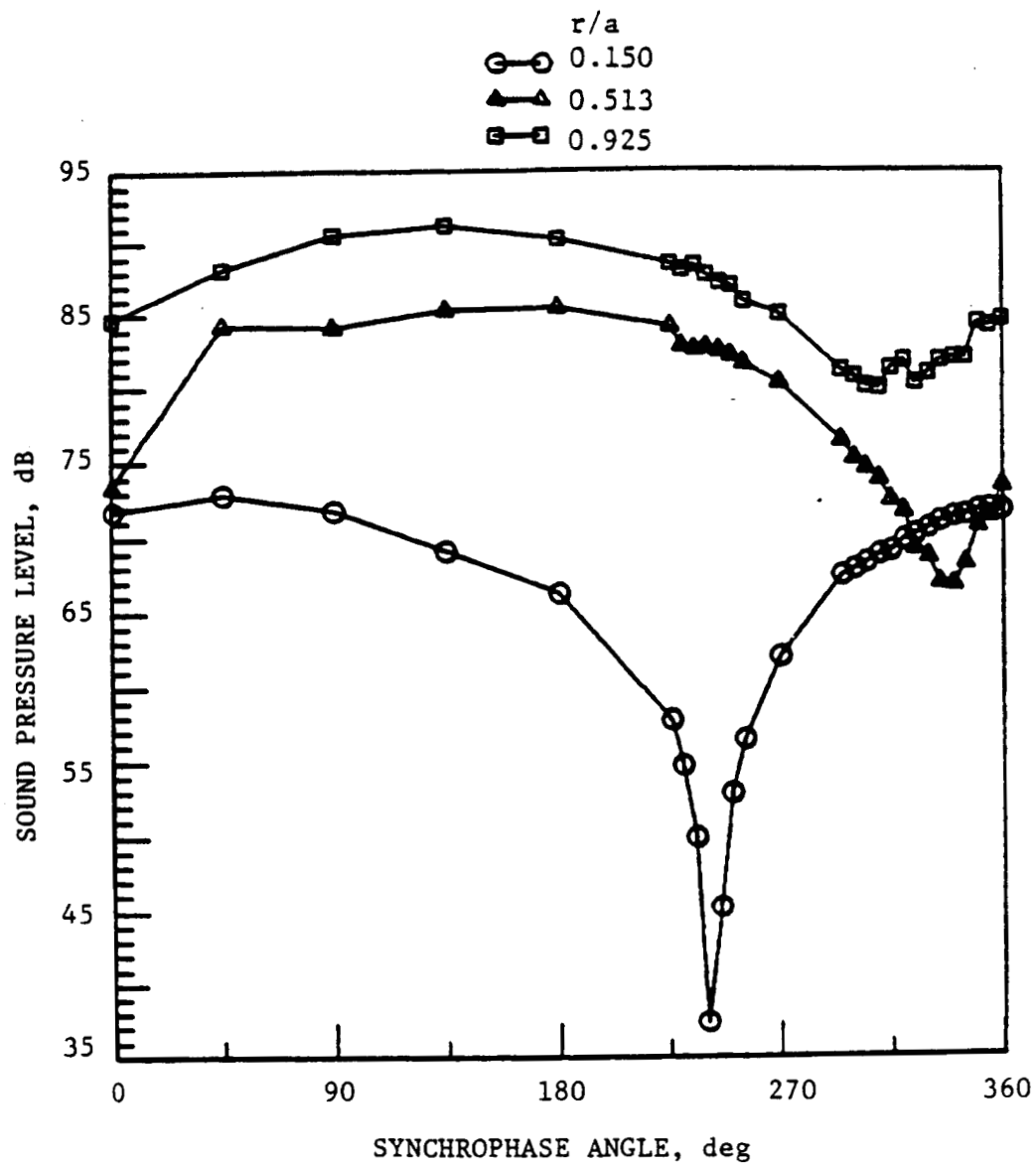


Fig. 43. Interior Pressure Measurements at $x/a = 0.0$, $\theta = 45^\circ$, and $f = 708$ Hz with Internal Acoustic Damping.

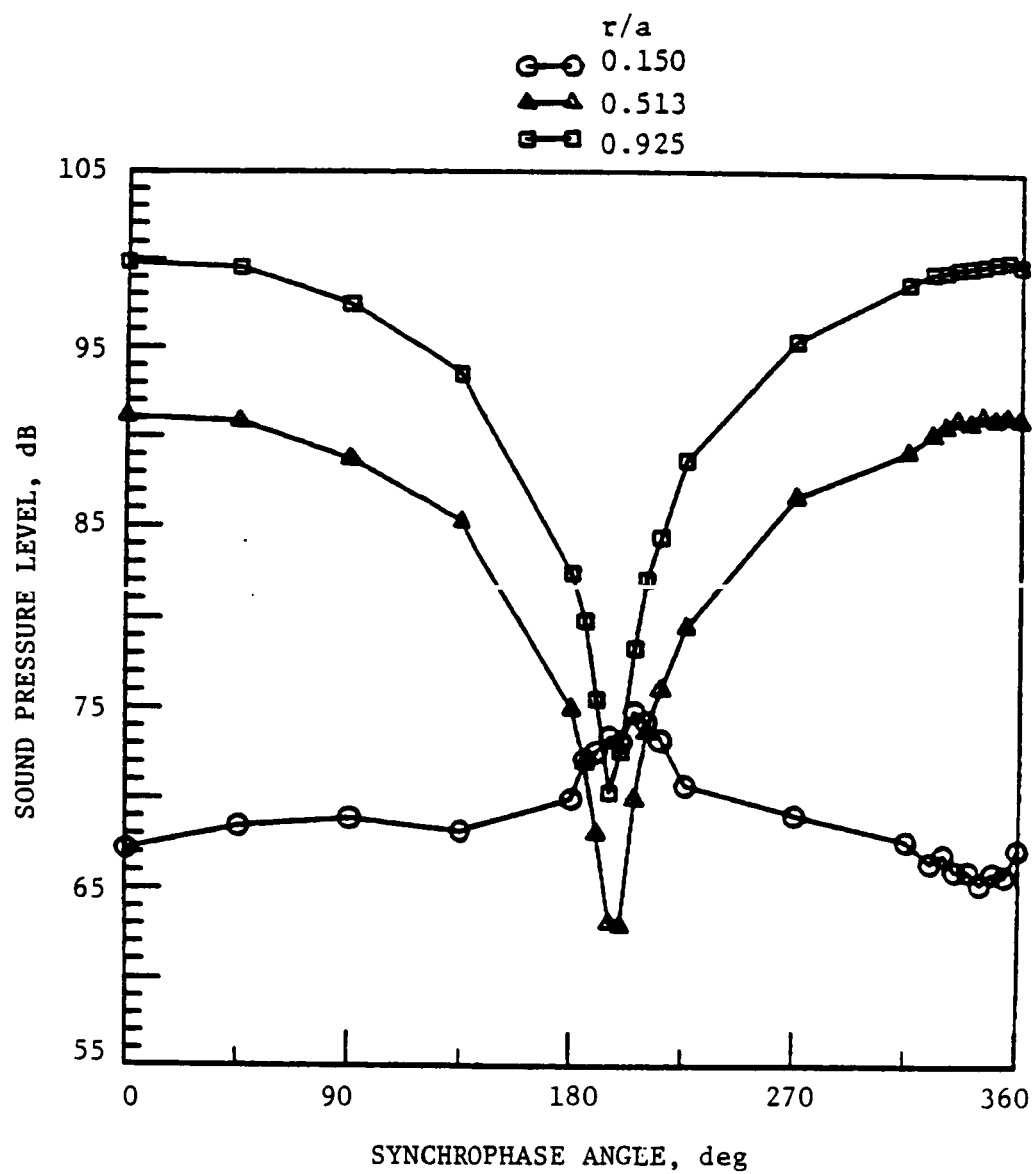


Fig. 44. Interior Pressure Measurements at $x/a = 0.0$, $\theta = 90^\circ$, and $f = 708$ Hz with Internal Acoustic Damping.

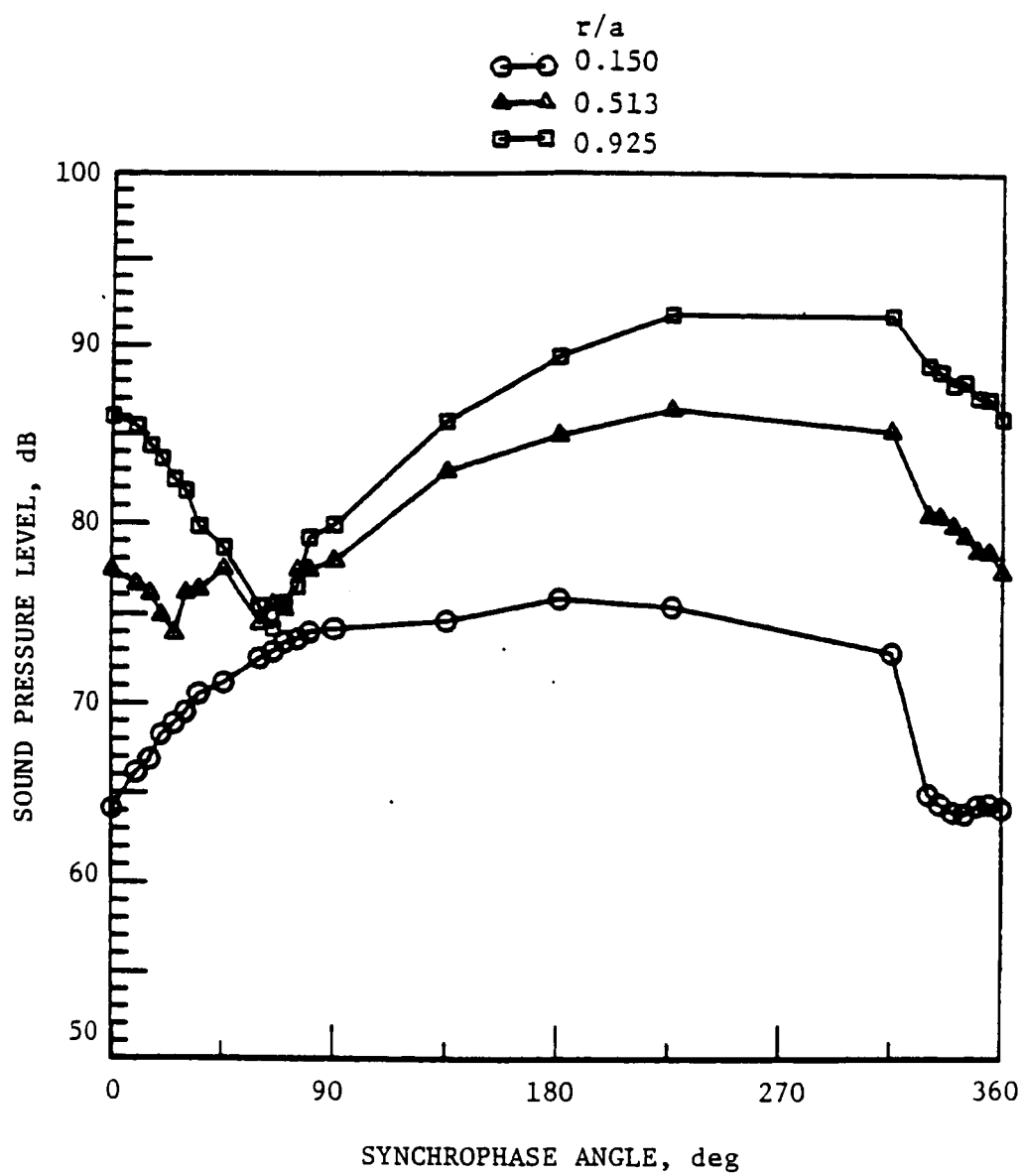


Fig. 45. Interior Pressure Measurements at $x/a = 0.0$, $\theta = 135^\circ$, and $f = 708$ Hz with Internal Acoustic Damping.

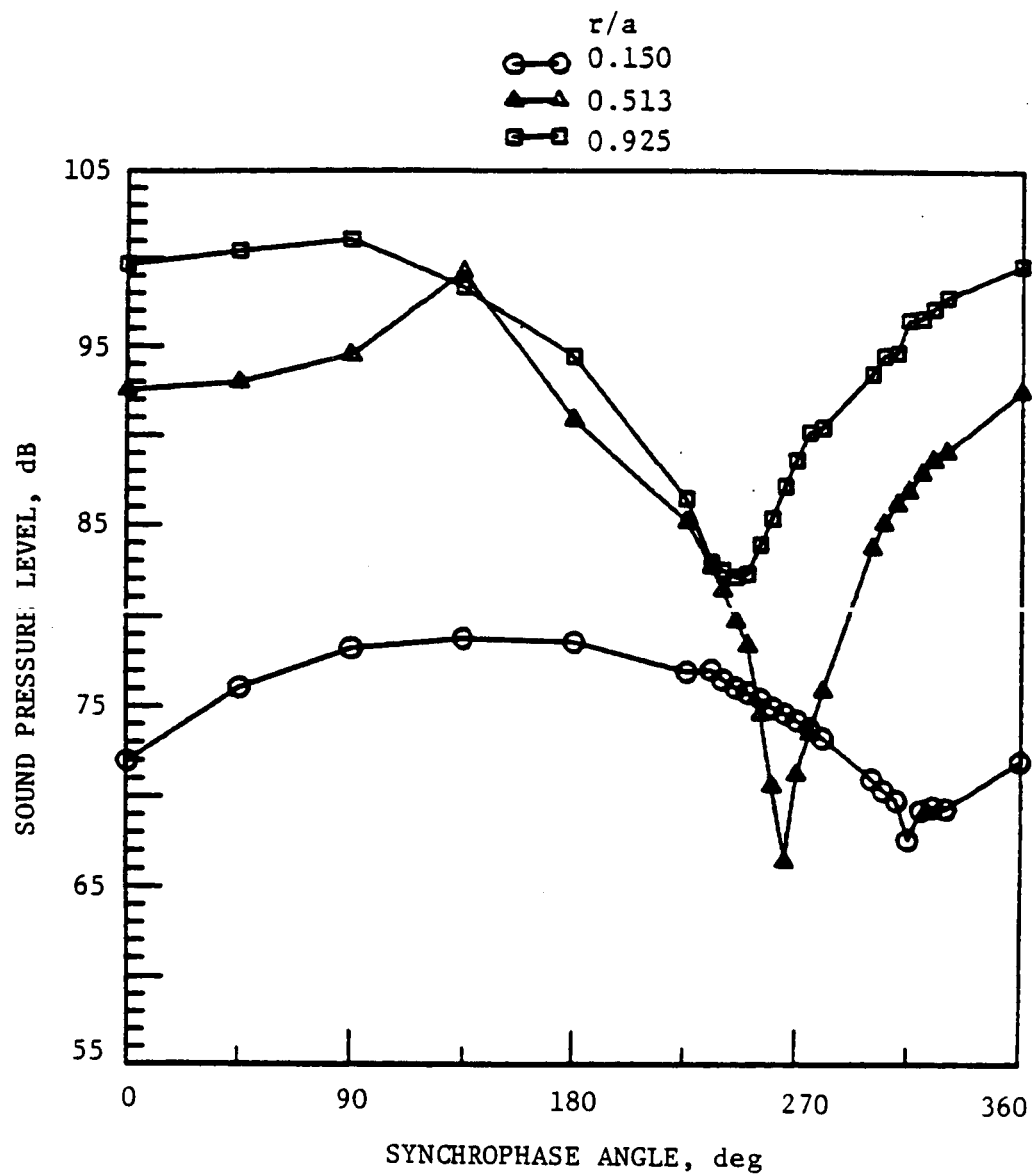


Fig. 46. Interior Pressure Measurements at $x/a = 0.0$, $\theta = 180^\circ$, and $f = 708$ Hz with Internal Acoustic Damping.

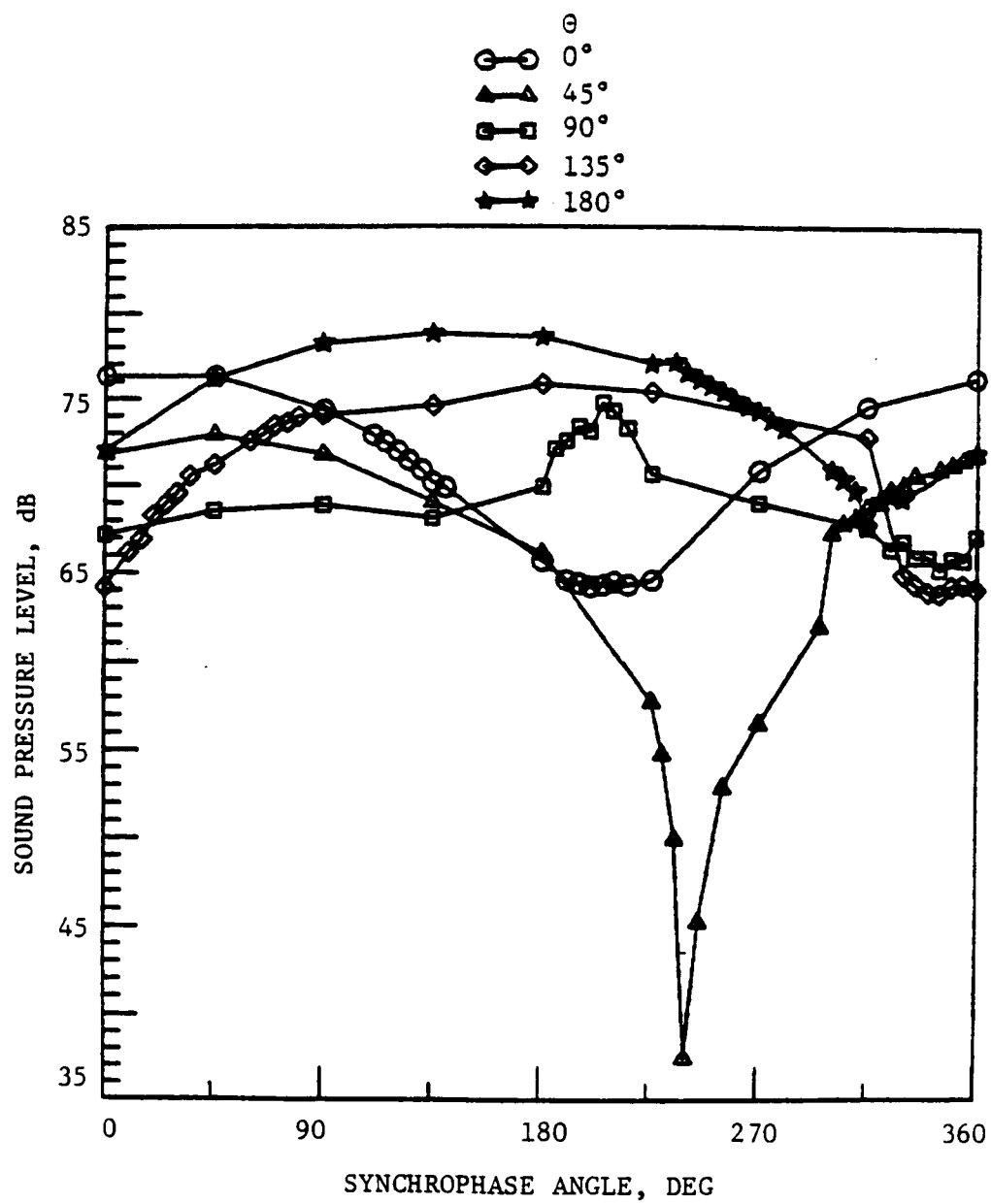


Fig. 47. Interior Pressure Measurements at $x/a = 0.0$, $r/a = 0.150$, and $f = 708$ Hz with Internal Acoustic Damping.

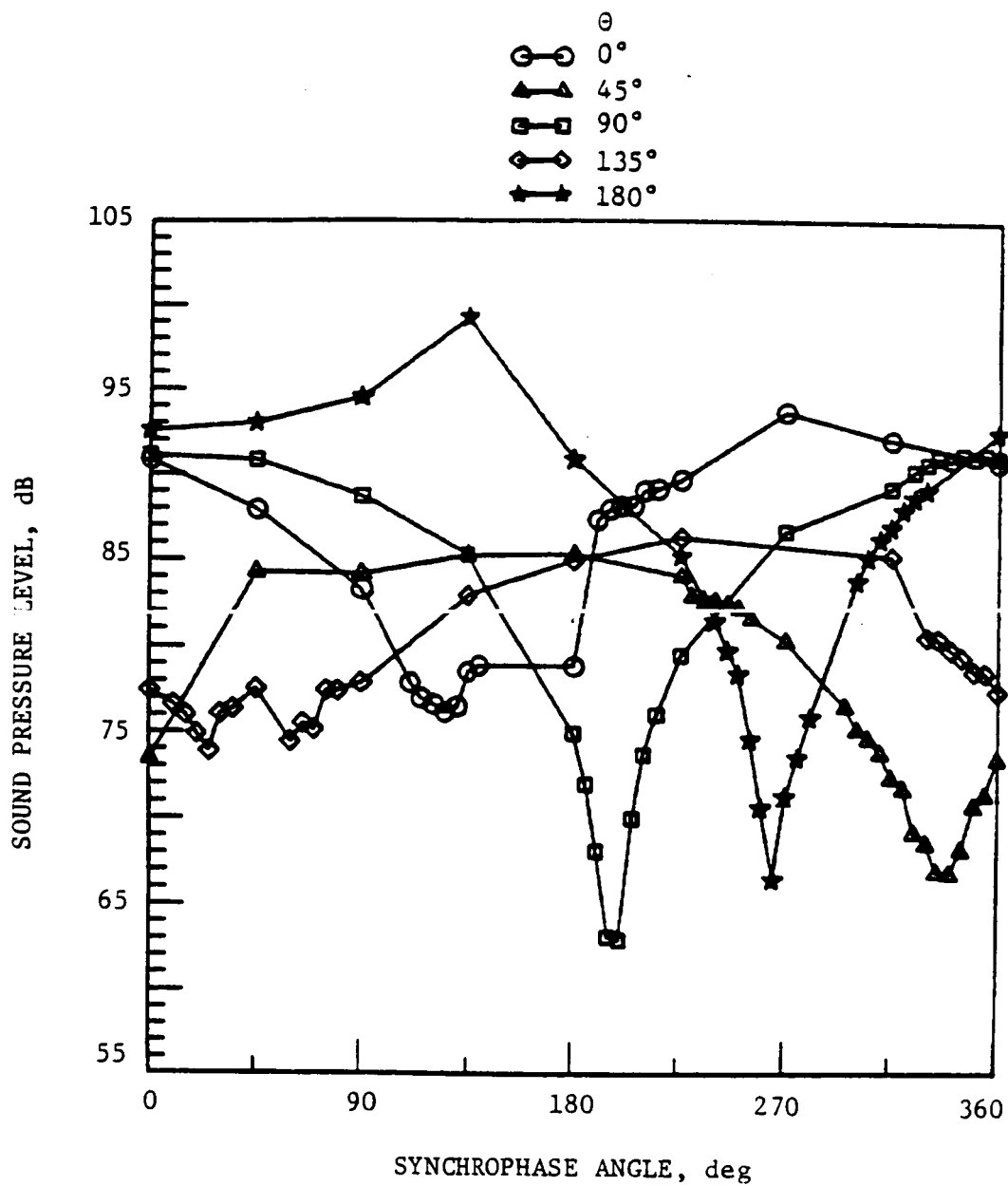


Fig. 48. Interior Pressure Measurements at $x/a = 0.0$, $r/a = 0.513$, and $f = 708$ Hz with Internal Acoustic Damping.

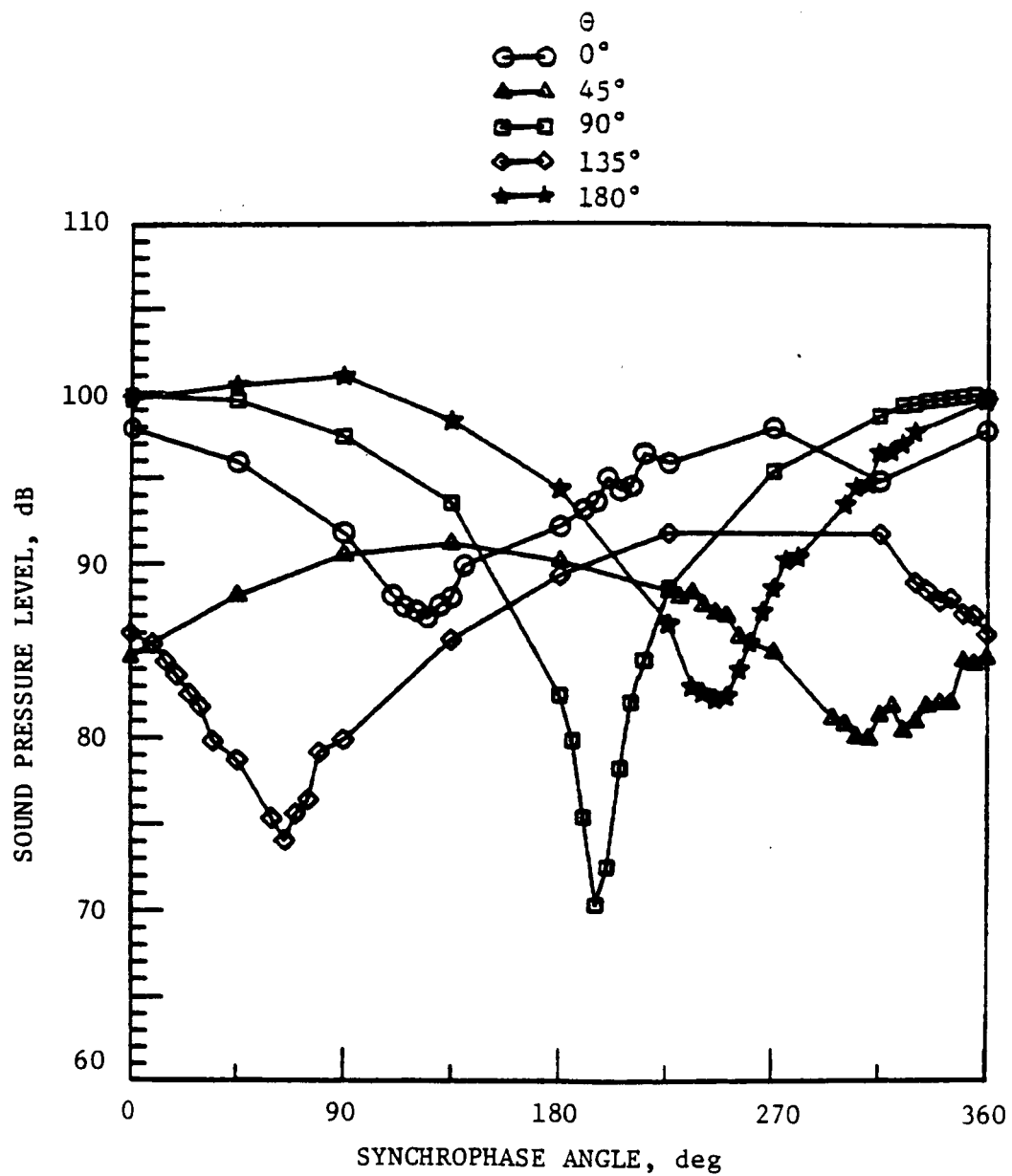


Fig. 49. Interior Pressure Measurements at $x/a = 0.0$, $r/a = 0.925$, and $f = 708$ Hz with Internal Acoustic Damping.

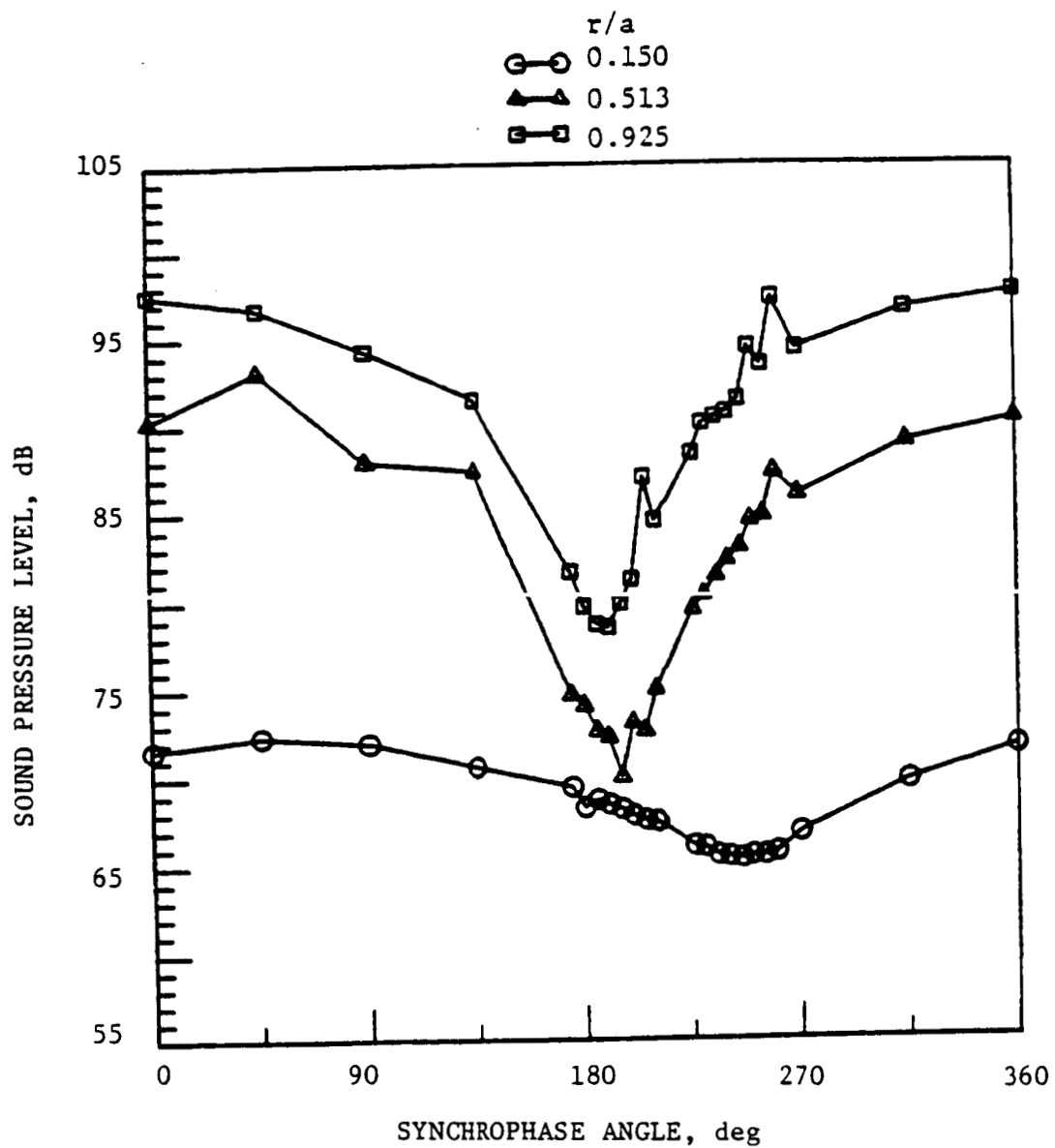


Fig. 50. Interior Pressure Measurements at x/a 0.4, $\theta = 0^\circ$, and $f = 708$ Hz with Internal Acoustic Damping.

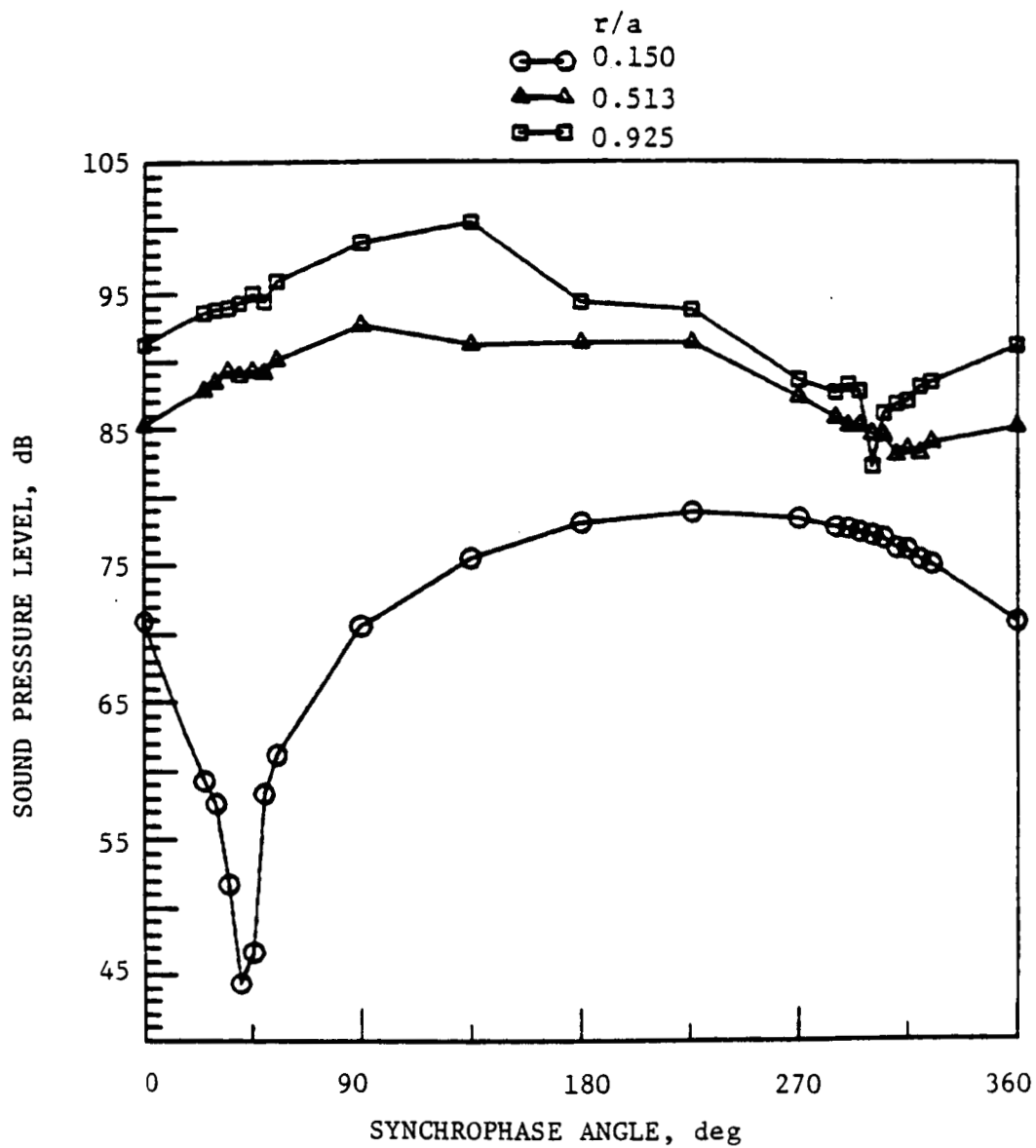


Fig. 51. Interior Pressure Measurements at $x/a = 0.8$, $\theta = 0^\circ$, and $f = 708$ Hz with Internal Acoustic Damping.

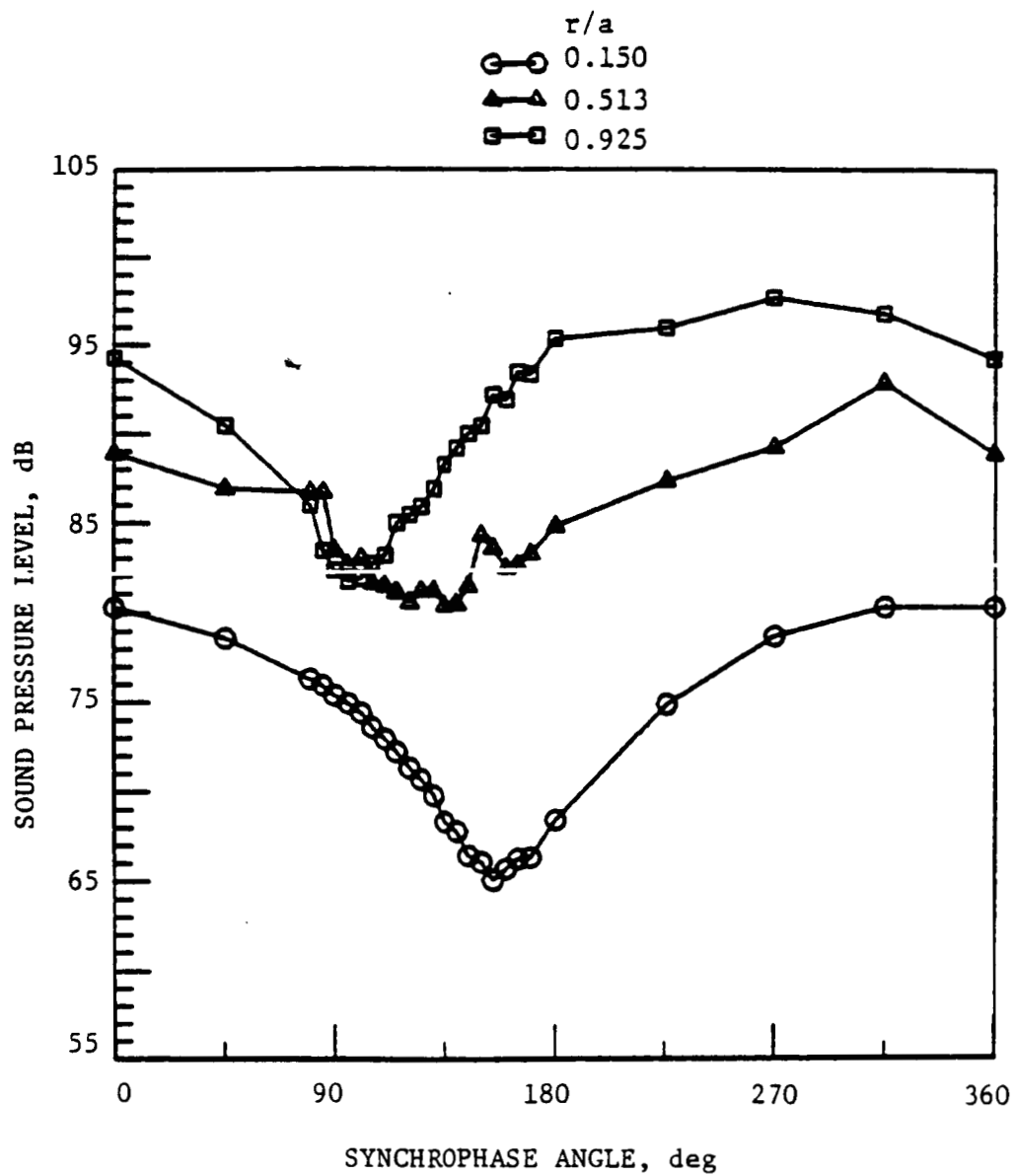


Fig. 52. Interior Pressure Measurements at $x/a = 1.6$, $\theta = 0^\circ$, and $f = 708$ Hz with Internal Acoustic Damping.

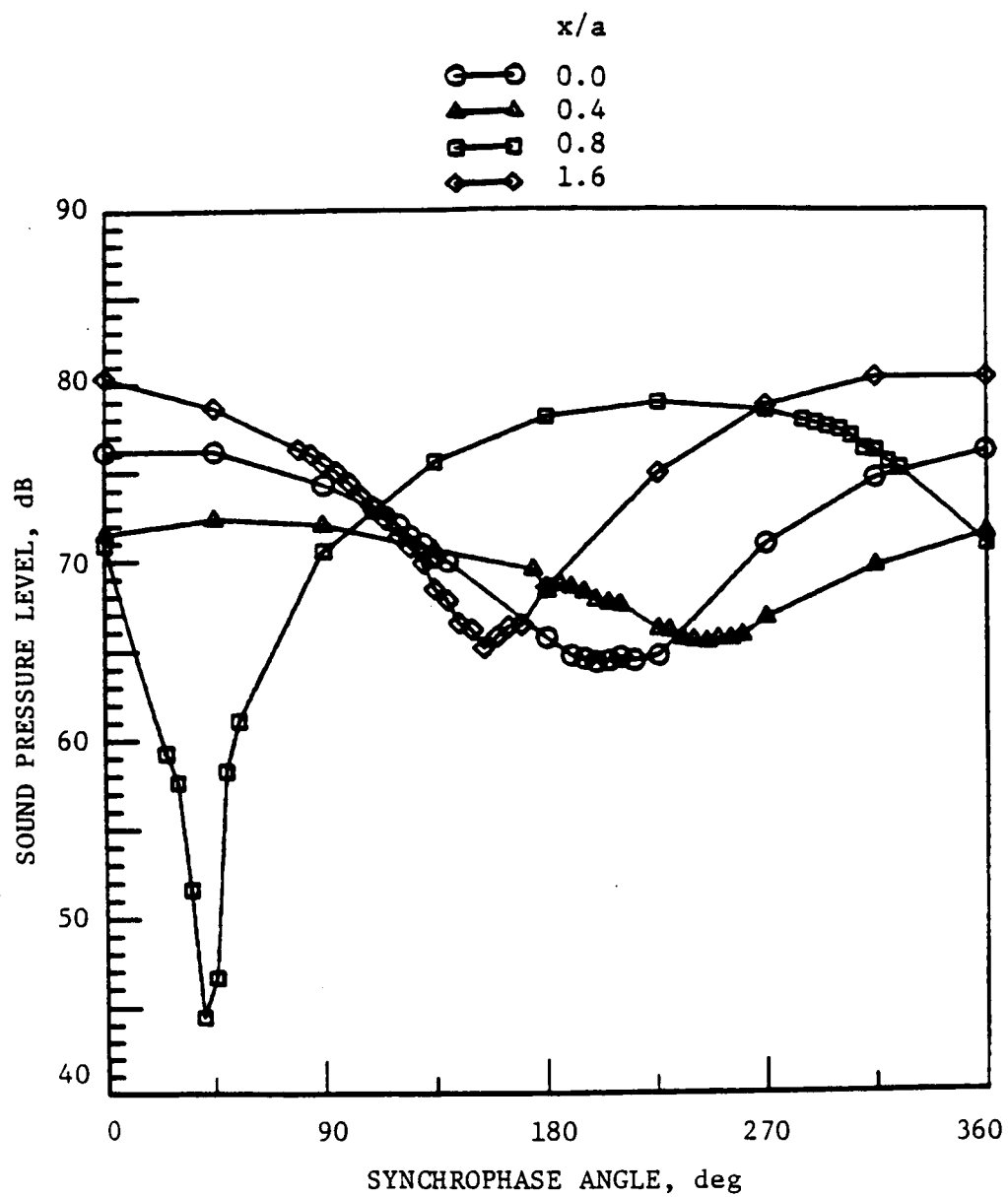


Fig. 53. Interior Pressure Measurements at $r/a = 0.150$, $\theta = 0.0^\circ$, and $f = 708$ Hz with Internal Acoustic Damping.

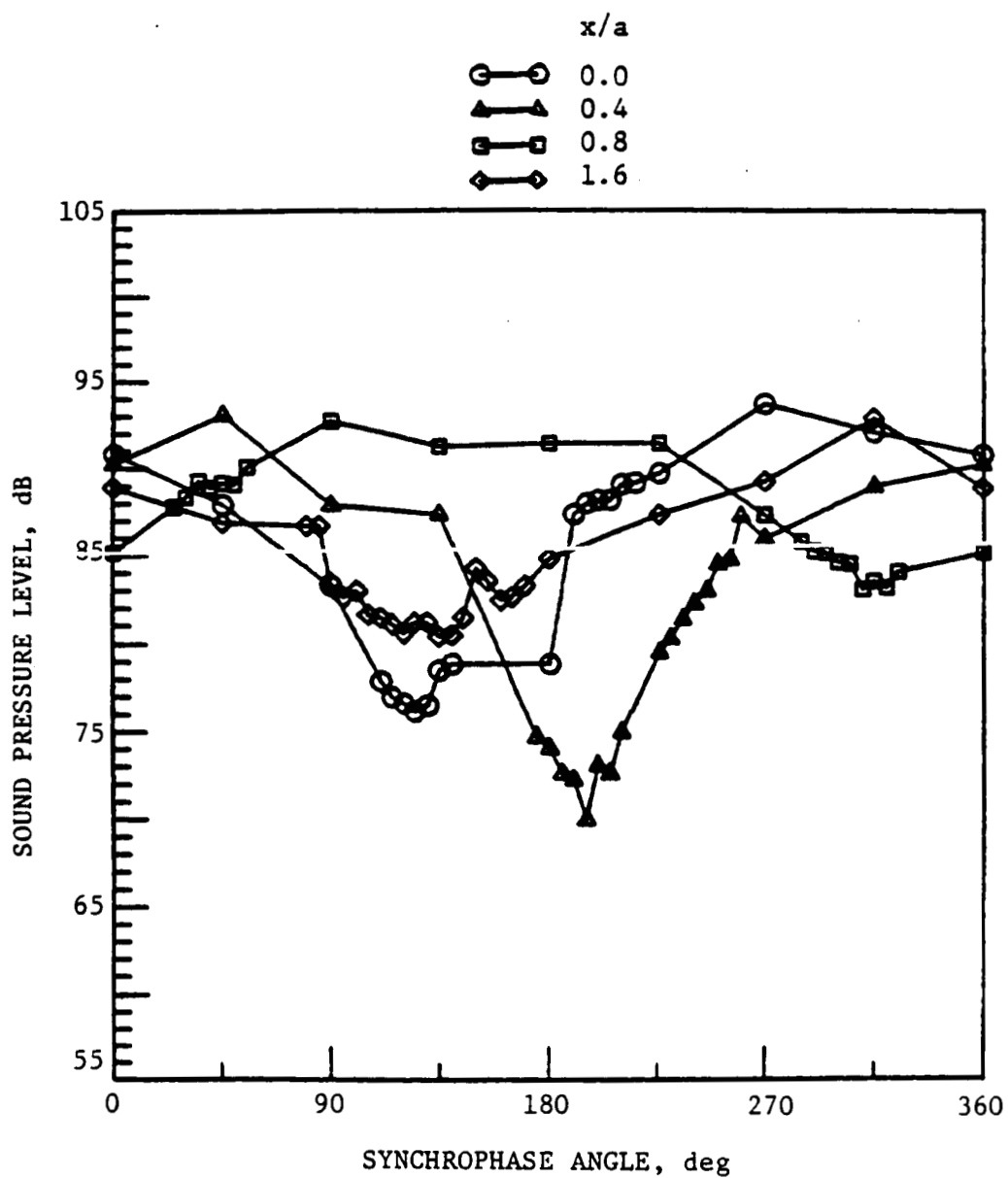


Fig. 54. Interior Pressure Measurements at $r/a = 0.513$, $\theta = 0^\circ$, and $f = 708$ Hz with Internal Acoustic Damping.

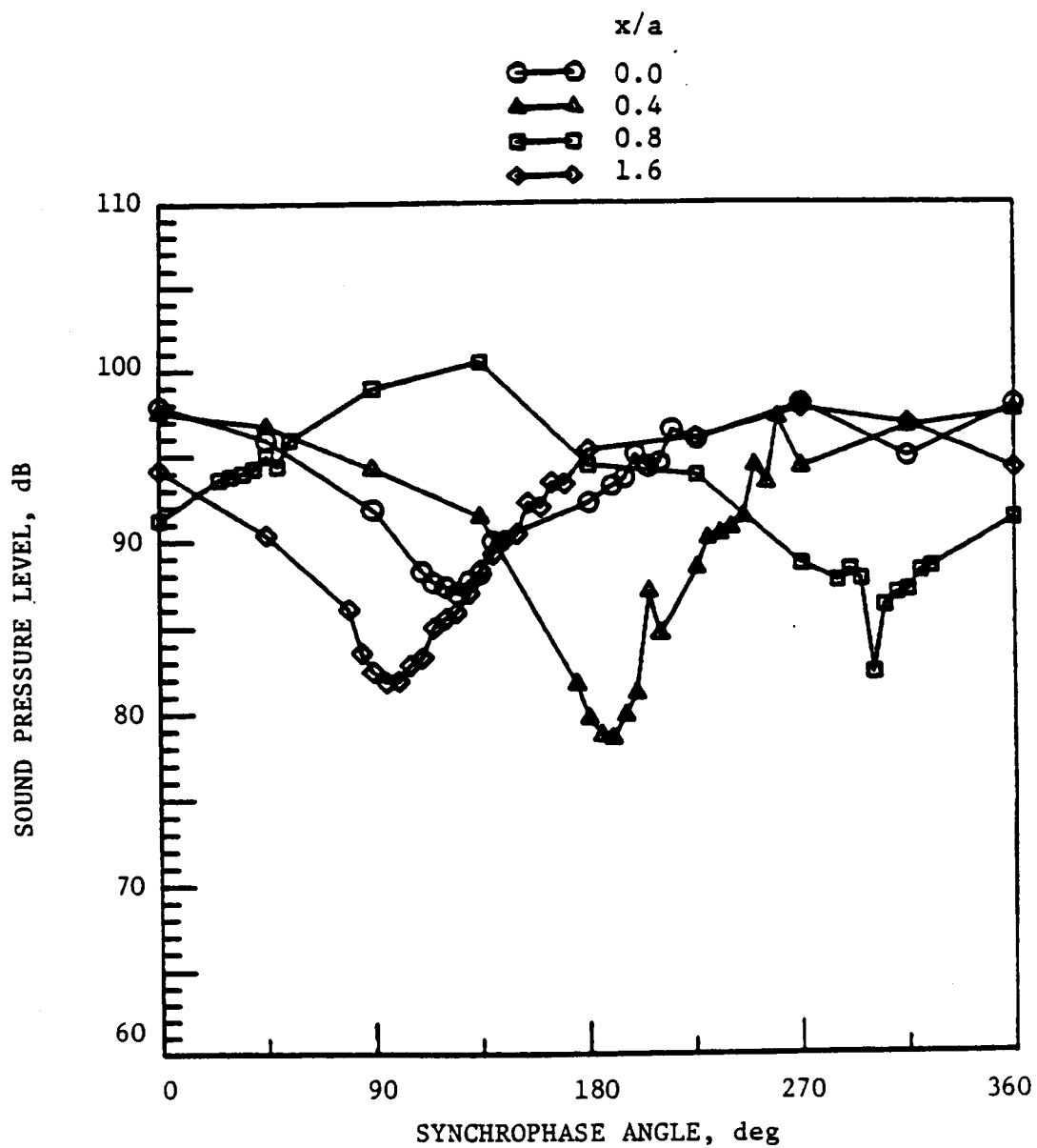


Fig. 55. Interior Pressure Measurements at $r/a = 0.925$, $\theta = 0^\circ$, and $f = 708$ Hz with Internal Acoustic Damping.

1. Report No. NASA CR-178185		2. Government Accession No.		3. Recipient's Catalog No.	
4. Title and Subtitle An Experimental Investigation of the Interior Noise Control Effects of Propeller Synchrophasing				5. Report Date October 1986	
				6. Performing Organization Code 535-03-11-03	
7. Author(s) J. D. Jones C. R. Fuller				8. Performing Organization Report No.	
				10. Work Unit No.	
9. Performing Organization Name and Address Virginia Polytechnic Institute and State University Department of Mechanical Engineering Blacksburg, VA 24061				11. Contract or Grant No. NAG1-390	
				13. Type of Report and Period Covered Contractor Report	
12. Sponsoring Agency Name and Address National Aeronautics and Space Administration Washington, DC 20546				14. Sponsoring Agency Code	
15. Supplementary Notes This report has been prepared jointly by J. D. Jones and C. R. Fuller of Virginia Polytechnic Institute and State University under grant NAG1-390. <u>Langley Technical Monitor: Harold C. Lester</u>					
16. Abstract A simplified cylindrical model of an aircraft fuselage is used to investigate the mechanisms of interior noise suppression using synchrophasing techniques. This investigation allows isolation of important parameters to define the characteristics of synchrophasing. The optimum synchrophase angle for maximum noise reduction is found for several interior microphone positions with pure tone source excitation. Noise reductions of up to 30 dB are shown for some microphone positions, however, overall reductions are less. A computer algorithm is developed to decompose the cylinder vibration into modal components over a wide range of synchrophase angles. The circumferential modal response of the shell vibration is shown to govern the transmission of sound into the cylinder rather than localized transmission. As well as investigating synchrophasing, the interior sound field due to sources typical of propellers has been measured and discussed.					
17. Key Words (Suggested by Author(s)) Interior Noise Synchrophasing Cylinder Response Modal Decomposition			18. Distribution Statement Unclassified - Unlimited Subject Category - 71		
19. Security Classif. (of this report) Unclassified		20. Security Classif. (of this page) Unclassified		21. No. of Pages 102	
				22. Price A06	